

# Radial velocity homogeneous analysis of M dwarfs observed with HARPS

## I. Exoplanet detection and candidates<sup>★</sup>

L. Mignon<sup>1,2</sup>, X. Delfosse<sup>1</sup>, X. Bonfils<sup>1</sup>, N. Meunier<sup>1</sup>, N. Astudillo-Defru<sup>3</sup>, G. Gaisne<sup>1</sup>, T. Forveille<sup>1</sup>, F. Bouchy<sup>2</sup>, G. Lo Curto<sup>4</sup>, S. Udry<sup>3</sup>, D. Segransan<sup>2</sup>, N. Unger<sup>2</sup>, C. Lovis<sup>2</sup>, N. C. Santos<sup>5,6</sup>, and M. Mayor<sup>2</sup>

<sup>1</sup> Univ. Grenoble Alpes, CNRS, IPAG, F-38000 Grenoble, France  
correspondence: Lucile.Mignon@unige.ch

<sup>2</sup> Observatoire astronomique de l'Université de Genève, 51 chemin Pegasi, 1290 Versoix, Switzerland

<sup>3</sup> Departamento de Matemática y Física Aplicadas, Universidad Católica de la Santísima Concepción, Alonso de Rivera 2850, Concepción, Chile

<sup>4</sup> European Southern Observatory, Casilla 19001, Santiago 19, Chile

<sup>5</sup> Instituto de Astrofísica e Ciências do Espaço, Universidade do Porto, CAUP, Rua das Estrelas, 4150-762 Porto, Portugal

<sup>6</sup> Departamento de Física e Astronomia, Faculdade de Ciências, Universidade do Porto, Rua Campo Alegre, 4169-007 Porto, Portugal

Received ; accepted

### ABSTRACT

**Context.** The census of planets around M dwarfs in the solar neighbourhood meets two challenges: detecting the best targets for the future characterisation of planets with ELTs, and studying the statistics of planet occurrence that are crucial to formation scenarios. The radial velocity (RV) method remains the most appropriate for such a census as it is sensitive to the widest ranges of masses and periods. HARPS, mounted on the 3.6 m telescope at La Silla Observatory (ESO, Chile), has been obtaining velocity measurements since 2003, and can therefore be used to analyse a very large and homogeneous dataset.

**Aims.** We performed a homogeneous analysis of the RV time series of 200 M dwarfs observed with HARPS from 2003 to 2019 (gathering more than 15000 spectra), with the aim of understanding detectable signals such as stellar and planetary companions and activity signals.

**Methods.** The RVs were computed with a template matching method before carrying out the time series analysis. First, we focused on the systematic analysis of the presence of a dominant long-term pattern in the RV time series (linear or quadratic trend and sine function). Then, we analysed higher-frequency periodic signals using periodograms of the residual time series and Keplerian function fitting.

**Results.** We found long-term variability in 57 RV time series (28.5%). This led to the revision of the parameters of the massive planet (GJ 9482 b), as well as the detection of four substellar and stellar companions (around GJ 3307, GJ 4001, GJ 4254, and GJ 9588), for which we characterised inclinations and masses by combining RV and astrometry. The periodic analysis allowed us to recover 97% of the planetary systems already published in this sample, but also to propose three new planetary candidates orbiting GJ 300 (7.3M<sub>⊕</sub>), GJ 654 (5M<sub>⊕</sub>), and GJ 739 (39M<sub>⊕</sub>), which require additional measurements before they can be confirmed.

**Key words.** Methods: data analysis – exoplanets – Stars: M-dwarfs – Techniques: radial velocities – Stars: Activity – Stars: Planetary Systems

## 1. Introduction

M dwarfs represent 80% of the stellar neighbourhood (e.g. Henry et al. 1994). Due to their favourable star–planet contrast and separation, planetary systems orbiting the closest M dwarfs are the most promising targets for future atmospheric characterisation by the new generation of facilities. They provide the only opportunity in the coming decade to obtain reflected spectra of Earth-like or Neptune-type planets by combining high-contrast imaging and high-dispersion spectroscopy on extremely large telescopes (ELTs) (Snellen et al. 2015; Marconi et al. 2020). Although many planets have been identified in the very close solar neighbourhood (e.g. Bonfils et al. 2011, 2018b; Delfosse et al. 2013; Anglada-Escudé et al. 2016; Astudillo-Defru et al. 2017b;

Díaz et al. 2019), the census of planets around these stars is far from complete.

Such a census is also necessary for statistical studies of planets orbiting around very low-mass stars and their unbiased mass–period distribution (Bonfils et al. 2013b; Sabotta et al. 2021; Pinamonti et al. 2022). Increasing the size of the probed sample provides more precise occurrence rates, and thus provides even stronger constraints on the formation scenarios, and in particular on the dependence on the central mass (e.g. Burn et al. 2021).

The radial velocity (RV) method remains the most complete way to identify planetary systems in the solar neighbourhood as it is not limited to particular configurations, unlike the transit method. It is particularly well suited to the search for systems around very low-mass stars, especially for planets located in their habitable zone (HZ). The orbital distances of the HZs strongly depend on the luminosity (hence the mass) of the host stars: fainter stars have closer HZs. Exo-Earths in the HZs of M

<sup>★</sup> All radial velocity time series and the full Table B.5 are only available at the CDS via anonymous ftp to cdsarc.u-strasbg.fr (130.79.128.5) or via <http://cdsarc.u-strasbg.fr/viz-bin/cat/J/A+A/XXX/AX>

dwarfs thus exhibit much larger RV oscillations on much shorter timescales than those orbiting Sun-like stars.

Since 2003 the HARPS spectrograph (Mayor et al. 2003), installed on the 3.6-meter telescope at La Silla Observatory (ESO, Chile), has been producing precise RV measurements for thousands of stars, including many M dwarfs in the solar neighbourhood. Our study is a systematic and homogeneous analysis of the RV time series of 200 M dwarfs observed on at least ten nights with HARPS (gathering more than 15000 velocities). After computing the RVs using a template matching method, we applied an analysis based on the method of (Cumming et al. 1999), (Cumming et al. 2008), (Zechmeister et al. 2009), (Zechmeister & Kürster 2009), and (Bonfils et al. 2013b). To summarise, we first searched for a long-term signal (modelled by different functions) in the time series, then for higher-frequency periodic signals; finally, we analysed the signals found to determine whether they are due to stellar activity or a planetary candidate.

The outline of this paper is as follows. In Sect. 2 we present the sample of M dwarfs observed by HARPS. In Sect. 3 we describe the observations, our procedure to extract accurate RVs, and the automatic corrections made to build the final sample. In Sect. 4 we present the long-term models that tested the different statistical validations used. In Sect. 5 we present the frequency analysis of the sample, the tools used, and the identification of the Keplerian signals found and subtracted. In Sect. 6 we present a first analysis of the stellar and planetary candidates detected. Finally, we conclude in Sect. 7, and discuss the limitations of this study in Sect. 8.

## 2. Sample

Since our study is based on a dataset entirely derived from HARPS (Mayor et al. 2003), it is subject to similar systematic effects, and homogeneous analysis can be performed using a consistent approach. The first RV follow-up programme for M dwarfs was conducted as soon as HARPS came into operation, allocating 10% of the 500 nights of the Guaranteed Times to characterising the planetary population orbiting stars with masses below  $0.6 M_{\odot}$  (Mayor et al. 2003; Bonfils et al. 2013b). Since then, HARPS has played a major role in the search for planets around M dwarfs, contributing to the detection of a large fraction of the M-dwarf planets thanks to numerous programmes dedicated entirely or in part to M dwarfs. This possibly includes the first super-Earths in HZ (Bonfils et al. 2013a; Delfosse et al. 2013; Anglada-Escudé et al. 2013; Astudillo-Defru et al. 2017c; Bonfils et al. 2018b), and the closest planet to us (Anglada-Escudé et al. 2016). HARPS RVs were also used to confirm the planetary nature and to measure the masses of transiting planet candidates around M dwarfs originally identified by transit surveys such as K2, MEarth, and now TESS (e.g. Charbonneau et al. 2009; Berta-Thompson et al. 2015; Almenara et al. 2015; Dittmann et al. 2017; Ment et al. 2019; Winters et al. 2019; Astudillo-Defru et al. 2020; Lillo-Box et al. 2020b,a; Van Eylen et al. 2021).

Our first objective in this study is to collect the spectra obtained by HARPS for all the programmes targeting M dwarfs. We restrict our sample to stars located within 26 pc.

### 2.1. Input catalogues

#### 2.1.1. Initial selection

Our reference catalogues of M dwarfs in the solar neighbourhood are from a compilation of Gaidos et al. (2014), Winters

et al. (2014), Stauffer et al. (2010, the release of the Gliese and Jahreiss catalogue), Henry et al. (2018), and Winters et al. (2021). We cross-referenced each object in the combined catalogue with the second release of the Gaia catalogue (Gaia DR2 Collaboration et al. 2018)<sup>1</sup> to extract very precise coordinates, parallaxes, proper motions, and G-band photometry. Finally, we retained 1362 stars, the southern ( $\delta < +20^{\circ}$ ) M dwarfs within 26 pc. We cut the catalogue slightly beyond the traditional (Gliese & Jahreiß 1991) 25 pc limit of the solar neighbourhood to provide a margin that includes some true members of the 25 pc volume with very slightly overestimated distances.

We cross-matched the positions of these 1362 stars with those of the public HARPS spectra observed before 2019<sup>2</sup> available in the ESO archives. Of these 1362 stars, 425 have at least one HARPS spectrum, for a total of 12984 spectra. Figure 1 superposes the distance distributions of the 1362 M dwarfs of our combined catalogue with the 425 observed with HARPS; all the programmes used are listed in Table B.1.

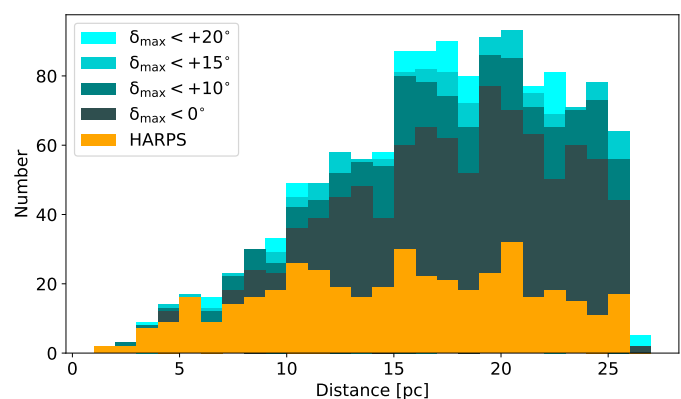


Fig. 1: Distance distribution of the sample. In green is the distribution of our reference catalogue for different declination limits. In orange is the distance distribution of the M dwarfs with HARPS measurements.

As detailed in the caption, the figure proposes several alternative declination cuts for the combined catalogue. Most of the southern M dwarfs within 10 pc were observed with HARPS, as this corresponds to the distance limit of the sample studied during the GTO programme (Bonfils et al. 2013b). Beyond this distance, only a minority of the catalogued M dwarfs were observed with HARPS, and overall 31.2% of the stars in our combined catalogue have HARPS spectra. Completeness rates are detailed in Table 1 as a function of distance and declination.

Pre-Gaia solar neighbourhood catalogues are known to be incomplete beyond 15 pc, and miss over half of the stars between 20 and 25 pc (see Gaia Collaboration et al. 2021b, and in particular their figure 10). A much more complete list of stars can now be obtained directly from the Gaia DR3 catalogue, as was done by e.g. Gillon et al. (2020) and Reylé et al. (2021). This, however, is not directly relevant to the scope of this paper since all observing programmes that obtained M dwarf spectra with HARPS before 2019 built upon pre-Gaia input catalogues. The

<sup>1</sup> Gaia DR3 (Gaia Collaboration et al. 2021a) was not yet available when we initiated the project. After verification, the Gaia parameters used for our study did not change significantly between Gaia DR2 and DR3.

<sup>2</sup> Corresponding to data for which the proprietary time had expired when we interrogated the ESO archive in 2021; we note that HARPS has acquired few measurements of M dwarfs since 2019.

Table 1: Fraction of stars observed with HARPS.

$\delta_{max}$	+0°	+10°	+15°	+20°
Distance				
5 pc	71,43%	73,08%	74,07%	72,41%
7 pc	80,0%	81,13%	80,70%	75,0 %
10 pc	63,64%	63,91%	64,28%	62,34 %
15 pc	45,03%	48,74%	49,73%	48,64%
26 pc	31,33%	34,39%	35,13%	31,25%

**Notes.** Fraction of observed stars from the combined catalogue as a function of the declination and the distance.

more complete Gaia catalogues can therefore only include solar neighbourhood M dwarfs that have not yet been observed by HARPS.

### 2.1.2. Complementary data

As explained above, coordinates, proper motions, and parallaxes are mainly from the Gaia catalogue (Gaia DR2 Collaboration et al. 2018) and completed by various sources for the 11 missing stars<sup>3</sup>

sV-band magnitudes are from Koen et al. (2010) for 57% of the sample, supplemented by Zacharias et al. (2013) for 15%. A further 15% come from a dozen other catalogues, leaving 13% of the targets without a V-band magnitude value. The G-band magnitudes come from the Gaia DR2 catalogue Collaboration et al. (2018) for 97.5% of the sample. The H-, J-, and K-band magnitudes come from the 2MASS database (Cutri et al. 2003), supplemented by H- and J-band magnitudes of GJ 205 from Ducati (2002), and the H-band magnitude of GJ 1 and K-band magnitude of GJ 803 from Koen et al. (2010).

For our study we also needed to determine the masses of the 425 M dwarfs in our sample. We computed them using Delfosse et al. (2000) empirical mass-luminosity relation with parallaxes and photometry collected. Since the magnitude V is not available for the entire sample and the mass–luminosity relations in the optical bands depend strongly on the metallicity, we used only the three near-infrared relationships (mass versus  $M_K$ ,  $M_H$ , and  $M_J$ ). The mass value for each star chosen and used for this study is the average of the three values. Table B.5 lists all the stellar parameters collected and computed for the 425 stars in the sample.

## 2.2. Magnitude and mass distributions

The G-band distribution in Fig. 2 has a mean (resp. median) value of 10.20 mag (resp. 10.38 mag), and ranges from 5.98 to 14.30 mag. Regarding the magnitude V, with a median value of 11.28 mag, our sample is almost 1 magnitude fainter than the 11 pc volume-limited sample studied by Bonfils et al. (2013b), which will naturally impact the median photon noise of our RV measurements.

The mass distribution in our sample (Fig. 3) ranges from 0.79 to 0.08  $M_\odot$  with an average (resp. median) value of 0.45  $M_\odot$  (resp. 0.46  $M_\odot$ ). The distribution peaks between 0.5 and

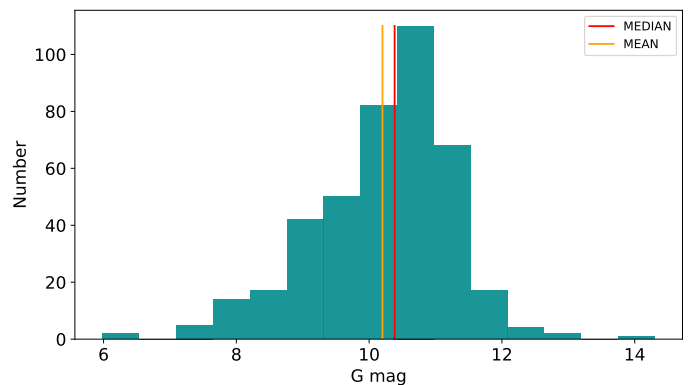


Fig. 2: G magnitude distribution of the sample.

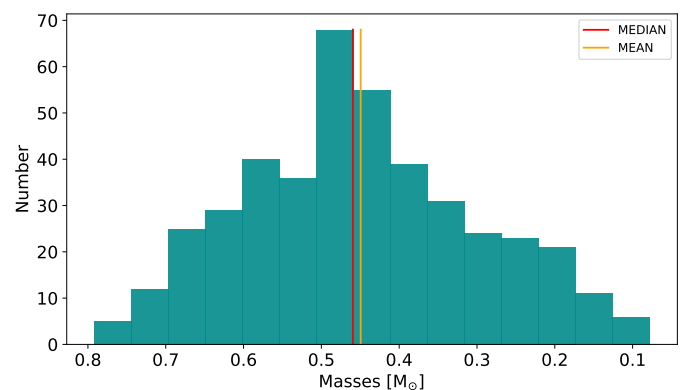


Fig. 3: Mass distribution of the sample.

0.45  $M_\odot$ , whereas the stellar mass function of the solar neighbourhood is known to increase monotonically (on a linear scale) up to the hydrogen burning limit (e.g. Figure 5 in Chabrier 2001). This simply illustrates a selection bias in our sample: the underlying observing programmes are magnitude-limited, and therefore under-represent the faint late M dwarfs.

### 2.3. The 7 pc subsample

Planets orbiting the nearest M dwarfs represent the only practical short-term opportunities for characterising Earth-like planets. In addition to transmission spectroscopy of transiting planets (e.g. with JWST Doyon et al. 2014; Beichman et al. 2014, with NIRPS Bouchy et al. 2017), a new strategy using ELTs is being developed for the more general case of non-transiting planets. Snellen et al. (2015) demonstrates that the combination of high-contrast imaging and high-dispersion spectroscopy with ELTs can be used to characterise the rocky planets around our nearest neighbours. This ambitious objective can only be achieved from the ground in the most favourable case: lowest planet-to-star contrast and widest angular separation. Adopting  $3\lambda/D$  in the J-band as the practical limit for resolving a planetary system by this method, and for a planet located at the outer limit of the HZ of a mid-M dwarf ( $\sim 0.3$  au of the central star; see e.g. Kopparapu et al. 2013), the distance limit for the method on an ELT is 7 pc.

Monitoring this sample of 61 M dwarfs at less than 7 pc (for  $\delta < +20^\circ$ ) is therefore a particularly important issue at the moment. Furthermore, it is better observed than the complete sample, with 46 out of the 61 targets already observed with HARPS

<sup>3</sup> Van Leeuwen (2007): GJ 257, GJ 2033, GJ 4206, GJ 9163, HD196982; Weinberger et al. (2016): GJ 406; Riedel et al. (2014): GJ 3332; Finch et al. (2018): GJ 3813, GJ 4038; Winters et al. (2016): L43-72; Riaz et al. (2006): LP 993-116

(75%). The 16 unobserved stellar systems illustrate the selection biases of RV monitoring by falling into three categories: very late-M dwarfs that are too faint ( $V > 15$ ), binary stars that cannot be resolved with HARPS (separation smaller than the diameter of the fibre entrance), and fast rotators already identified before the beginning of HARPS observations high RV jitter expected from magnetic activity. Table 2 lists the 16 closest southern systems without HARPS observations and provides the reason identified for each.

### 3. HARPS observations

#### 3.1. Radial velocity extraction

12984 HARPS spectra<sup>4</sup> of the 425 M dwarfs in our sample were retrieved from the ESO archive. Each spectrum covers the 380–690 nm spectral range, spread over 71 orders with a median resolving power of 115,000 and is wavelength calibrated with very high accuracy. The data were analysed by the HARPS pipeline (Lovis & Pepe 2007), determining the RV by cross-correlation with a binary mask (Pepe et al. 2002) giving a typical precision of around 1 m/s. The cross-correlation function (CCF) obtained by the pipeline can be considered an average spectral line.

To fully exploit the Doppler information of the spectra, we used a template-matching code that extracts the RV through a maximum likelihood analysis between a template and each individual spectrum (see Astudillo-Defru et al. 2017b, for more details). A template is built for each star by computing the median of all its spectra; according to Astudillo-Defru et al. (2015), at least ten spectra are needed for this operation. We therefore focused on the 218 M dwarfs observed at least ten times with HARPS. RV uncertainties (hereafter *svrad*) were computed as described in Bouchy et al. (2001), and mostly depend on the read-out noise and photon noise. To account for the long-term instabilities of HARPS, we quadratically added 0.8 m/s to this value to obtain the total *svrad* (Lovis et al. 2008; Coffinet et al. 2019).

#### 3.2. Fibres change on HARPS

HARPS was upgraded on 28 May 2015, when the vacuum vessel was opened to change the fibres and improve the RV stability (Lo Curto et al. 2015). It introduced an RV offset that depends on the spectral type of the observed target, and varies from several hundred m/s for F dwarfs to just a few m/s for M dwarfs. This upgrade modifies the shape of the spectral lines, and hence the full width at half maximum (FWHM) of the CCF. Figure 4 highlights this temporal evolution of FWHM values for the most observed M dwarfs (before and after the change) in five different subspectral types: GJ 701 (M0), GJ 229 (M1), GJ 2066 (M2), GJ 752 (M3), and LP 816-60 (M4).

The width of the CCF of the M dwarfs changes by a few tens of m/s (1.003% relative), slightly above its dispersion before or after the upgrade. Among the 218 stars with at least ten HARPS spectra, 71 were observed before and after the fibre change. Since the shape of the lines changed, we conservatively analysed the spectra before and after the upgrade separately for each star affected by the fibre change.

For the 37 stars with at least ten measurements both before and after the fibre change, we extracted the RV using two independent templates. The RV series for these stars corresponds to

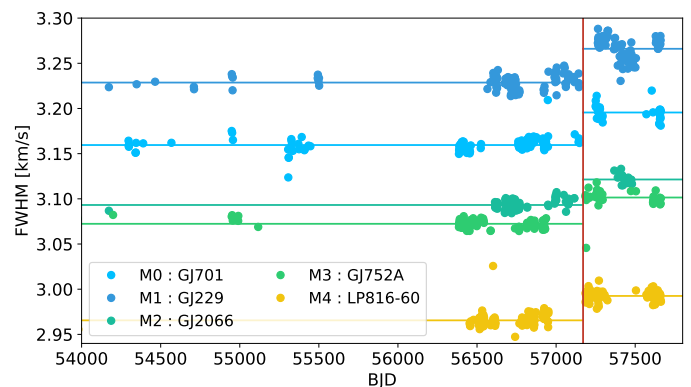


Fig. 4: Evolution of the CCF-FWHM for five different spectral subtypes. The red vertical line gives the date (BJD: Barycentric Julian Day) of the fibre change. The horizontal solid lines show the median of the FWHM of the CCF with the M2 mask before and after the fibre change.

two successive series HARPS03 and HARPS15, and the RV offset between them is modelled together with other possible variations (Keplerian, activity effects). A total of 32 stars have at least ten measurements either before or after the upgrade (but not both), and for these we chose to analyse the longest series and ignore the shortest. Finally, GJ 79 and GJ 3192 were observed less than ten times both before and after the upgrade, and consequently were rejected from this study, leaving a remaining sample of 216 stars.

#### 3.3. Selection process

Before carrying out our systematic analysis, we discarded some lower-quality spectra to guarantee the robustness of the RV time series.

##### 3.3.1. Selection based on the signal-to-noise ratio

Firstly, we rejected all exposures that did not reach an RV precision of 5 m/s (corresponding to a signal-to-noise ratio,  $S/N < 10$  in spectral order 50 = 550 nm), a typical limit for detecting low-mass planets. Secondly, we quantified the chromospheric activity by measuring the ionised calcium doublet lines (Ca H&K at 393,3 nm and 396,3 nm) to identify whether any velocity variation is due to stellar activity. We therefore imposed a  $S/N$  greater than 1 in the order continuum corresponding to this spectral region of these wavelengths (order 7). After this selection, two stars ended up with fewer than ten spectra and were therefore excluded from the sample.

We also automatically excluded spectra penalised by poor weather conditions by imposing a relative criterion on the  $S/N$  (in the spectral order 50) of each star. We computed the dispersion of the  $S/N$  value ( $\sigma_{S/N_{50}}$ ) of all observations on a target, and rejected all spectra whose  $S/N$  was more than  $5\sigma$  below the median value. Once the outliers were rejected, we carried out a new iteration after calculating a new dispersion and median.

##### 3.3.2. Selection based on the FWHM

As shown in Fig. 4, for a given star and instrumental set-up (before or after the fibre change), the FWHM of the CCF varies slightly, with a typical dispersion  $\sigma_{FWHM}$  of a few m/s (0.3% rel-

<sup>4</sup> E2DS from [http://archive.eso.org/wdb/wdb/adp/phase3\\_spectral/form](http://archive.eso.org/wdb/wdb/adp/phase3_spectral/form)

Table 2: Nearest stars not observed by HARPS programmes (distance &lt; 7 pc)

Star	Distance (pc)	Spectral Type	Explanation	V flux	Vsini	Separation
GJ 1005	4.99 <sup>1</sup>	M4V	Close Binary	11.483 <sup>4</sup>	4.30 <sup>11</sup>	-
GJ 65 A/B	2.7195 - 2.6749	M5.5V - M6V	Fast Rotator & Binary	12.08 <sup>4</sup>	29.5 <sup>12</sup> - 37.9 <sup>12</sup>	2.31
GAT1370	3.8315	M7	faint late-M dwarf	15.13	-	-
LP944-20	6.4268	M9	faint late-M dwarf	18.69 <sup>6</sup>	-	-
GJ 1116 A/B	5.1508	M7V - M7V	Faint close binary	13.93 <sup>7</sup>	-	2.48
GJ 3522	4.39 <sup>3</sup>	M4	Close Binary	10.98 <sup>5</sup>	-	-
GJ 1128	6.5036	M4	<i>no explanation</i>	12.44	-	-
GJ 3622	4.5593	M6.5	faint late-M dwarf	15.784 <sup>5</sup>	3.3 <sup>12</sup>	-
2MUCD 20385	4.0450	M9V	faint late-M dwarf	17.532 <sup>8</sup>	-	-
GJ 1156	6.4641	M4.5V	Fast Rotator	13.90 <sup>5</sup>	15.6 <sup>12</sup>	-
GJ 473 A/B	4.3267 - 4.4747	M5.5V -	Close Binary	12.467 <sup>9</sup>	-	-
UCAC4 195-119117	5.3268	M6.5	faint late-M dwarf	-	-	-
SCRJ1845-6357	4.0053	M8.5	faint late-M dwarf	17.40 <sup>10</sup>	-	-
GJ 829 A	6.7798 - 3.4 <sup>2</sup>	M4	SB2 Binary	10.303 <sup>4</sup>	-	-
GJ 866 B		M5	SB2 Binary	12.38 <sup>5</sup>	-	-
GJ 896 A/B	6.2631 - 6.2535	M3.5 - M4	Fast Rotator	10.173 <sup>4</sup>	14.5 <sup>12</sup>	4.34

**Notes.** Distances are from Gaia Collaboration (2020) except marked: <sup>1</sup> Koen et al. (2010), <sup>2</sup> Torres et al. (2010), and <sup>3</sup> Riedel et al. (2014). Spectral types are from Gaidos et al. (2014), V flux : <sup>4</sup> Koen et al. (2010), <sup>5</sup> Zacharias et al. (2013), <sup>6</sup> Lurie et al. (2014), <sup>7</sup> Lépine & Shara (2005), <sup>8</sup> Costa et al. (2005), <sup>9</sup> Landolt (1992), and <sup>10</sup> Winters et al. (2010). Vsini values are from: <sup>11</sup> Hojjatpanah et al. (2019) and <sup>12</sup> Fouqué et al. (2018). Separations were obtained via ExoFOP tools: <https://exofop.ipac.caltech.edu/tess/>.

ative). Thus, a large variation in the FWHM indicates a problem in the RV measurement, an incorrect star identification, for example. For each star we rejected spectra whose FWHM value was more than  $3\sigma_{\text{FWHM}}$  from the median value.

### 3.4. Average data per night

The targets of this study were monitored via various observation programmes (listed in Table B.1). Time sampling can therefore vary considerably from one star to another. In order to standardise the datasets, we binned the RVs per night, using an average weighted by the uncertainties. After this final step, we rejected the 14 stars that had not been observed on at least ten different nights.

### 3.5. Final sample

After these different selection steps, our final sample contained 200 stars, representing 10513 spectra. Figure 5 shows the distribution of the number of nights per star. Some targets were no longer observed after only a few measurements, which explains the steep shape of the distribution. At this stage of the study, RV time series were binned per night and considered corrected from outliers.

## 4. Long-term analysis

The first step of the analysis is a study of the long-term trends in the 200 time series. To automatically identify the long-term pattern dominance, we tested four different models labelled from 0 to 3:

- (0) a constant model;
- (1) a linear trend;
- (2) a second-order polynomial, called quadratic model;
- (3) a sinusoidal fit with a period of the same order as that of the temporal coverage of the series.

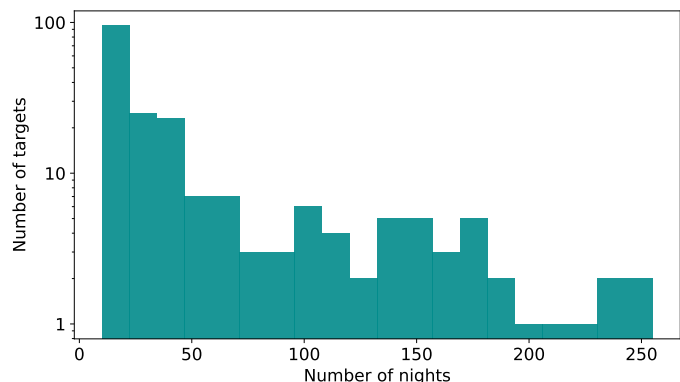


Fig. 5: Distribution of observed nights.

We use statistical tests to determine whether a long-term correction should be applied before searching for short-term periodic signatures.

### 4.1. Correction of the secular acceleration

Perspective or secular acceleration (van de Kamp 1977) is a geometric effect that results in a variation in the radial component of velocity (see e.g. Fig. 3 in Zechmeister et al. 2009), measured for the first time by Kuerster et al. (2003) on the Barnard star. We applied a secular acceleration ( $\dot{v}$ ) correction on RV time series as

$$\dot{v} = \frac{dv}{dt} = \frac{\mu_{RA}^2 + \mu_{DEC}^2}{\pi}, \quad (1)$$

where  $\mu_{RA}$  and  $\mu_{DEC}$  are the right ascension and declination components of the proper motion, and  $\pi$  is the parallax.

The uncertainties associated with the Gaia measurements of proper motions and parallaxes are much smaller (by a factor of

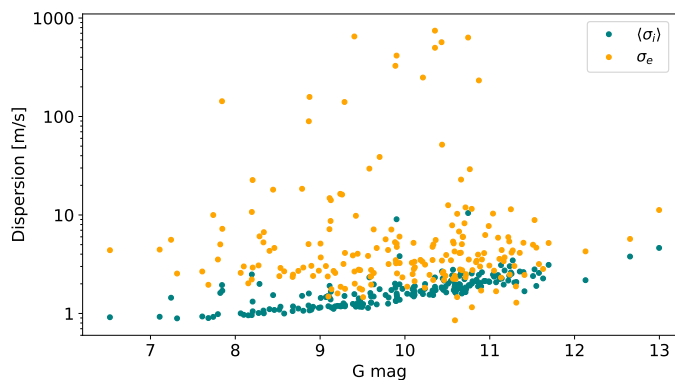


Fig. 6: Averaged internal error  $\langle\sigma_i\rangle$ :  $\sigma_i$  (green) and RV dispersion  $\sigma_e$  (orange) expressed in m/s vs G-band magnitude.

10) than the uncertainties previously used in Zechmeister et al. (2009) and Bonfils et al. (2013b), and derived from Van Leeuwen (2007). Consequently, the values of the acceleration correction terms are of the same order as in these previous works, but the associated uncertainties are now negligible compared to the photon noise.

#### 4.2. Excessive RV dispersion: Limits of the constant model

In this first step we measure the variability of the RV time series as in Bonfils et al. (2013b) to determine whether the constant model is sufficient to explain the dispersion. Fig. 6 shows, for each star, the averaged internal error ( $\langle\sigma_i\rangle$ ,  $\sigma_i$ , which is the quadratic sum of  $svrad$ , in green) and the measured RV dispersion ( $\sigma_e$ , in orange) as a function of G-band magnitude.

For the majority of the stars in our sample, the RV series show an excessive dispersion that cannot be explained by internal noise alone, and we observe  $\langle\sigma_i\rangle \leq \sigma_e$  in most cases, as in Bonfils et al. (2013b). To characterise this excessive dispersion, we performed a chi-squared test, with its  $\chi_0^2$  value and probability  $P(\chi_0^2)$  between the dispersion and the constant model. A low value of  $P(\chi_0^2)$  highlights that the model tested is not sufficient to explain the dispersion measured, even taking uncertainties into account.

Excessive variability can also be expressed as in Cumming et al. (1999), Cumming et al. (2008), Zechmeister et al. (2009), and Bonfils et al. (2013b), using the definition of  $Fvalue_0$  and its probability  $P(Fvalue_0)$ :

$$Fvalue_0 = \frac{\sigma_e^2}{\langle\sigma_i\rangle^2}. \quad (2)$$

As explained in the previous works cited, a high  $Fvalue_0$  (and low  $P(Fvalue_0)$ ) indicates a dispersion that cannot be explained by internal errors. These two complementary tests measure variability in two slightly different ways:  $Fvalue_0$  evaluates average dispersion, while the impact of outliers is reduced in the  $\chi^2$  test. An outlier with very high uncertainties will have less impact on the rest of the dataset in the  $\chi^2$  computation than in the  $Fvalue_0$  computation. Consequently,  $P(\chi_0^2)$  is lower than  $P(Fvalue_0)$ , as announced by Zechmeister et al. (2009). In our study, since the series are cleaned of points with aberrant uncertainties,  $P(\chi_0^2)$  is only slightly lower than  $P(Fvalue_0)$  as shown in Fig. 7.

To consider that a constant model cannot explain the dispersion of the dataset, we adopt the same threshold as Zechmeister

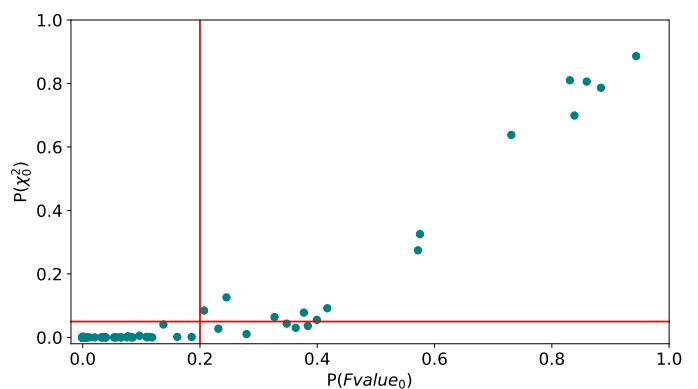


Fig. 7:  $P(\chi_0^2)$  vs  $P(Fvalue_0)$  for the constant model. The red vertical (resp. horizontal) line corresponds to the 0.2 (resp. 0.05) threshold adopted for  $P(Fvalue_0)$  (resp.  $P(\chi_0^2)$ ).

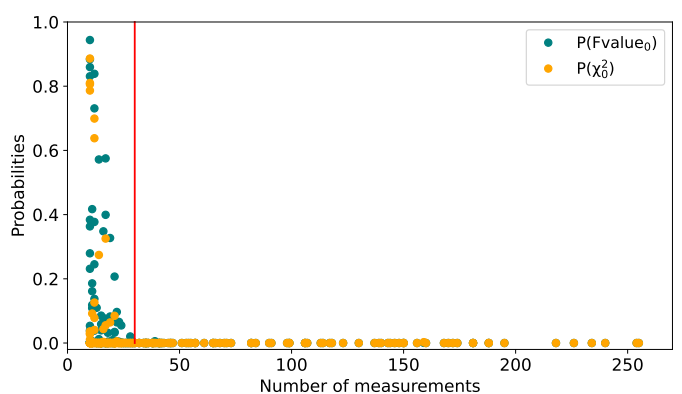


Fig. 8:  $P(Fvalue_0)$  (orange) and  $P(\chi_0^2)$  (green) as a function of the number of measurements for each star. The probabilities fall to zero after the threshold of 30 measurements (highlighted by the red vertical line).

et al. (2009) and Bonfils et al. (2013b):  $P(\chi_0^2) < 0.05$ . As shown in Fig. 7, this corresponds statistically to an equivalent threshold of  $P(Fvalue_0) < 0.2$ . Figure 8 shows  $P(\chi_0^2)$  and  $P(Fvalue_0)$  for our whole sample as a function of the number of measurements. All the values of these tests and the parameters used are listed in Table B.6. The probability that the dispersion measured in each data series is explained solely by internal errors associated with each measurement falls to zero for all time series with more than 30 measurements.

The question is whether this is due to an underestimation of the errors or to the presence of a real signal in each RV time series. The first hypothesis is simply verified by simulating the uncertainties required to obtain a uniform distribution of  $P(\chi^2)$  and  $P(Fvalue)$ . We obtain simulated uncertainties that are ten times greater than those calculated in Sect. 3.1, which is inconsistent with the characterisation of the precision obtained with HARPS. Finally, we conclude that a signal (planetary system and/or activity impact) is present in almost all RV time series. This result is consistent with the occurrence rate of  $0.9^{+0.04}_{-0.03}$  planets ( $R < 4 R_{\oplus}$  and  $P < 50$  days) per small star established on the Kepler missions (e.g. Dressing & Charbonneau 2013, 2015), but also with the  $1.32^{+0.33}_{-0.32}$  rocky planets ( $M < 10 M_{\oplus}$  and  $P < 100$  days) obtained on the RV survey of CARMENES (Sabotta et al. 2021).

### 4.3. Long-term signals

Following the approach of Zechmeister et al. (2009), we begin the characterisation of excessive dispersion by searching for long-term variations in the time series.

#### 4.3.1. Fitting method and statistical test

**Fitting method:** The models tested in this section are fitted with a least-squares optimisation algorithm from Limited memory Broyden-Fletcher-Goldfarb-Shanno (L-BFGS-B) (Byrd et al. 1995; Zhu et al. 1997). We use the diagonal terms of the covariance matrix associated with the parameters fitted as uncertainties, considering them uncorrelated.

**Reduced chi-squared ( $\chi^2_*$ ):** The  $\chi^2$ -probability is used to check whether the proposed long-term model is sufficient to explain the time series. Since we expect this to rarely be the case, we instead compare the improvements brought by the models with each other. As in Mignon et al. (2023), we use a test on the ratio of the reduced  $\chi^2$  values of two models defined as

$$F_{red\ j/k} = \frac{\chi_{k*}^2 - \chi_{j*}^2}{\chi_{k*}^2}, \quad (3)$$

where  $\chi_{j*}^2$  (respectively  $\chi_{k*}^2$ ) is the reduced chi-squared value of model j (resp. k). This ratio is close to 1 when model j brings a major improvement compared to model k. Conversely, a negative value or a value close to 0 indicates that the improvement is either negligible or nonexistent.

**F test:** We use also the F test to verify the improvement made by the model tested, as presented in Cumming et al. (1999) and Cumming et al. (2008):

$$F_{j/k} = (d_{free}) \cdot \frac{\chi_k^2 - \chi_j^2}{\chi_j^2}. \quad (4)$$

Here  $d_{free}$  is the degree of freedom of model j, and  $\chi_k^2$  and  $\chi_j^2$  are respectively the chi-squared values of models k and j. We compute its probability as in Bonfils et al. (2013b) (constructed on Beta functions) to express the significance of the improvement. A very low probability expresses a significant improvement and a probability near 100% expresses a non-significant improvement.

#### 4.3.2. Linear model

We automatically examine if the RV time series of each star is dominated by a long-term linear trend pattern (identified by the index 1). This signal can be caused by the presence of a massive companion with a large separation with a poorly covered orbit. We consider that this model dominates the RV time series when the following criteria are met:

- the ratio  $F_{red\ 1/0}$  is higher than the ratio of the other models (including the two other types of models described below  $F_{red\ 2/0}$  and  $F_{red\ 3/0}$ ), and is above our 0.2 threshold;
- the value of the  $P(F_{1/0})$  is under the threshold of 0.05;
- the ratio  $F_{red\ 2/1}$  is negative.

These criteria guarantee the improvement (and its significance) provided by the linear model compared with the other models tested (described below). The 16 targets whose RV time

series is dominated by a linear trend are listed in Table B.2. This slope is subtracted before proceeding to the frequency analysis in the next section. Figure 9 shows the example of GJ 864.

#### 4.3.3. Quadratic model

At the same time as the trend search, we also test a second-degree polynomial model (identified by the index 2). Such a signal may reflect the presence of an intermediate-period companion that is better covered than in the case of the trend, or it may be caused by a variation in stellar activity on a scale of several years. A second-degree polynomial is considered to be dominant in the RV time series when these criteria are met:

- the ratio  $F_{red\ 2/0}$  is higher than the ratio of the other models ( $F_{red\ 1/0}$  and  $F_{red\ 3/0}$ ), and is above the 0.2 threshold;
- the value of the  $P(F_{2/0})$  and  $P(F_{2/1})$  are under the threshold of 0.05;
- the ratio  $F_{red\ 2/1}$  is positive.

Once again these criteria guarantee the significant improvement provided by the quadratic model compared with the others. This corresponds to the 29 stars listed in Table B.2. The fitted second-degree polynomial is subtracted before proceeding to the frequency analysis in the next section. Figure 9 shows the example of GJ 680.

#### 4.3.4. Sinusoidal model

To complete the systematic analysis of the long-term variations, we test one last model: a sinusoidal function with and without a linear trend (identified by the index 3). Its period is of the order of the duration of the RV time series (shorter periods are identified during frequency analysis), and its amplitude is of the order of the peak-to-peak RV variation of the time series. We chose a sinusoidal function instead of a cubic trend in order to detect a wider range of long-term variations and minimise the impact of a bad sampling on the model chosen. We note that this step does not represent a definitive diagnosis of these systems, which are analysed in Sect. 6 through a Keplerian analysis. Given the sporadic sampling of RV time series, testing the sinusoidal model helps avoid incorrect automated linear or quadratic trend corrections. In particular, an RV series dominated by the signature of the presence of a massive companion can be misinterpreted as a simple trend in cases of very poor sampling, resulting in an incomplete phase coverage. The choice for this model 3, between a sinusoidal function or the sum of a linear trend and a sinusoid, is made by selecting the solution giving the smallest error computed in using the covariance matrix. The sinusoidal model is considered as dominant in the RV time series when these criteria are met:

- the ratio  $F_{red\ 3/0}$  is higher than the ratio of the other models ( $F_{red\ 1/0}$  and  $F_{red\ 2/0}$ ), and is above the threshold of 0.2;
- the value of  $P(F_{3/0})$ ,  $P(F_{3/1})$ , and  $P(F_{3/2})$  are under the threshold of 0.05.

Following these criteria, the RV time series of 12 stars are dominated by a sinusoidal pattern (listed in Table 3) and Fig. 9 shows the example of GJ 832. The signal identified corresponds to a stellar or massive planet companion already discovered for seven of them (see references in Table 3). We finally highlight five new massive candidates and/or binary systems described in Sect. 6 of this paper. The targets flagged with an asterisk in Table 3 are those dominated by the sum of a sinusoidal function and a linear trend. These time series were corrected for linear trend before performing the analysis described in the next section.

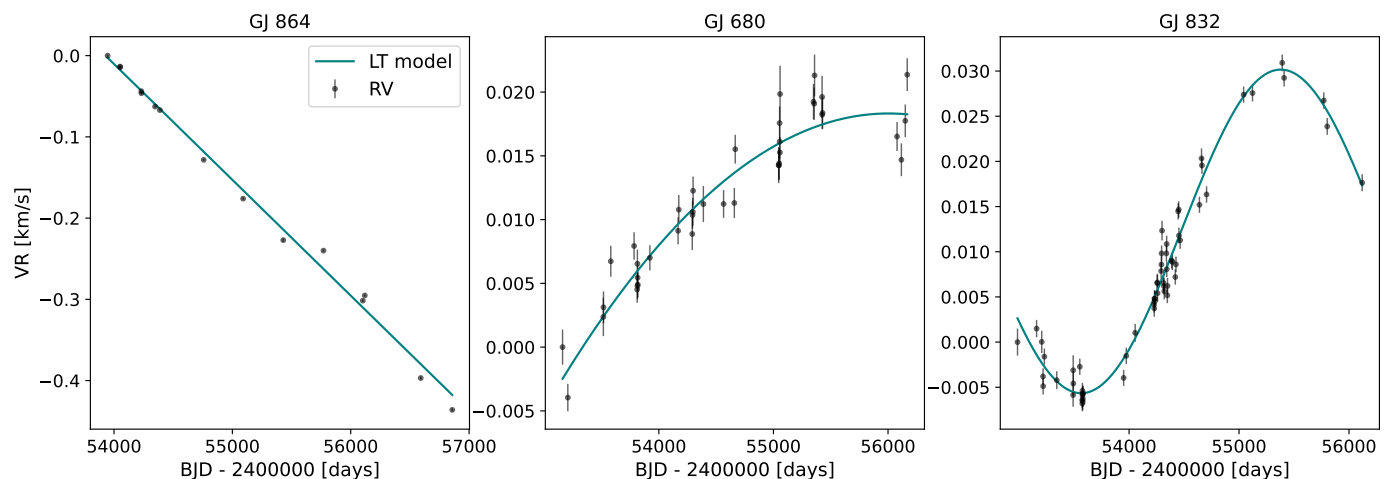


Fig. 9: Example of detection of dominant long-term signal: GJ 864 (*left panel*) as an example of linear trend, GJ 680 (*middle panel*) for the quadratic trend, and GJ 832 (*right panel*) for the sinusoidal function.

Table 3: Sinusoidal model

Star	Period (d)	K (m/s)	Ref	
GJ 179*	b	2288	22.10	Howard et al. (2010)
GJ 317	b	762	76.24	Johnson et al. (2007)
GJ 676A*	b	1056	166.47	Forveille et al. (2011)
GJ 832	b	3687	17.91	Bailey et al. (2008)
GJ 849*	b	1924	29.90	Butler et al. (2006)
GJ 3307		3539	970.41	this paper
GJ 4001		2672	571.92	this paper
GJ 4254*		1453	4595.92	this paper
GJ 4303		1267	47.92	this paper
GJ 9425*	c	1800	31.02	Moutou et al. (2011)
	b	700		Moutou et al. (2011)
GJ 9482*	b	6700	75.52	Segransan et al. (2011)
GJ 9588*		620	540.65	this paper

**Notes.** Targets dominated by a sinusoidal function. The last column gives the companion discovery reference, including the five in this work. Targets flagged with an asterisk correspond to those dominated by a linear trend in addition to the sinusoidal function.

#### 4.4. RV offset from HARPS fibre change

As discussed in Sect. 3.2, the change of HARPS fibres (in May 2015) induces an offset in the RV time series, which is different for each star and depends on the spectral type (Lo Curto et al. 2015; Trifonov et al. 2020). As a result, the RV series of the 37 stars observed sufficiently before and after the change of fibres consist of two series extracted from two templates that can be considered as coming from two distinct instruments (HARPS03 and HARPS15). For these stars, we fit an additional free parameter at the date of the change of fibres to each model tested. The values of this parameter are listed in Table B.3 with the corresponding model.

#### 4.5. Conclusion of the long-term analysis

Among the 200 RV time series in our sample, 57 (28.5%) are dominated by a long-term trend. Among these, we corrected 49

series; we subtracted a linear function from 20 series (including 4 where it was necessary to model a sinusoid to properly identify the trend), and subtracted a quadratic function from 29 others. RV time series dominated by a sinusoidal function are individually examined in the next section.

After these corrections, we recomputed the  $Fvalue_0$  ratio to estimate the excessive dispersion after subtracting the long-term pattern. Only 5% of the RV time series have an  $Fvalue_0 < 3$  (10 out of 200). This indicates that even after subtracting the long-term trend, the RV time series still exhibit excessive variability, certainly due to shorter-term periodic or stochastic signals.

## 5. Frequency analysis

Once the RV time series are corrected for the long-term signal, identified in the previous section, we analyse the higher-frequency signals corresponding to periodic or quasi-periodic variability (Keplerian or activity signals). Our aim here is not to optimise the identification of individual planetary systems, but to carry out a homogeneous search that can be used for subsequent statistical analysis. The signal detections we report in this section are compared with previously published systems.

### 5.1. Method

#### 5.1.1. Generalised Lomb-Scargle periodogram

For each star we compute a generalised Lomb-Scargle periodogram (GLS), proposed by Zechmeister & Kürster (2009) and based on Lomb (1976) and Scargle (1982). For a given period, the GLS gives the generalised power corresponding to the lowest  $\chi^2$  obtained with a sinusoidal function at that period. We compute the GLS from the minimum period of 1.6 days up to the maximum period of twice the time coverage of the RV time series. We summarise the main steps in our procedure as follows:

- We compute the GLS periodogram of the observation window on a synthetic data series with a regular sampling of one point per night, with an arbitrary value of 1 for each observed night and 0 for the others; we reject any peak in the GLS of the original series if its period corresponds to that of a peak of the window function (and within an interval corresponding to the width of this peak).

- Once a peak is identified in the GLS, we reject aliases caused by observation frequencies.
- The false alarm probability (hereafter FAP) is computed using a classical bootstrap method: we generate 1000 time series with dates similar to those of the original series, but we assign each of them a random RV value from the set of RV values in the original series; we then compute the GLS for each of these arranged series. The resulting periodograms are then sorted in ascending order of the power of the main peak, and the FAP level of the original series corresponds to its position in this ranking; for example, a FAP level of 1% corresponds to a ranking in the tenth position.

### 5.1.2. Keplerian analysis

We apply an iterative method to detect systems with multiple signals. For each star, as described above, we compute the GLS periodogram, determine the FAP level of its maximum peak, and verify that it is not caused by the sampling (window function or alias). If the FAP level of the peak is below the 1% threshold, we fit a Keplerian signal to the corresponding period by using a L-BFGS-B minimisation method. We use the procedure in the set of functions proposed in the Python script of DACE<sup>5</sup> by Delisle et al. (2016).

After subtracting the fitted Keplerian signal, we repeat the procedure on the residuals: computing a new GLS, checking for sampling effects, and determining the FAP level. If the FAP level is again below the 1% threshold, we fit a new model with an additional Keplerian to the original series. We stop this iterative process when there are no significant peaks left in the GLS of the residuals, if the Keplerian fitting fails to converge, or if the RMS of the residuals is below the internal noise parameter ( $\langle\sigma_i\rangle$ ).

## 5.2. Results

We obtain a total of 120 significant periodic signals, resulting in 108 Keplerian models (12 fittings did not converge) across the time series of 52 stars.

### 5.2.1. Previously known planetary systems

We identify the periodic signals corresponding to previously published planetary systems by cross-referencing them with the NASA Exoplanet Archive.<sup>6</sup> In Table 4 we list the 51 signals identified among the 108 peaks.

In this table, the periods in Col. 3 represent the values returned by our Keplerian fit (rather than the published ones) with the corresponding FAP level of the peak in the GLS given in Col. 2. Since the FAP level corresponds to its ranking, a value of 0 indicates that none of the 1000 permuted series yielded a peak as strong as that of the original series, implying a true FAP level below  $10^{-3}$ . The first column indicates the name of the recovered planet, and the last column provides the reference for its discovery. For multi-planetary systems the signals are listed in order of the successive iterations, and are indicated by the corresponding letter of the planet in the literature. The semi-amplitudes (K) of the fitted Keplerian signals are provided in Col. 4, and we also specify the long-term model applied to data before the Keplerian analysis (Col. 5). Several published planets are not retrieved by our analysis; according to the NASA Exoplanet database, there

are 78 published planets orbiting the 200 M dwarfs in our sample. The reasons are diverse and are discussed in detail in Sect. 7. We summarise them as follows:

- when the discovery is based on an accumulation of data from other instruments (HIRES and/or CARMENES);
- when the period is shorter than the lower limit of 1.6 days used here;
- when a detailed analysis of the impact of stellar activity is required (Gaussian process).

In addition, two long-period planets, GJ 317 c (Johnson et al. 2007) and GJ 676A c (Sahlmann et al. 2016), are not recovered because their orbital periods are longer than twice the duration of our data.

### 5.2.2. Stellar activity

M dwarfs are often active stars (Hawley & Pettersen 1991; Delfosse et al. 1998b; Morin et al. 2008; Newton et al. 2016; Astudillo-Defru et al. 2017a), and their variability impacts RVs. It is therefore possible to confuse stellar activity signal with a planetary signal.

The surface heterogeneities of the star (spot and plage contrasts, magnetic inhibition of surface convection) shift and/or deform stellar lines. Due to stellar rotation, stellar activity can thus add a quasi-periodic signal at the rotation period (or one of its harmonics) in the RV time series (see e.g. Queloz et al. 2001; Robertson et al. 2014). If the rotation period is known or identified, this signal is often modelled and subtracted using a Gaussian process regression (Haywood et al. 2014; Rajpaul et al. 2015; Aigrain & Foreman-Mackey 2022). However, most of the rotation periods of the M dwarfs in our sample are unknown, and performing such a process is therefore outside the scope of this study.

However, it is well known that the activity signal on M dwarfs can remain coherent over a long period and can create a peak in the periodograms. A periodic function can then model it, ultimately leading to false positive detections such as GJ 832 c (Wittenmyer et al. 2014) and GJ 9066 b (Feng et al. 2020), both recently ruled out.

Therefore, we compare the periods of the 57 unidentified signals with the stellar rotation periods published in the literature (determined through photometric or chromospheric emission variability). An RV signal detected at a period close to the published rotation period of the star (within 10%) is therefore attributed to a rotational signature. In addition, we perform a frequency analysis of three chromospheric proxies (the H- and K-bands of CaII, the sodium doublet, and the H $\alpha$  line) from each spectrum series in our sample. Finally, an RV signal detected at a period close (within 10%) to a periodic signal identified in the chromospheric indices is also conservatively attributed to a rotational signature. Out of the 57 remaining unidentified signals in the RV data, 35 are attributed to the stellar rotation signature of 23 stars, listed and detailed in Table B.4.

### 5.2.3. Non-identified signals

After these two steps 22 unidentified periodic signals remain. We attribute them to the following different origins:

- an unpublished or unidentified stellar rotation, requiring a more complete study, as was the case for GJ 581 (Robertson et al. 2014);

<sup>5</sup> <https://dace.unige.ch/tutorials/?tutorialId=3>

<sup>6</sup> <https://exoplanetarchive.ipac.caltech.edu/index.html>

Table 4: Planetary systems previously discovered and recovered.

Star	FAP	Period (d)	K (m/s)	Correction	Discovery reference
GJ 54.1 c	0.0	3.0599±0.0002	1.91	-	Astudillo-Defru et al. (2017b)
d	0.0	4.6566±0.0003	1.69	-	Astudillo-Defru et al. (2017b)
b	0.0	2.02101±0.00005	1.61	-	Astudillo-Defru et al. (2017b)
GJ 163 b	0.0	8.6300±0.0003	5.70	-	Bonfils et al. (2013a)
c	0.0	25.608±0.006	3.83	-	Bonfils et al. (2013a)
d	0.0	642.15±1.65	3.40	-	Bonfils et al. (2013a)
GJ 176 b	0.0	8.7754±0.0002	4.14	-	Forveille et al. (2009)
GJ 179 b	0.0	2321±500	23.87	-	Howard et al. (2010)
GJ 180 b	0.0	17.124±0.006	4.26	-	Feng et al. (2020)
GJ 221 c	0.0	125.44±0.09	7.27	quadratic	Lo Curto et al. (2013)
b	0.0	3.87±0.01	4.32	-	Lo Curto et al. (2013)
GJ 229 c	0.0	121.49±0.07	7.23	quadratic	Feng et al. (2020)
b	0.0	528.17±6.7	1.26	-	Feng et al. (2020)
GJ 273 b	0.0	18.661±0.004	1.44	-	Astudillo-Defru et al. (2017c)
c	0.0	4.7230±0.0002	1.14	-	Astudillo-Defru et al. (2017c)
GJ 393 b	0.0	7.0223±0.0008	1.04	-	Amado et al. (2021)
GJ 433 b	0.0	7.3721±0.0006	3.05	-	Delfosse et al. (2013)
GJ 447 b	0.0	9.861±0.002	1.68	quadratic	Bonfils et al. (2018b)
GJ 480 b	0.002	9.548±0.005	5.61	quadratic	Feng et al. (2020)
GJ 536 b	0.0	8.7089±0.0004	3.59	linear trend	Suárez Mascareño et al. (2017a)
GJ 551 b	0.001	11.187±0.001	1.42	quadratic	Anglada-Escudé et al. (2016)
GJ 581 b	0.0	5.36856±0.00006	12.77	-	Bonfils et al. (2005)
c	0.0	12.914±0.001	3.25	-	Udry et al. (2007)
e	0.0	3.1489±0.0001	1.66	-	Udry et al. (2007)
GJ 628 d	0.0	217.914±0.305	2.48	-	Astudillo-Defru et al. (2017c)
c	0.0	17.865±0.003	2.10	-	Astudillo-Defru et al. (2017c)
b	0.0	4.8872±0.0003	1.63	-	Wright et al. (2016)
GJ 667C b	0.0	7.2005±0.0001	3.97	linear trend	Delfosse et al. (2013)
f	0.0	38.948±0.03	1.07	-	Anglada-Escudé et al. (2013)
c	0.0	28.151±0.005	1.77	-	Delfosse et al. (2013)
GJ 674 b	0.0	4.69507±0.00002	8.75	-	Bonfils et al. (2007)
GJ 676A b	0.0	1039.3±0.6	-	linear trend	Forveille et al. (2011)
GJ 752A b	0.0	106.34±0.08	2.81	-	Kaminski et al. (2018)
GJ 832 b	0.0	3684±97	17.39	sinusoidal	Bailey et al. (2008)
GJ 849 b	0.0	1796±3	20.8	sinusoidal	Butler et al. (2006)
GJ 876 b	0.0	61.0320±0.0003	219.01	linear trend	Delfosse et al. (1998a)
c	0.0	30.2310±0.0002	82.11	-	Marcy et al. (2001)
d	0.001	1.93789±0.00001	5.90	-	Rivera et al. (2005)
GJ 1132 b	0.0	1.6287±0.0002	3.13	-	Berta-Thompson et al. (2015)
c	0.0	8.933±0.006	2.49	-	Bonfils et al. (2018a)
d	0.0	177±2	3.3	-	Bonfils et al. (2018a)
GJ 3053 b	0.0	24.84±0.03	5.36	-	Dittmann et al. (2017)
c	0.007	3.7816±0.0008	2.07	-	Ment et al. (2019)
GJ 3293 b	0.0	30.611±0.006	14.10	-	Astudillo-Defru et al. (2017c)
c	0.0	123.4±0.1	24.44	-	Astudillo-Defru et al. (2017c)
d	0.0	48.16±0.03	5.33	-	Astudillo-Defru et al. (2017c)
GJ 3323 b	0.002	5.3551±0.0007	2.55	-	Astudillo-Defru et al. (2017c)
c	0.001	40.36±0.07	1.37	-	Astudillo-Defru et al. (2017c)
GJ 3341 b	0.0	14.208±0.005	2.83	-	Astudillo-Defru et al. (2015)
GJ 3634 b	0.0	2.6458±0.0002	5.48	quadratic	Bonfils et al. (2011)
GJ 9018 b	0.0	15.79±0.02	4.64	-	Tuomi et al. (2014)

**Notes.** The 0.0 FAP value corresponds to a value under the  $10^{-3}$  threshold.

– a long-term magnetic variability, of the order of a few hundred days or more, leading to a long-term RV variation (see analysis in our companion paper [Mignon et al. 2023](#));

– an unidentified planetary or binary system.

These remaining 22 signals are listed in Table 5, where we also indicate the dominant long-term model found in the previous section.

Table 5: Periodic signal in RV times series whose origin is not yet identified (discussed individually in Sect. 6).

Star	FAP	Period (d)	K (m/s)	Correction
GJ 300	0.0074	8.33	7.14	quadratic
GJ 317	$< 10^{-9}$	314.40	38.95	-
	$9 \cdot 10^{-9}$	236.46	21.65	-
GJ 361	$2.4 \cdot 10^{-8}$	28.94	4.94	-
GJ 393	$4.4 \cdot 10^{-6}$	775.94	1.43	-
	$7.3 \cdot 10^{-5}$	51.9	1.73	-
GJ 569A	0.00073	14.38	11.17	linear
GJ 588	0.0021	21.02	2.5	-
	0.0067	24.19	2.3	-
GJ 654	0.00019	260.83	1.81	-
GJ 699	$6.3 \cdot 10^{-8}$	373.09	2.5	-
GJ 739	0.00066	138.73	4.06	linear
GJ 754	0.00061	250.43	3.3	-
	0.0031	16.99	1.9	-
GJ 846	0.0049	10.80	4.5	-
GJ 880	0.0081	40.17	2.32	quadratic
GJ 3307	$7.4 \cdot 10^{-6}$	3539.87	1271.02	-
GJ 4001	$1.4 \cdot 10^{-6}$	4274.92	608.94	-
GJ 4254	$< 10^{-9}$	1453.68	3393.67	linear
GJ 4303	$1.8 \cdot 10^{-9}$	1267.26	45.06	-
	0.0012	17.63	11.1	-
GJ 9588	$< 10^{-9}$	558.72	-	linear

## 6. Candidates

In this section we focus on the remaining 22 Keplerian signals as well as the massive candidates detected with the sinusoidal function in the long-term analysis. The spectral types of the M dwarfs discussed below are taken from (Gaidos et al. 2014). The RV time series derived from the template-matching method of the respective stars are imported into the DACE<sup>7</sup> platform, where we use the Keplerian analysis of Delisle et al. (2016) and the analytical FAP computation routines from Baluev (2008). The fitted parameters on the platform are listed in Table 5.

### 6.1. Stellar or brown dwarf companions

With a temporal coverage of nearly 20 years, HARPS is an ideal instrument for detecting, monitoring, and completing the orbits of long-period companions. In this section we provide detailed information on the high-amplitude RV signals found during the long-term and Keplerian analyses. For the specific analysis of these massive companions, we utilise a software called *orvara* (Brandt et al. 2021), which is a Markov chain Monte Carlo (MCMC) programme designed to fit Keplerian orbits to various combinations of proper motion anomalies, absolute and relative astrometry, and radial velocities. It uses the Hipparcos-Gaia Catalog of Accelerations (HGCA, Brandt (2021)), which relies on a combination of the Hipparcos and Gaia EDR3 catalogues. It has been cross-checked and adjusted to address any discrepancies and ensure that all proper motions in the Gaia EDR3 are accurately aligned; this enables us to obtain precise dynamical masses and orbital elements. We are using a modified *orvara* version<sup>8</sup> that incorporates extra priors on orbital periods and

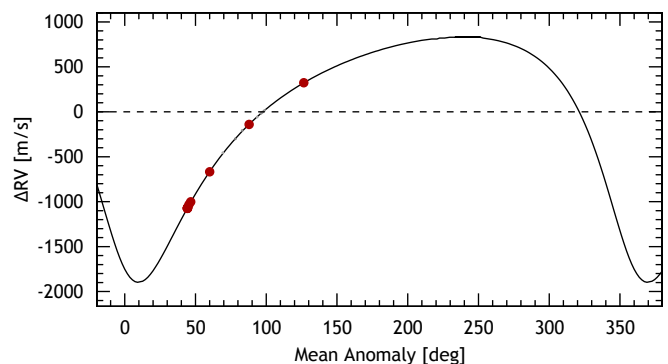


Fig. 10: GJ 3307 RV phase-folding

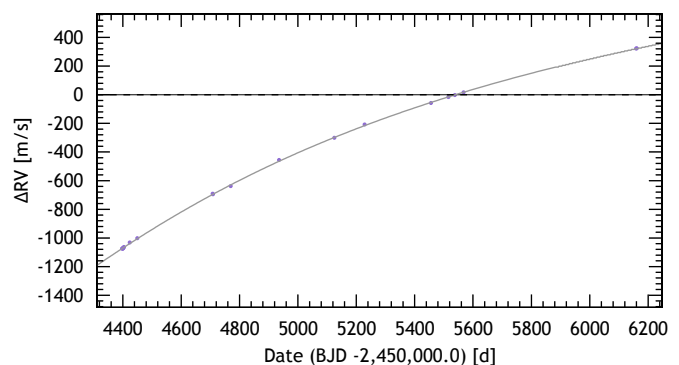


Fig. 11: GJ 3307 RV time series and best fitting orbit model.

semi-major axes, along with primary mass and stellar jitter priors from the original code, to enhance accuracy and improve orbital element consistency, especially for intermediate-separation binaries.

#### 6.1.1. GJ 3307

GJ 3307 is an M2V dwarf at a distance of  $\sim 23$  pc, one of the most massive stars in our sample ( $0.63 \pm 0.01 M_{\odot}$ ). Our modelling of its RV time series converges to a large-amplitude sinusoidal function (peak-to-peak variation of 1.6 km/s). By using the estimated period from Sect. 4.3.4 as a prior to the Keplerian fit on DACE, we obtain a minimum period of  $8396 \pm 52300$  days and a minimum mass of  $0.091 M_{\odot}$  (see Fig. 10). The orbit is not well constrained by the 20 HARPS data points taken between October 2007 and September 2012 (a time coverage of 1800 days), but the fitted signal can be subtracted from the RV series shown in Fig. 11, and the periodogram of the residuals shows no significant peak. Therefore, the companion is likely a very low-mass star with a typical orbital period of about 20 years or longer, and should be resolvable with high angular resolution imaging. The FWHM of the CCF for this star remains stable over time, indicating that this system is not an SB2 and that the contrast in luminosity between the two components must be significant. Since this star has not been observed by Hipparcos, we are not able to use *orvara* to combine the astrometry and the RV to extract the system's inclination and the true companion mass.

<sup>7</sup> <https://dace.unige.ch/tutorials/?tutorialId=3>

<sup>8</sup> <https://github.com/nicochunger/orvara/tree/period-prior>

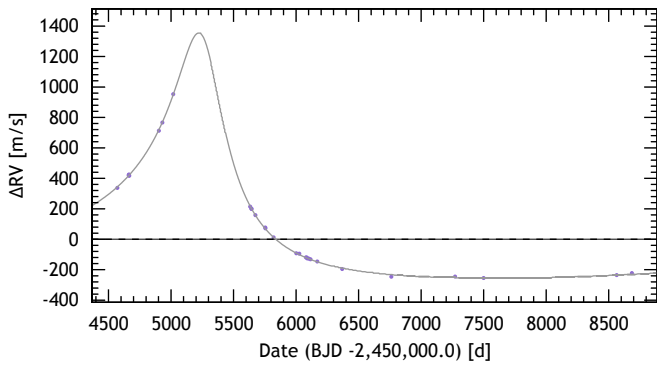


Fig. 12: GJ 4001 HARPS RV measurements and best fitting orbit model.

### 6.1.2. GJ 4001

GJ 4001 (HIP 84652) is classified as M1V and is in the top 10% of the most massive stars in our sample, with a determined mass of  $0.66 \pm 0.03 M_{\odot}$ , also classified as a K7V in previous studies (Stephenson 1986). Once again, the FWHM of the CCF remains stable over time, indicating that GJ4001 is not an SB2 system. We use the period estimated in Sect. 4.3.4 as a prior in the Keplerian fitting on DACE, and obtain a minimum projected mass  $42.49 M_J$  with a period of  $7378 \pm 84$  days and a high eccentricity ( $e = 0.717 \pm 0.005$ ). Since measurements were taken over a 4115-day time span, slightly more than half of the period is covered, but fortunately the passage to periastron was well monitored. With a separation of  $6.6 \pm 0.17$  au at a distance of 22.5 pc (Gaia DR2 Collaboration et al. 2018), the maximum apparent separation of the system is around 290 mas, making it an ideal target for high angular resolution observations and also for astrometric detection with Gaia. Kervella et al. (2019), in studying perturbations in proper motion using HIPPARCOS and Gaia DR2 measurements, found a possible astrometric signal for this system corresponding to a companion of  $\sim 54 M_J$  at a separation of 1.28 au at the time of the Gaia DR2 observation windows. Using *orvara*, we obtain an inclination of 8.6 degrees, indicating that the system is seen from the pole and suggesting a fairly massive companion of  $362 M_J$ .

### 6.1.3. GJ 4254

GJ 4254 (HIP 109084) is a massive M0V star ( $0.79 \pm 0.02 M_{\odot}$ ) in our sample, also classified as a K7V in Bidelman (1985). The 30 HARPS measurements, shown in Fig. 13, exhibit a peak-to-peak variation of 3.7 km/s. Using the DACE platform, the Keplerian fit converges to a period of  $917.4 \pm 0.8$  days and a semi-amplitude of  $K = 3.18 \pm 0.08$  km/s, corresponding to a companion mass of  $m \cdot \sin i = 0.1 M_{\odot}$ . Unfortunately, for this system the periastron passage has not been sufficiently monitored to constrain the eccentricity (0.65 in the solution presented in Fig. 13). The true amplitude of the signal is therefore strongly underestimated in our fit. This source would require additional measurements, ideally at a time when the RV separation is greatest, to identify the two individual components in the CCF.

### 6.1.4. GJ 4303

GJ 4303 (HIP 113201AB) is a M1 system with a mass of  $0.54 \pm 0.01 M_{\odot}$ , at a distance of 23.8 pc. The system has been moni-

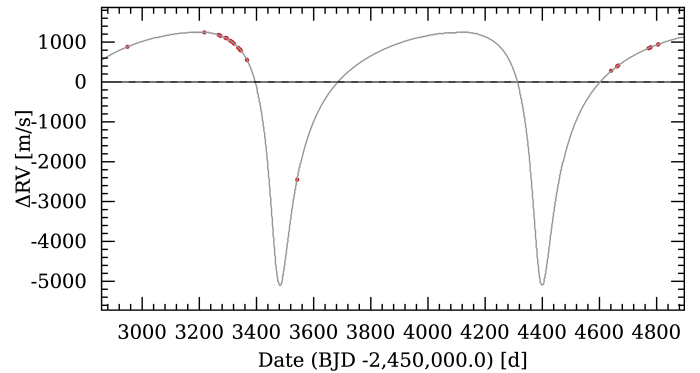


Fig. 13: GJ 4254 HARPS RV measurements and best fitting orbit for the first Keplerian model.

tored using direct imaging with SPHERE, astrometry with HIPPARCOS and RV measurements with HARPS by Biller et al. (2022) in recent years. They detected a low-mass stellar companion of  $0.145 M_{\odot}$  with a period of 33 years. In this study we use 73 of the 76 public RV measurements of HARPS, excluding the last 3 measurements taken after the change of fibres as they do not allow the construction of a proper template. We fit the orbit using priors from our long-term signal analysis. We obtain a period of  $11709 \pm 2030$  days, with an eccentricity of  $0.66 \pm 0.05$ , and a companion mass of  $m \cdot \sin i \sim 0.07 M_{\odot}$ , both consistent with Biller et al. (2022). Additionally, the periodogram of the residuals shows two significant peaks at 8.8 and 17.6 days, once again consistent with the stellar rotation published in Biller et al. (2022).

### 6.1.5. GJ 9482

GJ 9482 is an M0V star ( $0.68 \pm 0.01 M_{\odot}$ ) with a massive planet of  $m \cdot \sin i = 9 \pm 6 M_J$  and a period of  $17337 \pm 15512$  days, detected in RV by Segransan et al. (2011). For this star, the dominant long-term model is a sinusoidal function, with a fitted period of 6700 days and an offset value of  $-27.1 \pm 15.7$  m/s, as this target was monitored both before (41 nights) and after (13 nights) the fibre change. However, the Keplerian fit performed during the iterative search for signals did not converge. Using the DACE platform, we obtain a good solution (with a residual dispersion of 3.39 m/s) that constrains the period and mass much better than in Segransan et al. (2011), thanks to the addition of 13 new data points (2015.08-2019.08). We obtain a companion mass of  $m \cdot \sin i = 4.58 \pm 0.09 M_J$  and a orbital period of  $3659 \pm 4$  days. However, in this solution the RV offset at the time of the fibre change is  $39.2 \pm 0.6$  m/s. The correction of the time series with an incorrect offset value explains why the automatic Keplerian fitting did not converge. This poor estimation of the offset is due to the high eccentricity of the orbit ( $e = 0.660 \pm 0.004$ ), modelled at this step as a sinusoidal function. This case, with a high-eccentricity orbit, highlights a limitation of our systematic study of long-term signals which do not converge, and so must be treated individually. Using *orvara*, the inclination is not well constrained ( $i = 90_{-21}^{+24}$ ), but it is sufficient to confirm that the system is observed close to edge-on, giving a maximum mass of the planet of  $4.6 M_J$ .

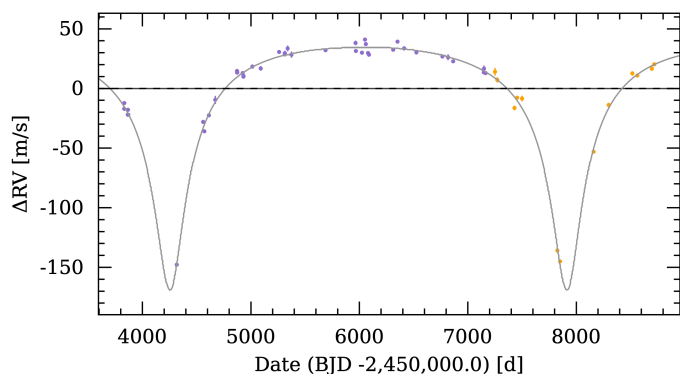


Fig. 14: GJ 9482 HARPS 54 RV measurements and best fitting orbit model. The 41 RV measurements done before the change are in purple and the 13 after the change are in orange.

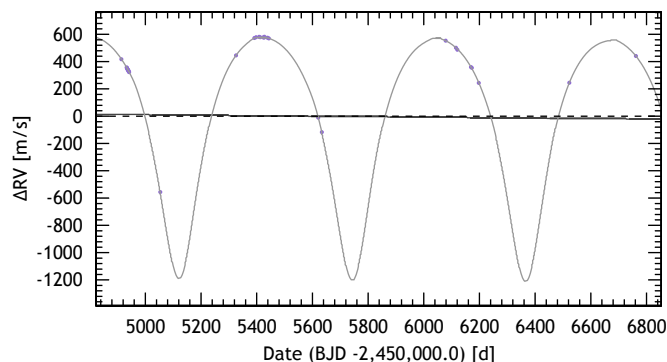


Fig. 15: GJ 9588 HARPS 28 RV measurements done before the change of fibres and best fitting orbit model.

### 6.1.6. GJ 9588

GJ 9588 is an M1 star with a mass of  $0.44 \pm 0.03 M_{\odot}$  and a companion detected through direct imaging, with a spectral type of M9 ( $\pm 2$ ) and an estimated mass between  $0.075$  and  $0.080 M_{\odot}$  (Schneider et al. 2011). We measure the signature of this companion in the RV time series as a linear trend of  $-7.43 \pm 2.94$  m/s/yr, consistent with the reflex motion due to the presence of an object close to the hydrogen-burning limit at a separation of 120 au. However, this is not the dominant signal in RV time series. We detect a clear signal of a new companion with a period of  $618.54 \pm 0.11$  days and a minimum projected mass of  $34 M_J$ . Using *orvara*, we obtain an inclination of 54 degrees and a true mass of  $44 M_J$ . The FWHM of the CCF remains stable over time, indicating that this system is not an SB2. Therefore, GJ 9588 is a very interesting M-dwarf system with two companions, one in the brown dwarf mass range and the second at the boundary between a star and a brown dwarf, both being at very different orbital periods. As illustrated, for example, by Fig. 10 in Artigau et al. (2021), a brown dwarf companion to an M dwarf with an orbital period of  $\sim 2$  yr is a rare object. This system is of interest from the perspective of formation models.

### 6.1.7. Stars with RV drift

Table B.2 lists the stars for which we detect RV drift (linear or quadratic). The sources of these drifts can be companions and/or long-term activity signal (magnetic cycle), making these stars good candidates for future monitoring. Focusing on the 14

stars with the highest amplitude of RV variation (50 m/s peak-to-peak), the majority of them are well-known binaries (e.g. GJ 234 or GJ 660), but some do not have a known companion at the moment and need to be investigated in the future.

## 6.2. Planetary candidates

Beyond the stellar or brown dwarf companion signatures presented and discussed, we point out 16 previously unidentified periodic or quasi-periodic signals in this section. This is only a preliminary analysis as the scope of this article is to make a homogeneous analysis of a large sample. For several of these sources we identify planetary candidates for which additional measurements would be crucial to strengthen the significance of the signal. It is worth noting that several of the stars listed below are part of the NIRPS GTO programme (Bouchy et al. 2017), which should allow conclusions to be drawn about the status of some of these planetary candidates in the near future. For other stars, a detailed analysis of the activity signal via Gaussian process regression or any other method would be important, but is outside the scope of our analysis.

### 6.2.1. GJ 300

This is a very low-mass star ( $M_* = 0.27 \pm 0.09 M_{\odot}$ ) of M5V spectral type, observed on 39 nights between December 2003 and April 2010 with HARPS. This target was poorly monitored during the first and last seasons, with only four measurements before 2008 and five measurements after 2009 (see Fig. A.1). Therefore, we focus on the 30 measurements taken between October 2008 and April 2009 (see Fig. A.2). This RV time series exhibits a high dispersion (rms of 5.07 m/s), and its periodogram shows a significant maximum peak at 8.33 days with a FAP level about 0.1% (see Fig. ?? and Fig. ??). Using the DACE platform, we fit a Keplerian signal at  $8.347 \pm 0.005$  days, with a high eccentricity ( $0.64 \pm 0.07$ ) and a semi-amplitude of  $7.1 \pm 0.8$  m/s, corresponding to a planet of approximately  $7.3 M_{\oplus}$  (presented in Fig. ??). The dispersion of the residuals is about 2.14 m/s and the reduced  $\chi^2$  is below 3. When we subtract this  $\sim 8.33$ -day signal from the complete RV time series of 39 nights, the periodogram of the residuals shows a maximum peak at 299 days. This long-term signal is consistent with the dominant quadratic pattern found in Sect. 4. According to the mean activity level  $\log R'_{HK}$  (-5.3066), the derived rotation period is about 67 days, which does not match with the 8.33-day RV signal. Furthermore, the emission in the three activity indicators (used in Sect. 5.2.2) is not consistent with a saturated regime of the chromosphere, typical of a fast rotator with a rotation period of less than ten days (Delfosse et al. 1999; Reiners et al. 2009; Astudillo-Defru et al. 2017a). This  $\sim 8$ -day signal is therefore a good indication of the presence of a low-mass planet orbiting GJ 300. However, we note that the high eccentricity required to fit this signal is not consistent with the orbital period of less than ten days; such a planet should be on a circularised orbit due to tidal effects. This may indicate that the small number of measurements does not yet allow convergence to the correct orbital solution. If we impose a circular orbit, the fit is of much lower quality (dispersion of the residuals of 3.37 m/s). An alternative solution is to consider two planets in 2:1 resonance on circular orbits, which results in a very good fit (dispersion of the residuals of 2.43 m/s). In any case, this source deserves further observations to lower the FAP of the signal and to study the long-term signal.

### 6.2.2. GJ 317

GJ 317 is an M4V-type star with a mass of  $0.42 \pm 0.02 M_{\odot}$ , known to host two confirmed planets in orbit. GJ 317 b is a planet with a mass of  $1.853 \pm 0.037 M_J$  and an orbital period of  $695.36 \pm 0.70$  days (Rosenthal et al. 2021), discovered using the RV method (Johnson et al. 2007). GJ 317 c is a less constrained object with a mass of  $1.673^{+0.078}_{-0.076} M_J$  and an orbital period of  $7500^{+1500}_{-720}$  days (Rosenthal et al. 2021). GJ 317 was observed on 99 nights from January 2010 to June 2018 with HARPS, and is therefore affected by the fibre change. We find a signal similar to that of GJ 317 b as a large sinusoidal function (see Table 3) and that of GJ 317 c as a linear trend. However, during the periodic analysis, we also find two signals at 314.40 and 236.46 days. These signals stem from an RV time series corrected with an erroneous offset value due to the difficulty of identifying the two signals during our long-term analysis, as in the case of GJ 9482. Using the DACE platform, we adopt the period of Rosenthal et al. (2021) for GJ 317 c as a prior to fit the two Keplerian signals (as presented in Fig. A.3). Two peaks in the periodogram of the residuals reach the 10% FAP level at periods of 50.9 and 59.4 days. These periods are of the same order of magnitude as the estimated rotation period (63 days with the  $\log R'_{HK}$ ), and are close to the significant peak we find in the periodogram of the  $S_{NaD}$  index at 64 days. Consequently, these signals are not considered new candidates, but signatures of the rotation.

### 6.2.3. GJ 361

GJ 361 is an M2V-type star with a mass of  $0.484 \pm 0.022 M_{\odot}$ , observed on 103 nights with HARPS from December 2007 to March 2013 (1919 days of coverage). The periodogram of the RV time series shows two significant peaks with a FAP level well below 0.1% at 28.91 and 26.82 days of period. The last one is a 365-day alias of the first. Using the DACE platform, we fit a signal with a period of 28.95 days and the periodogram of the residuals exhibits a significant peak at 24.98 days. The 33-day rotation period derived from the mean activity level is very close to the signal in the RV periodogram. Furthermore, we find a significant peak in the  $S_{Ca}$  index periodogram at 23.96 days (close to the alias), and another one at 29.79 days in the  $S_{NaD}$  index periodogram. Therefore the two significant periodicities in the HARPS data are similar to that of the stellar rotation, and we do not propose any planetary candidate at these periods.

### 6.2.4. GJ 393

GJ 393 is an M2V-type star with a mass of  $0.43 \pm 0.11 M_{\odot}$ , observed for a total of 169 nights with HARPS from December 2003 to April 2016. At the first step of the iterative search for periodic signals in the RV periodograms, we find a signal with a period of 7.02 days. This particular signal is identified as a planetary signature by Amado et al. (2021), using velocities from HARPS, CARMENES, and HIRES, and photometric data. In this study they subtract a model based on a Gaussian process with a 34-day period signal, attributed to rotational signature, and a longer-term signal, also attributed to activity effect. Numerous significant peaks (with FAP level around or well below 0.1%) are present in the periodogram of the residuals (see Fig. A.4) around 35, 51, 450, 550, 780, and 1000 days. In addition, we find significant peaks in the periodograms of two activity indices ( $S_{Ca}$  and  $S_{H\alpha}$ ) at a period of  $\sim 340$  days, indicating that activity may be responsible for the longer-period RV signals. Consequently, we consider it highly likely that the remain-

ing signals, after subtracting the 7.02-day planetary signature, are not due to planets, but rather to the impact of complex stellar activity.

### 6.2.5. GJ 569A

GJ 569A is a young M2-type star with a mass of  $0.49 \pm 0.04 M_{\odot}$ , and an estimated age of 100 to 125 Myr (Simon et al. 2006). It is sparsely monitored with HARPS, with only 25 measurements taken between 2003 and 2013. The periodogram exhibits a maximum significant peak at a period of 14.38 days (see Fig. ??) with a FAP level of 0.1%. Given its young age this star is highly active, and we estimate a 13-day rotation period from the average  $\log R'_{HK}$  level. Additionally, we find signals at 11.5, 15.8, and 23.1 days in the periodograms of the three activity indices. Due to the poor sampling of the time series and the high level of activity, we are unable to confirm the presence of a planetary candidate signature. The primary signal observed in the RV data is most likely attributable to the stellar activity.

### 6.2.6. GJ 588

GJ 588 is an M2V-type star with a mass of  $0.42 \pm 0.20 M_{\odot}$ , observed for 64 nights with HARPS<sup>9</sup> from 2003 to 2019, and is therefore affected by the change of fibres. Using the DACE platform, we observe a significant dispersion in RVs around the fibre change date, with some measurements taken shortly after the change. To ensure the homogeneity of the dataset, we exclude these specific points. Subsequently, the study of the remaining dataset exhibits a significant peak at a period of 48 days, close to the rotation period of 51.2 days derived from the average level of activity. Furthermore, we find several significant peaks in the analysis of the chromospheric series, at distinct periods (11, 27, 63, and 73 days), indicating a complex manifestation of activity in this star. The presence of multiple significant peaks in the chromospheric series further supports the notion of a dynamically active star, exhibiting a rich variety of activity phenomena. Although the RV data exhibited a significant peak at 48 days, the proximity of this period to the derived rotation period reinforces the idea that this signal is associated with the stellar activity rather than a planetary signal.

### 6.2.7. GJ 654

GJ 654 is an M2V star ( $M_{*} = 0.48 \pm 0.04 M_{\odot}$ ) observed for 186 nights with HARPS from April 2008 to September 2016, which is therefore affected by the change of fibres. Using the DACE platform, the fit of the 260.8-day signal found in the Keplerian analysis does not converge to any satisfactory solution. Consequently, we only focus on four well-sampled observing seasons (165 data points) between April 2013 to September 2016. After subtracting a linear drift, the periodogram of the RV times series exhibits a large peak at 50.50 days and a clear secondary at 15.35 days. In the  $S_{Ca}$  periodogram, we found two significant peaks at 48.2 and 51.4 days, and a significant peak at 50.4 days in

<sup>9</sup> GJ 588 and GJ 887 have also been intensively monitored in recent years as part of observational programmes focused on asteroseismology. Although the hundreds of data points from these programmes are now publicly available and would undoubtedly offer valuable insights into the stars' characteristics, we have not incorporated them into our RV database to keep the RV database consistent, as a dataset of several hundred measurements would compromise the homogeneity of both this study and the next, given their specific goals.

the  $S_{NaD}$  periodogram. Therefore, we consider the first signal at 50.5 days to be attributed to the star's rotational signature, while the remaining signal at 15.35 days is a strong planetary candidate. The fitted Keplerian function corresponds to a  $5.11 \pm 0.4 M_{\oplus}$  planetary mass. The complete characterisation of the system goes beyond the scope of this paper and will be addressed in a future paper.

### 6.2.8. GJ 699

At just 1.8 pc from our Sun, Barnard's Star (GJ 699) is the second-closest system after Proxima Centauri -  $\alpha$  Centauri (Bailer-Jones et al. 2018; Gaia Collaboration et al. 2021b). Ribas et al. (2018) proposes the presence of a candidate super-Earth planet on a 233-day orbit. The star has a long rotation period of approximately  $145 \pm 15$  days, determined by variations in chromospheric activity indicators by Toledo-Adrón et al. (2019), and  $137 \pm 5$  days derived from the longitudinal magnetic field variation by Fouqué et al. (2023). However, Lubin et al. (2021) does not confirm this planet and proposes it to be an alias of the rotation period. This conclusion is further supported by infrared RV measurements with SPIRou (Artigau et al. 2022), which strongly disfavour the existence of a 233-day planet. The periodogram of our RV time series exhibits a significant peak at 273 days (i.e. twice the rotation period). It is therefore likely that this signal is due to stellar activity.

### 6.2.9. GJ 739

GJ 739 is an M3V-type star with an estimated mass of  $0.46 \pm 0.02 M_{\odot}$ , poorly monitored with HARPS with only 19 measurements taken from July 2008 to May 2012. In our analysis we find a significant peak with a very low FAP level (well below 0.1%) in the RV periodogram at 137.8 days. By fitting a Keplerian function on the DACE platform, we obtain a signal at  $145.3 \pm 0.8$  days, corresponding to a planet with a mass of  $39 \pm 4 M_{\oplus}$ . The rotation period derived from the level of activity is around 50 days, and we find a significant peak in the  $S_{Ca}$  periodogram at 40.82 days and another significant peak at 47.9 days in the  $S_{H\alpha}$  periodogram. These findings suggest that the signal adjusted to about 138 days is unlikely to be a rotational signature. However, to confirm this strong planet candidate, we require more than the current 19 measurements.

### 6.2.10. GJ 754

GJ 754 is an M4.5V-type star (Reid et al. 1995) with a mass of  $0.18 \pm 0.02 M_{\odot}$ , observed for a total of 170 nights between May 2004 and September 2016 with HARPS, which means it is affected by the change of fibres. Upon analysing the entire dataset, we find two significant peaks in the RV periodogram at 249 and 17 days (in order of their power), with no long-term signal detected. However, focusing on the well-monitored seasons (from 2012 to 2016), we find a significant peak at 77 days using the DACE platform (see Fig. A.9). Using the activity proxies, we find seven significant peaks at different periods in the three chromospheric indexes (ranging from 12 to 1750 days), and the rotation period derived from the mean activity level is about 77 days. In conclusion, this quiet mid-M dwarf exhibits a complex and evolving activity signal, which poses challenges in disentangling any potential planetary system from the RV time series. A more in-depth analysis is required to determine if there is indeed a planetary system, which is beyond the scope of this article.

### 6.2.11. GJ 846

GJ 846 is an M1V-type star with a mass of  $0.61 \pm 0.08 M_{\odot}$ , observed for a total of 51 nights from May 2004 to November 2010 with HARPS. The RV periodogram exhibits a significant peak at 10.8 days with a FAP of around 0.1%. However, using the DACE platform for Keplerian fitting, the results are inconclusive, showing a high dispersion in the residuals and a high value of reduced  $\chi^2$ . The rotation period derived from the average activity level is about 20 days, and we find significant peaks at 7.8, 10.7, 19.2, and 30.9 days in the periodograms of the three activity indices. Previous studies identified rotation periods ranging from 26 to 31 days when determined by activity index variations (Suárez Mascareño et al. 2015, 2017b; Díez Alonso et al. 2019a), and from 10.7 to 11.01 days when determined from the magnetic field modulation (Hébrard et al. 2016; Fouqué et al. 2023), highlighting the complexity of the activity signal. In conclusion, the RV signal is consistent with one of the activity signals, leading us to consider that the RV time series is dominated by the short-term impact of activity.

### 6.2.12. GJ 880

GJ 880 is an M2V-type star with a mass of  $0.58 \pm 0.08 M_{\odot}$ , and was well monitored with HARPS over 137 nights from December 2003 to October 2016. We find a significant peak at 40.05 days in the RV periodogram, with a FAP below 0.1%, and another less significant peak at 37.2 days. These signals are aliases of each other due to the one-year sampling. In addition, we find a signal at 37.4 days in the  $S_{NaD}$  periodogram, another at 37.0 days in the  $S_{H\alpha}$  periodogram, and a third at 35.3 days in the  $S_{Ca}$  periodogram. Suárez Mascareño et al. (2015) and Fouqué et al. (2023) both find a similar rotation period of  $\sim 37$  days using two complementary methods. In conclusion, the signal at 37.2 days corresponds to the rotational signature, while the signal at 40.5 days is an alias of it.

## 7. Limits and discussion

The systematic analysis of 200 highly heterogeneous RV time series imposes the use of conservative methods, which entails certain limitations. Here we discuss these choices and their consequences in terms of detection.

### 7.1. Sampling

Even if stars observed for fewer than 10 nights are excluded from the study, the sampling frequency remains the main bias in this analysis. Stars that are well sampled over a short timescale allow the detection of short-term periodicity, and the better characterisation and subtraction of activity-induced signals from the rotation period. Conversely, only stars monitored over a long timescale enable the analysis of long-period signals. The histogram of the time interval between the first and last measurement for the 200 stars in our sample is presented in Fig. 16. It is evident that this span varies significantly, resulting in an uneven detectability. This bias is taken into account in the second article of this analysis (Mignon et al. in prep.), where individual detection limits are computed in order to construct the overall occurrence frequency.

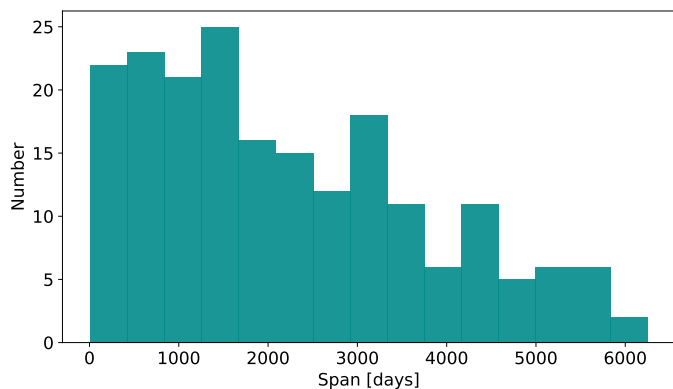


Fig. 16: Distribution of time coverage of the RV time series for the 200 stars in our sample.

## 7.2. Periodograms

For this study we compute the periodogram proposed in Zechmeister & Kürster (2009), previously used in Bonfils et al. (2013b), and adopt the FAP level of the highest peak as a conservative detection criterion for detecting a periodic signal. Although more recent methods enable the better separation of Keplerian signals from correlated noise, which can be due to activity (Delisle et al. 2020; Hara et al. 2022). They generally require a more accurate knowledge of the rotation period, which is not precisely known for all our targets. Additionally, for certain M dwarfs in the sample, the effect of activity may manifest at different periods (Mignon et al. 2023).

## 7.3. Corrections of activity

We correct 23 RV time series from 35 signatures of the stellar rotation using a Keplerian signal with the same phase across the entire dataset. As the presence of activity-induced effects is a direct consequence of magnetic structures (mainly spots) on the surface, which have a finite lifetime, their behaviour is usually quasi-periodic rather than strictly periodic. Our correction is therefore not optimal compared to a case-by-case study, but it is well-suited for our homogeneous and automated search. However, this approach may hinder the detection of some weak Keplerian signals.

## 7.4. Missed planetary systems

In this section we provide an explanation for the non-detection of some previously published planets, aiming to illustrate the limitations of conducting such a homogeneous study on a very large sample. Additionally, this comparison allows us to identify the domains (e.g. mass, period, multiplicity) where our study remains robust. According to the NASA Exoplanet database, we identify 51 planets out of the 78 previously published (65.4%) within our sample of 200 M dwarfs in 2020–2021. In terms of planetary systems, we identify 31 of the 40 previously discovered systems (75%).

### 7.4.1. System detected with additional measurements

We limit our study to the analysis of RVs data from HARPS, to ensure a homogeneous dataset. However, some of the planets we do not detect were originally discovered using datasets combined from other instruments. GJ 191 hosts a two-planet

system discovered by Anglada-Escudé et al. (2014) using RV data from HARPS, HIRES, and PFS combined with photometry (ASAS 3). GJ 357 (Luque et al. 2019) hosts a three-planet system, which was revealed by combining transit and RV methods from TESS, CARMENES, HIRES, UVES, and HARPS. The planetary systems orbiting GJ 422 and GJ 682 were detected by the RV method, but most of the data were obtained using UVES (Tuomi et al. 2014). GJ 740 and GJ 3779 are both single-planet systems detected by RVs, combining HARPS, HARPS-N, and CARMENES data (Toledo-Adrón et al. 2021) and HARPS and CARMENES data (Luque et al. 2018), respectively. By excluding these five systems, which were not detected mainly due to an insufficient number of measurements with HARPS, we recover over 88% of the previously published systems within our sample.

### 7.4.2. Very short-period planets

We perform automatic Keplerian analysis for periods longer than 1.6 days to avoid confusion between aliases created by the one-day sampling and the actual period of the signal. As a result, two planets with periods below this threshold were not detected: GJ 1214 b, which has a period of 1.58 days and was detected through the transit method (Carter et al. 2011), and GJ 3543 b, which has a period of 1.12 days and was detected by the RV method (Astudillo-Defru et al. 2015). By lowering the threshold to 1.1 days, we do detect these two planets in the periodograms. This confirms that they are only missed due to the choice of the tested period domain, and thus lie outside the scope of this study. It is therefore possible that we might have missed unknown planets in our sample with orbital periods shorter than 1.6 days. If we consider only systems with periods superior to 1.6 days, we recover 94% of the previously published systems.

### 7.4.3. The specific case of GJ 1061

The case of GJ 1061 is complex. This system includes three planet candidates detected from the HARPS data (Dreizler et al. 2020), with minimum masses ranging from 1.4 to 1.8 Earth masses and RV signal semi-amplitudes between  $K = 1.8$  and  $K = 2.5$  m/s. The RVs we obtain show an offset of about a dozen m/s over one observing season, without a clear explanation at this stage. These data come from three different programmes, and the mask used in the CCF method is not the same for the various observer teams. However, even if our template matching code uses this first CCF RV for its original iteration, its final result is independent of it. Several other sources were initially analysed with different CCF masks, but they did not generate this type of offset. This remains the only case where we do not detect the published signal without identifying the reason behind it.

## 8. Conclusion

This comprehensive analysis of RVs measured with HARPS on M dwarfs between 2003 and 2019 (200 stars with over ten measurements) significantly updates the set of detected periodic RV signals. The investigation of long-term trends (linear, quadratic, or sinusoidal) reveals variability in 57 time series (28.5% of our sample): 16 linear trends, 29 quadratic trends, and 12 sinusoidal functions. Regarding the objects in the last category, we confirm seven detections of massive companions (very low-mass stars or brown dwarfs), identify four new companions of M

dwarfs (ultra-cool dwarfs or brown dwarfs for GJ 3307, GJ 4001, GJ 4254, and GJ 9588), and significantly revise the parameters of a massive planet detected in 2011 (GJ 9482 b), providing better constraints on its orbit with a period of  $3659 \pm 4$  days and a mass of  $4.5 M_J$ . After subtracting the long-term variability, the analysis of the remaining 108 periodic signals leads to the recovery of 52 previously published planets and 34 known rotation period signatures. The analysis of other previously unidentified periodic signals allows us to propose three planetary candidates in orbit around GJ 300 ( $7.3 M_{\oplus}$ ), GJ654 ( $5 M_{\oplus}$ ), and GJ739 ( $39 M_{\oplus}$ ), which will require additional measurements for confirmation. For six other stars (GJ 361, GJ 393, GJ 569, GJ 754, GJ 846, and GJ 880), we suggest that the RV variation is more likely due to stellar activity. This work serves as the foundation for a statistical study of the M dwarf population in the solar neighbourhood, from detection limits to occurrence statistics, which is the aim of the second article in this series.

*Acknowledgements.* This research has made use of the VizieR catalogue access tool, CDS, Strasbourg, France. The original description of the VizieR service was published in A&AS 143, 23 This work has been supported by a grant from LabEx OSUG@2020 (Investissements d'avenir - ANR10LABX56) This research has made use of the NASA Exoplanet Archive, which is operated by the California Institute of Technology, under contract with the National Aeronautics and Space Administration under the Exoplanet Exploration Program. This research has made use of the Exoplanet Follow-up Observation Program (ExoFOP; DOI: 10.26134/ExoFOP5) website, which is operated by the California Institute of Technology, under contract with the National Aeronautics and Space Administration under the Exoplanet Exploration Program. This work has been carried out within the framework of the NCCR PlanetS supported by the Swiss National Science Foundation. NCS acknowledges funding by the European Union (ERC, FIERCE, 101052347). Views and opinions expressed are however those of the author(s) only and do not necessarily reflect those of the European Union or the European Research Council. Neither the European Union nor the granting authority can be held responsible for them. This work was supported by FCT - Fundação para a Ciência e a Tecnologia through national funds and by FEDER through COMPETE2020 - Programa Operacional Competitividade e Internacionalização by these grants: UIDB/04434/2020; UIDP/04434/2020.

## References

- Aigrain, S. & Foreman-Mackey, D. 2022, arXiv e-prints, arXiv:2209.08940
- Almenara, J. M., Astudillo-Defru, N., Bonfils, X., et al. 2015, *A & A*, 581, L7
- Amado, P. J., Bauer, F. F., Rodríguez López, C., et al. 2021, *A & A*, 650, A188
- Anglada-Escudé, G., Amado, P. J., Barnes, J., et al. 2016, *Nature*, 536, 437
- Anglada-Escudé, G., Arriagada, P., Tuomi, M., et al. 2014, *Monthly Notices of the Royal Astronomical Society: Letters*, 443, L89
- Anglada-Escudé, G., Tuomi, M., Gerlach, E., et al. 2013, *A&A*, 556, A126
- Artigau, É., Cadieux, C., Cook, N. J., et al. 2022, *AJ*, 164, 84
- Artigau, É., Hébrard, G., Cadieux, C., et al. 2021, *AJ*, 162, 144
- Astudillo-Defru, N., Bonfils, X., Delfosse, X., et al. 2015, *A & A*, 575, A119
- Astudillo-Defru, N., Cloutier, R., Wang, S. X., et al. 2020, *A&A*, 636, A58
- Astudillo-Defru, N., Delfosse, X., Bonfils, X., et al. 2017a, *A & A*, 600, A13
- Astudillo-Defru, N., Diaz, R. F., Bonfils, X., et al. 2017b, *A & A*, 605, L11
- Astudillo-Defru, N., Forveille, T., Bonfils, X., et al. 2017c, *A & A*, 602, A88
- Bailer-Jones, C. A. L., Rybizki, J., Fouesneau, M., Mantelet, G., & Andrae, R. 2018, *AJ*, 156, 58
- Bailey, J., Butler, R. P., Tinney, C. G., et al. 2008, *The Astrophysical Journal*, 690, 743
- Baluev, R. V. 2008, *MNRAS*, 385, 1279
- Beichman, C., Benneke, B., Knutson, H., et al. 2014, *PASP*, 126, 1134
- Berta-Thompson, Z. K., Irwin, J., Charbonneau, D., et al. 2015, *Nature*, 527, 204
- Bidelman, W. P. 1985, *ApJS*, 59, 197
- Biller, B. A., Grandjean, A., Messina, S., et al. 2022, *A&A*, 658, A145
- Bonfils, X., Almenara, J.-M., Cloutier, R., et al. 2018a, *A & A*, 618, A142
- Bonfils, X., Astudillo-Defru, N., Díaz, R., et al. 2018b, *A & A*, 613, A25
- Bonfils, X., Curto, G. L., Correia, A., et al. 2013a, *A & A*, 556, A110
- Bonfils, X., Delfosse, X., Udry, S., et al. 2011, *The M-dwarf sample*, 1111
- Bonfils, X., Delfosse, X., Udry, S., et al. 2013b, *A & A*, 549, A109
- Bonfils, X., Forveille, T., Delfosse, X., et al. 2005, *A & A*, 443, L15
- Bonfils, X., Mayor, M., Delfosse, X., et al. 2007, *A & A*, 474, 293
- Bouchy, F., Doyon, R., Artigau, É., et al. 2017, *The Messenger*, 169, 21
- Bouchy, F., Pepe, F., & Queloz, D. 2001, *A & A*, 374, 733
- Brandt, T. D. 2021, *ApJS*, 254, 42
- Brandt, T. D., Dupuy, T. J., Li, Y., et al. 2021, *AJ*, 162, 186
- Burn, R., Schlecker, M., Mordasini, C., et al. 2021, *A&A*, 656, A72
- Butler, R. P., Johnson, J. A., Marcy, G. W., et al. 2006, *Publications of the Astronomical Society of the Pacific*, 118, 1685
- Byrd, R. H., Lu, P., Nokedal, J., & Zhu, C. 1995, *SIAM Journal on scientific computing*, 16, 1190
- Carter, J. A., Winn, J. N., Holman, M. J., et al. 2011, *The Astrophysical Journal*, 730, 82
- Chabrier, G. 2001, *ApJ*, 554, 1274
- Charbonneau, D., Berta, Z. K., Irwin, J., et al. 2009, *Nature*, 462, 891
- Coffinet, A., Lovis, C., Dumusque, X., & Pepe, F. 2019, *A&A*, 629, A27
- Collaboration, G. et al. 2018, *VizieR Online Data Catalog*, 1345
- Costa, E., Méndez, R. A., Jao, W.-C., et al. 2005, *The Astronomical Journal*, 130, 337
- Cumming, A., Butler, R. P., Marcy, G. W., et al. 2008, *Publications of the Astronomical Society of the Pacific*, 120, 531
- Cumming, A., Marcy, G. W., & Butler, R. P. 1999, *ApJ*, 526, 890
- Cutri, R. M., Skrutskie, M. F., van Dyk, S., et al. 2003, *VizieR Online Data Catalog*, II/246
- Delfosse, X., Bonfils, X., Forveille, T., et al. 2013, *A&A*, 553, A8
- Delfosse, X., Forveille, T., Beuzit, J. L., et al. 1999, *A&A*, 344, 897
- Delfosse, X., Forveille, T., Mayor, M., et al. 1998a, *A&A*, 338, L67
- Delfosse, X., Forveille, T., Perrier, C., & Mayor, M. 1998b, *A&A*, 331, 581
- Delfosse, X., Forveille, T., Ségransan, D., et al. 2000, *A&A*, 364, 217
- Delisle, J. B., Hara, N., & Ségransan, D. 2020, *A&A*, 635, A83
- Delisle, J. B., Ségransan, D., Buchschacher, N., & Alesina, F. 2016, *A&A*, 590, A134
- Diaz, R. F., Delfosse, X., Hobson, M. J., et al. 2019, *A&A*, 625, A17
- Diez Alonso, E., Caballero, J. A., Montes, D., et al. 2019a, *A&A*, 621, A126
- Diez Alonso, E., Caballero, J. A., Montes, D., et al. 2019b, *A & A*, 621, A126
- Dittmann, J. A., Irwin, J. M., Charbonneau, D., et al. 2017, *Nature*, 544, 333
- Doyon, R., Lafrenière, D., Albert, L., et al. 2014, in *Search for Life Beyond the Solar System. Exoplanets, Biosignatures & Instruments*, ed. D. Apai & P. Gabor, 3.6
- Dreizler, S., Jeffers, S. V., Rodríguez, E., et al. 2020, *MNRAS*, 493, 536
- Dressing, C. D. & Charbonneau, D. 2013, *ApJ*, 767, 95
- Dressing, C. D. & Charbonneau, D. 2015, *ApJ*, 807, 45
- Ducati, J. 2002, *VizieR Online Data Catalog*, 2237
- Feng, F., Butler, R. P., Shectman, S. A., et al. 2020, *The Astrophysical Journal Supplement Series*, 246, 11
- Finch, C. T., Zacharias, N., & Jao, W.-C. 2018, *The Astronomical Journal*, 155, 176
- Forveille, T., Bonfils, X., Curto, G. L., et al. 2011, *A & A*, 526, A141
- Forveille, T., Bonfils, X., Delfosse, X., et al. 2009, *A & A*, 493, 645
- Fouqué, P., Martioli, E., Donati, J. F., et al. 2023, arXiv e-prints, arXiv:2302.03377
- Fouqué, P., Moutou, C., Malo, L., et al. 2018, *MNRAS*, 475, 1960
- Gaia Collaboration. 2020, *VizieR Online Data Catalog*, I/350
- Gaia Collaboration, Brown, A. G. A., Vallenari, A., et al. 2021a, *A&A*, 650, C3
- Gaia Collaboration, Smart, R. L., Sarro, L. M., et al. 2021b, *A&A*, 649, A6
- Gaidos, E., Mann, A., Lépine, S., et al. 2014, *Monthly Notices of the Royal Astronomical Society*, 443, 2561
- Gillon, M., Meadows, V., Agol, E., et al. 2020, in *Bulletin of the American Astronomical Society*, Vol. 52, 0208
- Gliese, W. & Jahreiß, H. 1991, *Preliminary Version of the Third Catalogue of Nearby Stars, On: The Astronomical Data Center CD-ROM: Selected Astronomical Catalogs*
- Hara, N. C., Unger, N., Delisle, J.-B., Díaz, R. F., & Ségransan, D. 2022, *A&A*, 663, A14
- Hawley, S. L. & Pettersen, B. R. 1991, *ApJ*, 378, 725
- Haywood, R. D., Collier Cameron, A., Queloz, D., et al. 2014, *MNRAS*, 443, 2517
- Hébrard, É., Donati, J.-F., Delfosse, X., et al. 2016, *Monthly Notices of the Royal Astronomical Society*, 461, 1465
- Henry, T. J., Jao, W.-C., Winters, J. G., et al. 2018, *AJ*, 155, 265
- Henry, T. J., Kirkpatrick, J. D., & Simons, D. A. 1994, *The Astronomical Journal*, 108, 1437
- Hojjatpanah, S., Figueira, P., Santos, N. C., et al. 2019, *A&A*, 629, A80
- Howard, A. W., Johnson, J. A., Marcy, G. W., et al. 2010, *The Astrophysical Journal*, 721, 1467
- Johnson, J. A., Butler, R. P., Marcy, G. W., et al. 2007, *The Astrophysical Journal*, 670, 833
- Kaminski, A., Trifonov, T., Caballero, J., et al. 2018, *A & A*, 618, A115
- Kervella, P., Arenou, F., Mignard, F., & Thévenin, F. 2019, *A&A*, 623, A72
- Kiraga, M. & Stepien, K. 2007, arXiv preprint arXiv:0707.2577
- Koen, C., Kilikenny, D., Van Wyk, F., & Marang, F. 2010, *Monthly Notices of the Royal Astronomical Society*, 403, 1949
- Kopparapu, R. K., Ramirez, R., Kasting, J. F., et al. 2013, *ApJ*, 765, 131
- Kuerster, M., Endl, M., Rouesnel, F., et al. 2003, *A & A*, 403, 1077
- Landolt, A. U. 1992, *The Astronomical Journal*, 104, 340

- Lépine, S. & Shara, M. M. 2005, *AJ*, 129, 1483
- Lillo-Box, J., Figueira, P., Leleu, A., et al. 2020a, *A&A*, 642, A121
- Lillo-Box, J., Lopez, T. A., Santerne, A., et al. 2020b, *A&A*, 640, A48
- Lo Curto, G., Mayor, M., Benz, W., et al. 2013, *A&A*, 551, A59
- Lo Curto, G., Pepe, F., Avila, G., et al. 2015, *The Messenger*, 162, 9
- Lomb, N. R. 1976, *Astrophysics and space science*, 39, 447
- Lovis, C., Mayor, M., Pepe, F., Queloz, D., & Udry, S. 2008, in *Astronomical Society of the Pacific Conference Series*, Vol. 398, *Extreme Solar Systems*, ed. D. Fischer, F. A. Rasio, S. E. Thorsett, & A. Wolszczan, 455
- Lovis, C. & Pepe, F. 2007, *A&A*, 468, 1115
- Lubin, J., Robertson, P., Stefansson, G., et al. 2021, *AJ*, 162, 61
- Luque, R., Nowak, G., Pallé, E., et al. 2018, *A&A*, 620, A171
- Luque, R., Pallé, E., Kossakowski, D., et al. 2019, *A & A*, 628, A39
- Lurie, J. C., Henry, T. J., Jao, W.-C., et al. 2014, *The Astronomical Journal*, 148, 91
- Marconi, A., Abreu, M., Adibekyan, V., et al. 2020, in *Society of Photo-Optical Instrumentation Engineers (SPIE) Conference Series*, Vol. 11447, *Society of Photo-Optical Instrumentation Engineers (SPIE) Conference Series*, 1144726
- Marcy, G. W., Butler, R. P., Fischer, D., et al. 2001, *The Astrophysical Journal*, 556, 296
- Mayor, M., Pepe, F., Queloz, D., et al. 2003, *The Messenger*, 114, 20
- Ment, K., Dittmann, J. A., Astudillo-Defru, N., et al. 2019, *The Astronomical Journal*, 157, 32
- Mignon, L., Meunier, N., Delfosse, X., et al. 2023, *A&A*, 675, A168
- Morin, J., Donati, J.-F., Petit, P., et al. 2008, *Monthly Notices of the Royal Astronomical Society*, 390, 567
- Moutou, C., Mayor, M., Curto, G. L., et al. 2011, *A & A*, 527, A63
- Newton, E. R., Irwin, J., Charbonneau, D., Berta-Thompson, Z. K., & Dittmann, J. A. 2016, *ApJ*, 821, L19
- Pepe, F., Mayor, M., Galland, F., et al. 2002, *A&A*, 388, 632
- Pinamonti, M., Sozzetti, A., Maldonado, J., et al. 2022, *A&A*, 664, A65
- Queloz, D., Henry, G. W., Sivan, J. P., et al. 2001, *A&A*, 379, 279
- Rajpaul, V., Aigrain, S., Osborne, M. A., Reece, S., & Roberts, S. 2015, *MNRAS*, 452, 2269
- Reid, I. N., Hawley, S. L., & Gizis, J. E. 1995, *AJ*, 110, 1838
- Reiners, A., Basri, G., & Browning, M. 2009, *ApJ*, 692, 538
- Reylé, C., Jardine, K., Fouqué, P., et al. 2021, *A&A*, 650, A201
- Riaz, B., Gizis, J. E., & Harvin, J. 2006, *AJ*, 132, 866
- Ribas, I., Tuomi, M., Reiners, A., et al. 2018, *Nature*, 563, 365
- Riedel, A. R., Finch, C. T., Henry, T. J., et al. 2014, *AJ*, 147, 85
- Rivera, E. J., Lissauer, J. J., Butler, R. P., et al. 2005, *ApJ*, 634, 625
- Robertson, P. & Mahadevan, S. 2014, *ApJ*, 793, L24
- Robertson, P., Mahadevan, S., Endl, M., & Roy, A. 2014, *Science*, 345, 440
- Rosenthal, L. J., Fulton, B. J., Hirsch, L. A., et al. 2021, *ApJS*, 255, 8
- Sabotta, S., Schlecker, M., Chaturvedi, P., et al. 2021, *A&A*, 653, A114
- Sahlmann, J., Lazorenko, P., Ségransan, D., et al. 2016, *A & A*, 595, A77
- Scargle, J. D. 1982, *The Astrophysical Journal*, 263, 835
- Schneider, A., Melis, C., Song, I., & Zuckerman, B. 2011, *ApJ*, 743, 109
- Ségransan, D., Mayor, M., Udry, S., et al. 2011, *A & A*, 535, A54
- Simon, M., Bender, C., & Prato, L. 2006, *ApJ*, 644, 1183
- Snellen, I., de Kok, R., Birkby, J. L., et al. 2015, *A&A*, 576, A59
- Stauffer, J., Tanner, A. M., Bryden, G., et al. 2010, *Publications of the Astronomical Society of the Pacific*, 122, 885
- Stephenson, C. B. 1986, *AJ*, 92, 139
- Suárez Mascareño, A., González Hernández, J. I., Rebolo, R., et al. 2017a, *A&A*, 597, A108
- Suárez Mascareño, A., Rebolo, R., & González Hernández, J. I. 2016, *A&A*, 595, A12
- Suárez Mascareño, A., Rebolo, R., González Hernández, J. I., & Esposito, M. 2015, *MNRAS*, 452, 2745
- Suárez Mascareño, A., Rebolo, R., González Hernández, J. I., & Esposito, M. 2017b, *MNRAS*, 468, 4772
- Toledo-Padrón, B., González Hernández, J. I., Rodríguez-López, C., et al. 2019, *MNRAS*, 488, 5145
- Toledo-Padrón, B., Suárez Mascareño, A., González Hernández, J. I., et al. 2021, *A&A*, 648, A20
- Torres, G., Andersen, J., & Giménez, A. 2010, *The Astronomy and Astrophysics Review*, 18, 67
- Trifonov, T., Tal-Or, L., Zechmeister, M., et al. 2020, *A&A*, 636, A74
- Tuomi, M., Jones, H. R., Barnes, J. R., Anglada-Escudé, G., & Jenkins, J. S. 2014, *Monthly Notices of the Royal Astronomical Society*, 441, 1545
- Udry, S., Bonfils, X., Delfosse, X., et al. 2007, *A & A*, 469, L43
- van de Kamp, P. 1977, *Vistas in Astronomy*, 21, 289
- Van Eylen, V., Astudillo-Defru, N., Bonfils, X., et al. 2021, *MNRAS*, 507, 2154
- Van Leeuwen, F. 2007, *A & A*, 474, 653
- Weinberger, A. J., Boss, A. P., Keiser, S. A., et al. 2016, *The Astronomical Journal*, 152, 24
- Winters, J. G., Charbonneau, D., Henry, T. J., et al. 2021, *AJ*, 161, 63
- Winters, J. G., Henry, T. J., Jao, W.-C., et al. 2010, *The Astronomical Journal*, 141, 21
- Winters, J. G., Henry, T. J., Lurie, J. C., et al. 2014, *The Astronomical Journal*, 149, 5
- Winters, J. G., Medina, A. A., Irwin, J. M., et al. 2019, *AJ*, 158, 152
- Winters, J. G., Sevrinsky, R. A., Jao, W.-C., et al. 2016, *The Astronomical Journal*, 153, 14
- Wittenmyer, R. A., Tuomi, M., Butler, R., et al. 2014, *The Astrophysical Journal*, 791, 114
- Wright, D., Wittenmyer, R., Tinney, C., Bentley, J., & Zhao, J. 2016, *The Astrophysical Journal Letters*, 817, L20
- Zacharias, N., Finch, C., Girard, T., et al. 2013, *The Astronomical Journal*, 145, 44
- Zechmeister, M. & Kürster, M. 2009, *A & A*, 496, 577
- Zechmeister, M., Kürster, M., & Endl, M. 2009, *A & A*, 505, 859
- Zhu, C., Byrd, R. H., Lu, P., & Nocedal, J. 1997, *ACM Transactions on Mathematical Software (TOMS)*, 23, 550

## Appendix A: Graphs

### Appendix A.1: Planetary candidates

#### Appendix A.1.1: GJ 300

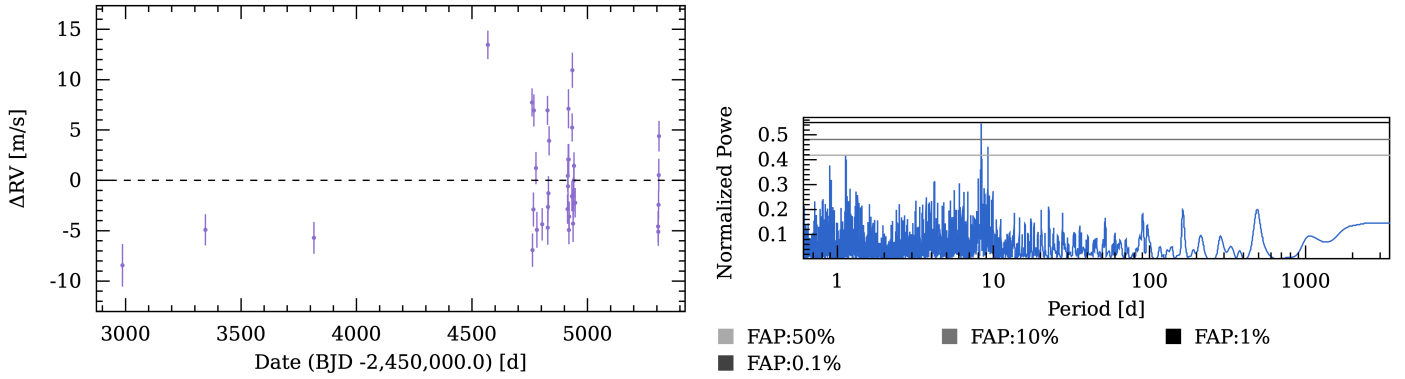


Fig. A.1: RV time series and GLS periodogram of the complete RV times series of GJ 300

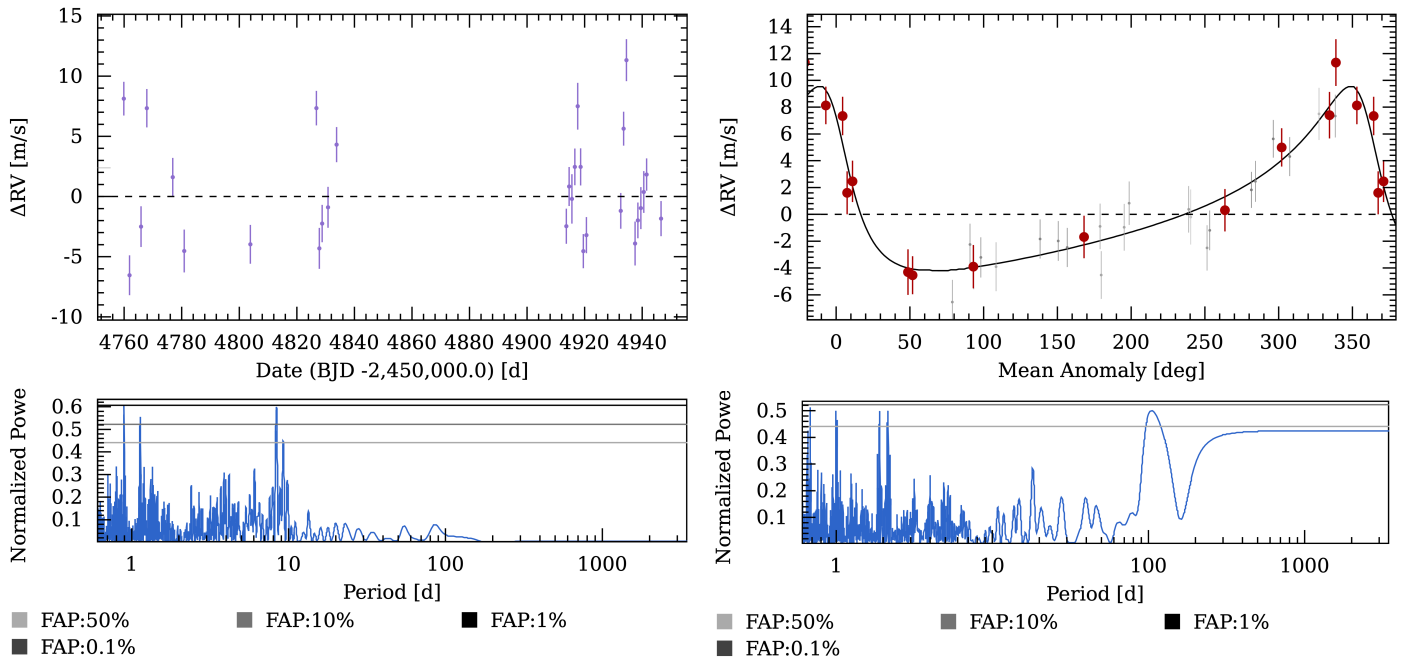


Fig. A.2: RV time series and GLS periodograms of the 28 nights between October 2008 and April 2009 (see text) of GJ 300 (left: original, right: residuals).

## Appendix A.1.2: GJ 317

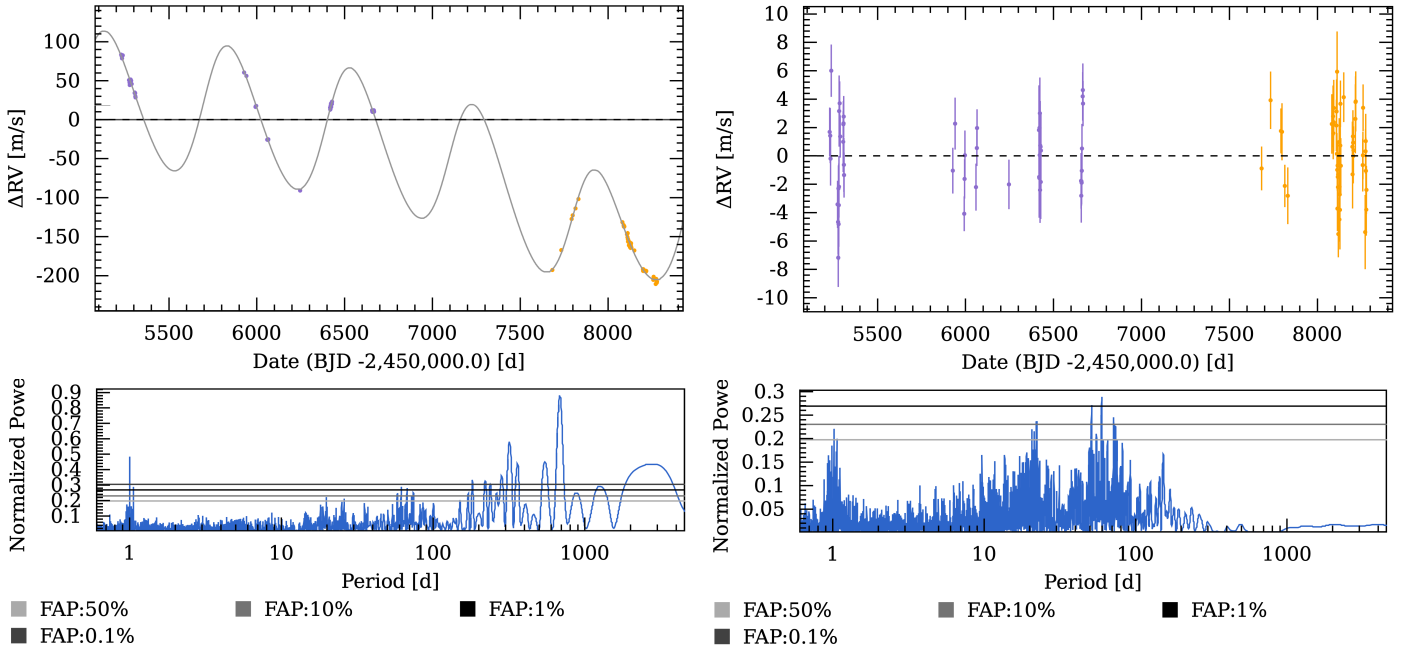


Fig. A.3: RV time series and GLS periodograms of GJ 317 (left: original, right: residuals). The RV obtained before and after the fibre change is respectively plotted in blue and orange.

## Appendix A.1.3: GJ 361

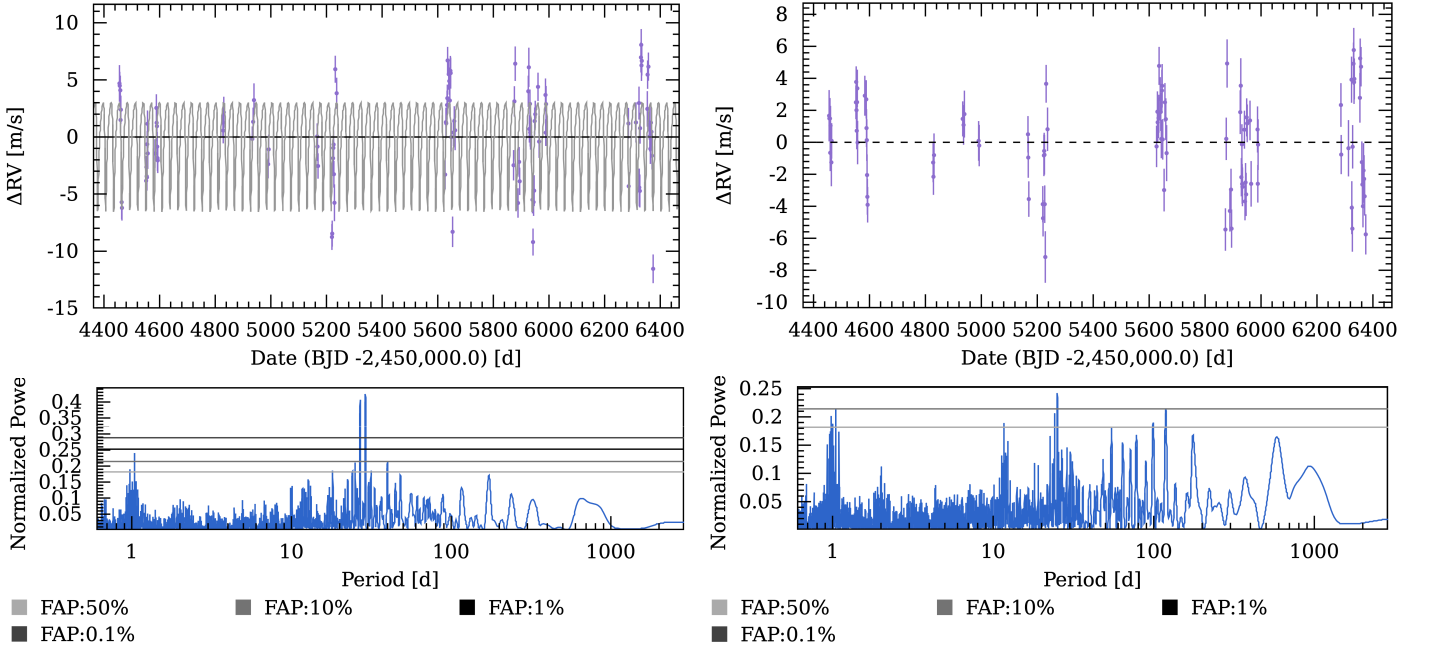


Fig. A.4: RV time series with fitted signal and GLS periodograms of GJ 361 (left: original, right: residuals).

Appendix A.1.4: GJ 393

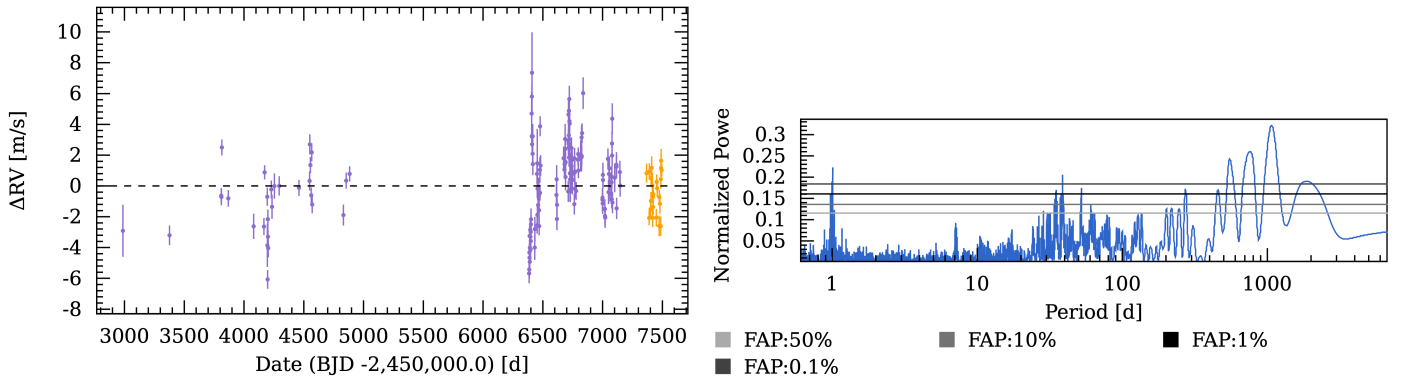


Fig. A.5: RV time series and GLS periodogram of GJ 393 after the subtraction of the planetary signal at 7.02 days.

Appendix A.1.5: GJ 569A

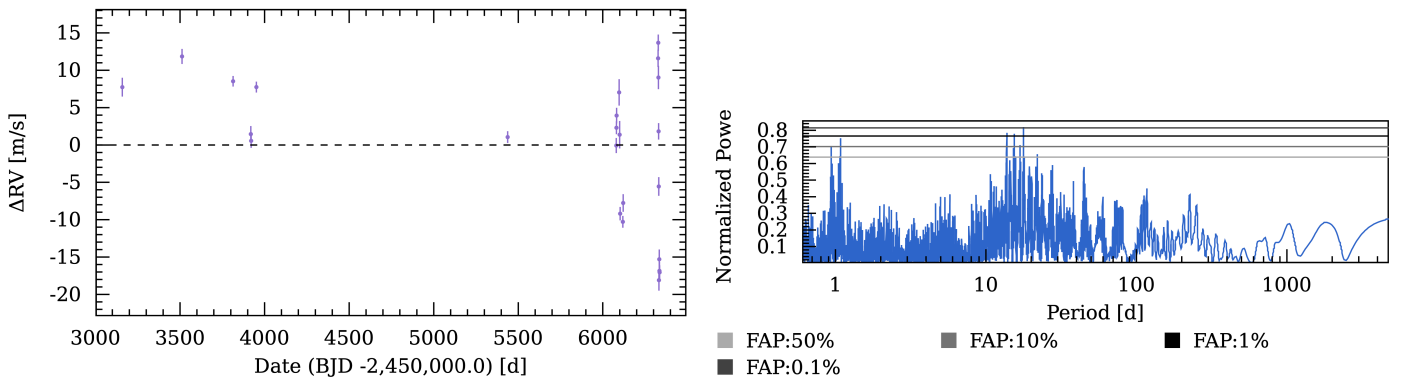


Fig. A.6: RV time series and GLS periodogram of GJ 569A.

## Appendix A.1.6: GJ 654

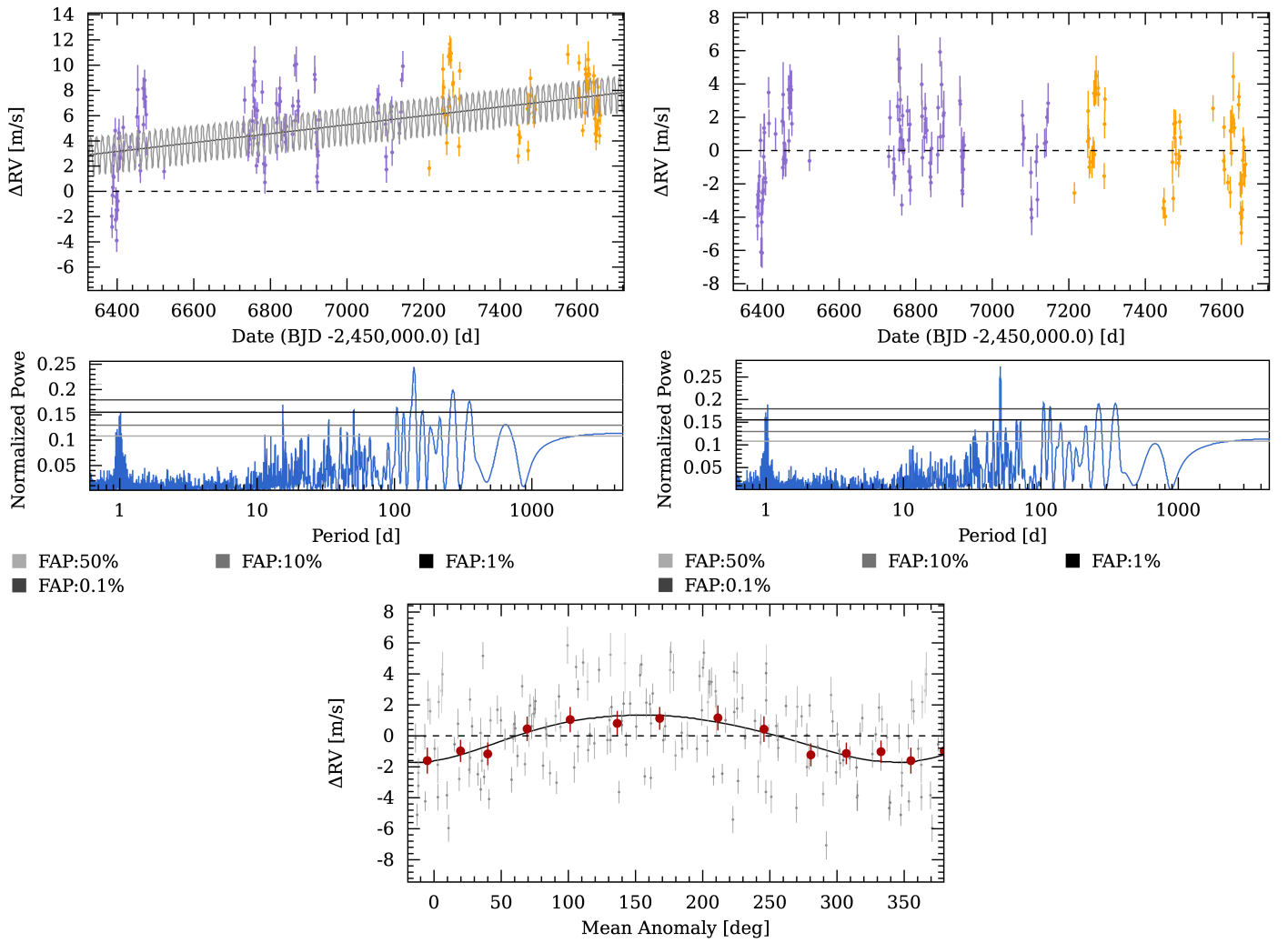


Fig. A.7: RV time series and GLS of GJ 654. Upper left: RV time series zoomed in on the four well-monitored seasons with the trend and Keplerian signals fitted at 15.35 days. Upper right: RV time series of the residuals of the trend and the Keplerian signal, zoomed in on the four well-monitored seasons. Middle left: periodogram. Middle right: periodogram of the residuals of the trend and the Keplerian signal, zoomed in on the four well-monitored seasons. Bottom: signal fitted at 15.35 days.

## Appendix A.1.7: GJ 739

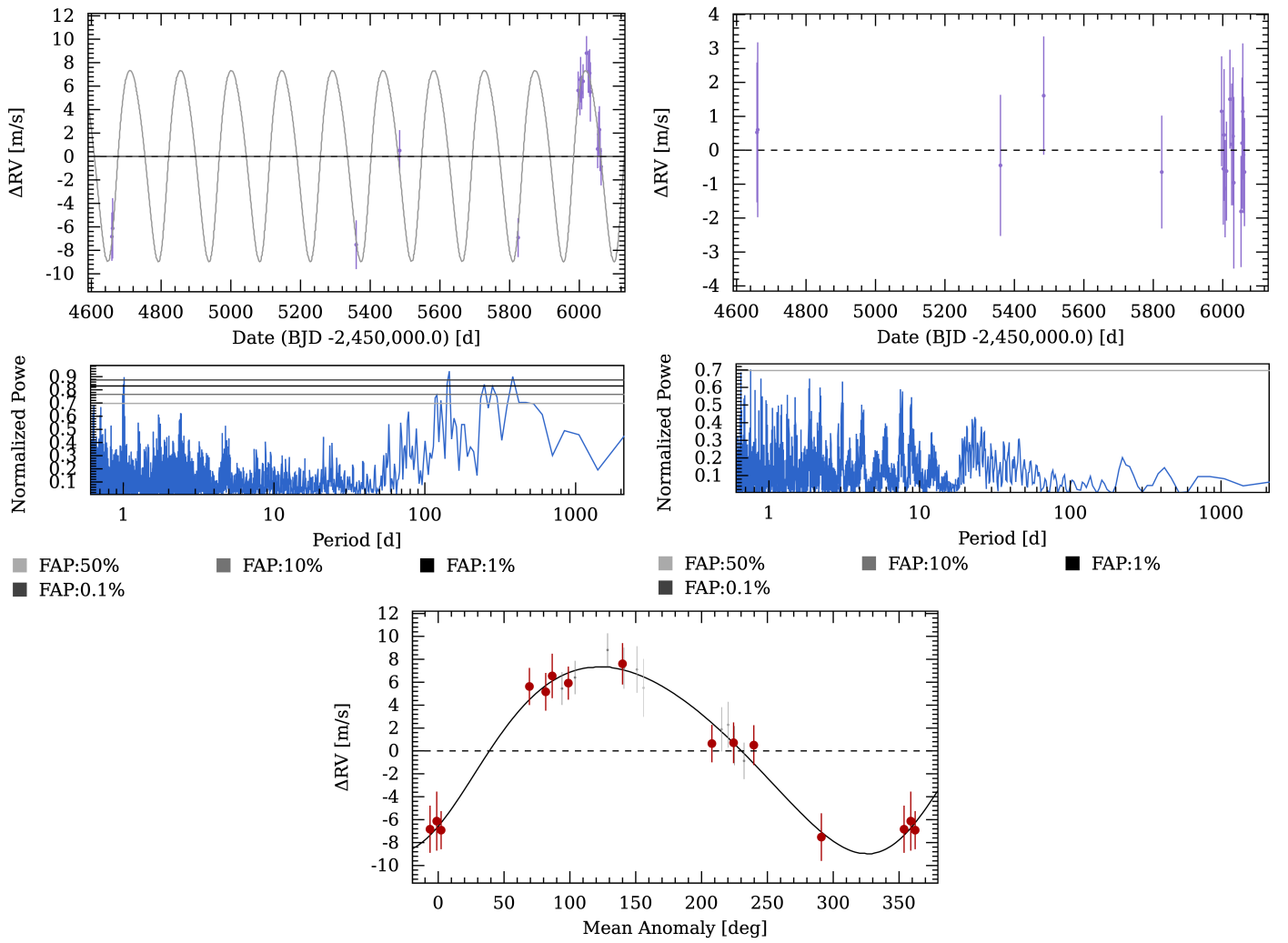


Fig. A.8: RV time series and GLS periodogram of GJ 654. Upper left: RV time series with the Keplerian signal fitted. Upper right: residuals. Middle left: periodogram. Middle right: periodogram of residuals. Bottom: Signal fitted at 145.3 days.

Appendix A.1.8: GJ 754

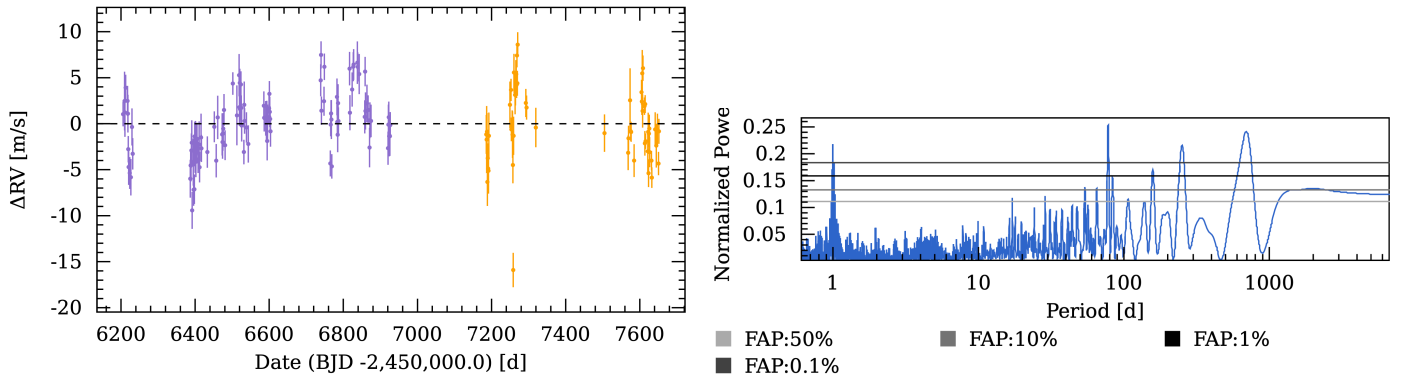


Fig. A.9: RV time series and GLS periodogram of GJ 754 for the four well-monitored seasons (2012–2016).

Appendix A.1.9: GJ 846

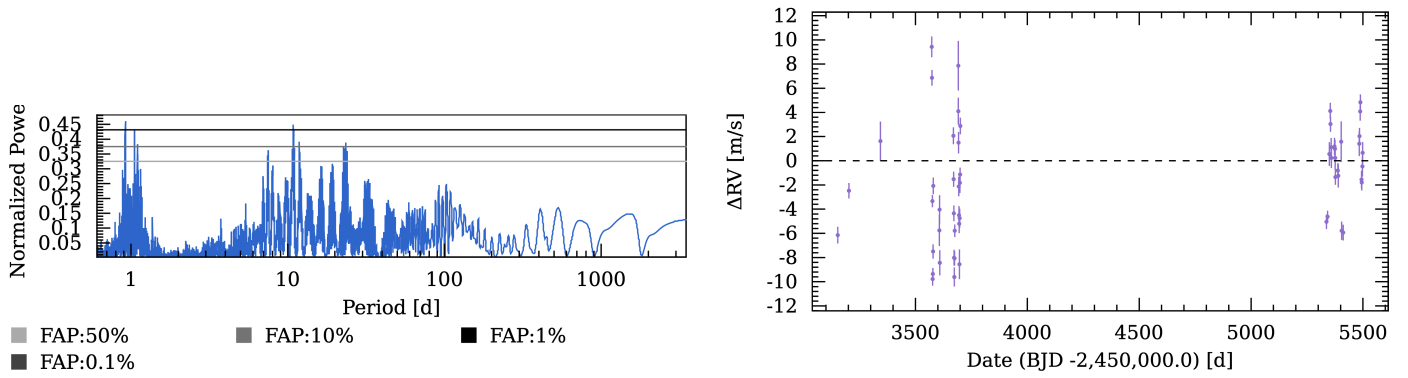


Fig. A.10: RV time series and GLS periodogram of GJ 846 without any correction of long-term trend.

Appendix A.1.10: GJ 880

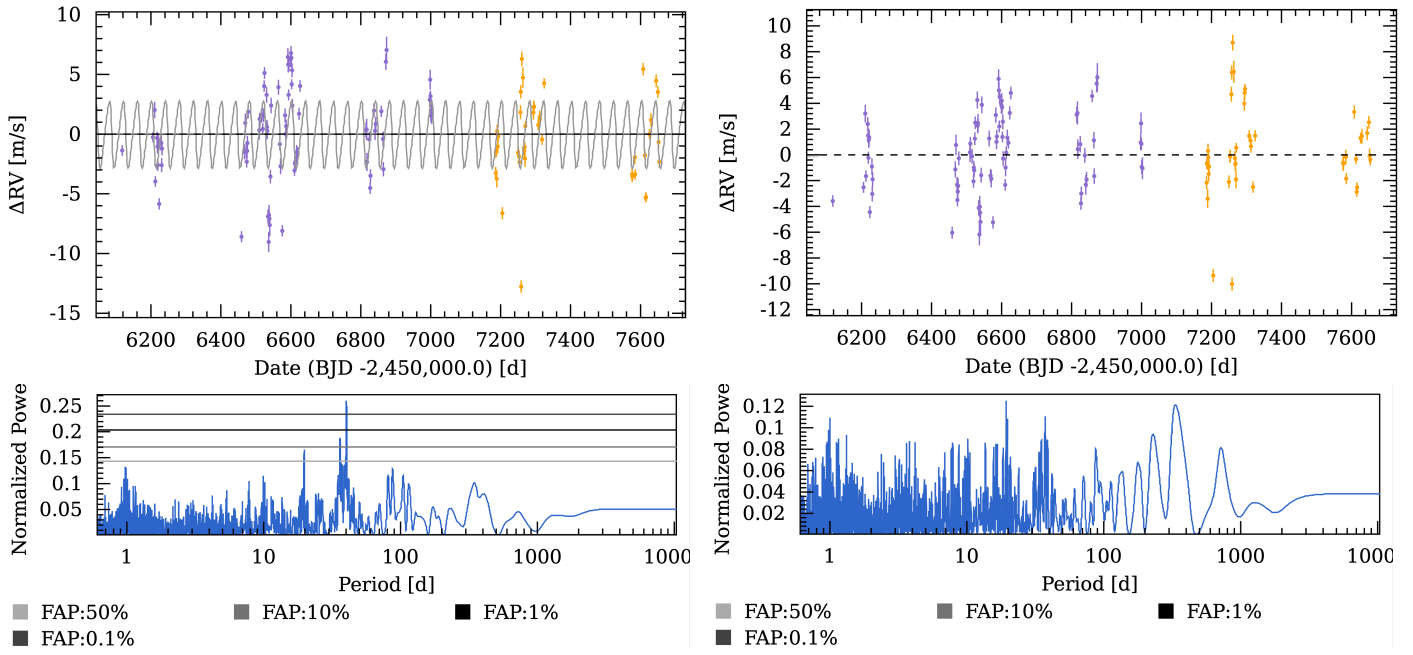


Fig. A.11: RV time series and GLS periodogram of GJ 880. Left: original series, right: residuals.

## Appendix B: Tables

Table B.1: Programme ID and PIs

PI	Prog. ID	PI	Prog. ID	PI	Prog. ID
Bonfils	198.C-0873	Lo Curto	196.C-1006	Udry	192.C-0852
	191.C-0873		099.C-0458		183.C-0972
	183.C-0437		098.C-0366	Lagrange	192.C-0224
	180.C-0886		096.C-0460		099.C-0205
	082.C-0718		095.C-0551		098.C-0739
	1102.C-0339		093.C-0409		089.C-0739
Anglada-Escude	191.C-0505		091.C-0034	Lannier	0104.C-0418
	096.C-0082		090.C-0421		097.C-0864
Astudillo Defru	100.C-0884		089.C-0732	Diaz	098.C-0518
Poretti	185.D-0056		087.C-0831		096.C-0499
Lachaume	089.C-0006		085.C-0019	Ruiz	0100.C-0487
Haswell	097.C-0390		0102.C-0558		090.C-0395
	096.C-0876		0103.C-0432		084.C-0228
Kuerster	097.C-0090		0101.C-0379	Santos	086.C-0284
Mayor	077.C-0364	0100.C-0097	Pepe	089.C-0050	
	072.C-0488	Dall	078.D-0245	Hebrard	078.C-0044
Albrecht	095.C-0718	Sterzik	079.C-0463	Galland	076.C-0279
Guenther	076.C-0010	Melo	076.C-0155	Jeffers	0104.C-0863
	075.C-0202	Robichon	074.C-0364	Trifonov	0100.C-0414
	074.C-0037	Berdinas	0101.D-0494	Debernardi	075.D-0614

Table B.2: Linear and quadratic trend model

Star	Slope (m/s/year)		Quadratic term (m/s/year <sup>2</sup> )		Peak-to-Peak amplitude (m/s)	$\sigma_{\text{res}}$ (m/s)	Span (days)
GJ234	-468.35	± 4.49	-	-	2874.03	29.56	2206
GJ569	-1.53	±	-	-	31.78	8.69	3177
GJ618A	3.418	± 0.26	-	-	25.07	1.75	2429
GJ667C	1.63	± 0.18	-	-	33.64	3.88	5559
GJ682	0.47	± 0.16	-	-	9.58	1.96	2896
GJ707	1.51	± 0.46	-	-	37.11	7.23	3682
GJ864	-52.04	± 1.20	-	-	436.06	11.28	2912
GJ1135	87.03	± 7.34	-	-	241.66	16.12	1082
GJ3090	15.14	± 3.67	-	-	37.93	7.85	326
GJ3141	678.61	± 150.72	-	-	19.72	3.39	9
GJ3279	-724.70	± 91.95	-	-	17.10	2.33	9
GJ3804	-1.16	± 0.36	-	-	10.10	2.24	1082
GJ3813	23.26	± 2.44	-	-	168.35	19.05	1807
GJ4056	-456.73	± 168.32	-	-	16.38	3.96	9
GJ4206	6.67	± 1.02	-	-	50.89	6.40	1413
GJ9568	-49.96	± 2.03	-	-	201.81	5.19	1447
GJ105B	209.08	± 38.08	-0.70	± 0.13	12.76	2.19	2418
GJ126	141.91	± 60.58	-0.46	± 0.20	21.71	2.75	4522
GJ208	20460.44	± 9476.48	-69.53	± 32.19	49.52	10.73	803
GJ229	-27.76	± 9.17	0.09	± 0.03	17.30	2.54	4674
GJ333	1799873.14	± 441529.61	-5992.28	± 1469.82	25.80	5.39	30
GJ334	307.64	± 128.46	-1.03	± 0.43	94.10	18.45	3778
GJ369	-70.20	± 57.39	0.23	± 0.19	8.45	1.87	1459
GJ480	-1733.78	± 961.02	5.74	± 3.19	23.13	5.02	844
GJ634	-5162.42	± 2235.89	17.18	± 7.44	15.91	4.11	538
GJ660	-1991.50	± 1219.15	6.38	± 4.00	184.55	12.56	1231
GJ680	103.69	± 16.45	-0.34	± 0.05	25.32	1.78	3008
GJ1001A	-152.42	± 60.83	0.51	± 0.20	23.35	4.99	2687
GJ1252	-315944.04	± 77842.50	980.94	± 241.69	12.53	2.48	60
GJ2121	3950.66	± 929.67	-13.10	± 3.05	173.08	11.43	1446
GJ3212	-50520.55	± 6885.03	166.96	± 22.75	9.05	1.15	786
GJ3501	-191420.67	± 33619.01	630.27	± 110.76	2940.24	744.23	1836

Table B.2: Linear and quadratic trend model

Star	Slope (m/s/year)		Quadratic term (m/s/year <sup>2</sup> )		Peak-to-Peak amplitude (m/s)	$\sigma_{\text{res}}$ (m/s)	Span (days)
GJ3528	2705.84	± 1189.34	-8.94	± 3.93	10.79	2.50	1601
GJ3530	-19454.02	± 10359.77	64.77	± 34.56	110.07	17.733	500
GJ3634	180.64	± 129.98	-0.56	± 0.42	41.03	4.10	1424
GJ3700	470803.47	± 221255.89	-1564.93	± 735.02	7.87	1.25	9
GJ3779	152.86	± 85.22	-0.55	± 0.28	78.80	2.83	1804
GJ3871	-496.66	± 322.19	1.63	± 1.06	25.51	5.37	1492
GJ3874	-386.73	± 142.09	1.27	± 0.47	11.20	2.41	1395
GJ4079	-1508.31	± 569.57	4.97	± 1.88	26.40	5.30	1493
GJ4088	-105409.22	± 24383.58	347.91	± 80.47	29.19	4.14	727
GJ4332	-310773.31	± 127431.77	970.85	± 398.06	15.05	3.13	63
GJ4364	4365.07	± 1375.04	-14.41	± 4.53	4.42	0.85	496
GJ9066	-465.04	± 181.48	1.60	± 0.61	53.75	6.03	1780
GJ9118B	14770.21	± 300.79	-48.86	± 1.00	217.15	2.32	1103

**Notes.** Parameters fitted and used for the long-term correction.

Table B.3: Offsets computed for the model chosen for each star

Star	Model	Offset (m/s)	Spect. Type	Vsini (km/s)
GJ 54.1	constant	-5.90 ± 0.46	M4	3.4
GJ 87	constant	-1.89 ± 0.58	M1	2.0
GJ 126	quadratic	-8.52 ± 0.75	M1	-
GJ 163	constant	-4.97 ± 1.334	M3.5	-
GJ 176	constant	-7.55 ± 1.075	M2	-
GJ 191	constant	1.94 ± 1.40	M0	3.01
GJ 213	constant	-5.22 ± 1.34	M5	3.41
GJ 229	quadratic	0.14 ± 0.68	M1	2.61
GJ 273	constant	2.88 ± 0.94	M4	2.68
GJ 317	sinusoidal	-3.3 ± 0.27	M3.5	-
GJ 367	constant	-7.34 ± 0.81	M2	-
GJ 393	constant	3.87 ± 1.1	M2	2.28
GJ 447	constant	-5.17 ± 0.79	M5	2.1
GJ 514	constant	-1.56 ± 0.72	M1	2.55
GJ 536	constant	38.56 ± 0.99	M0	4.7
GJ 551	constant	-3.48 ± 0.43	M6	2.7
GJ 588	constant	-7.64 ± 1.08	M3	2.35
GJ 628	constant	-8.80 ± 0.73	M4	2.89
GJ 654	constant	-1.64 ± 0.98	M2	5.7
GJ 667C	linear	-4.51 ± 1.92	M2	-
GJ 674	constant	-5.80 ± 1.30	M3	2.59
GJ 693	constant	-3.44 ± 0.41	M4	3.3
GJ 701	constant	-2.13 ± 0.89	M1	2.47
GJ 752A	constant	-12.76 ± 1.46	M3	2.34
GJ 754	constant	-3.00 ± 0.64	M4.5	-
GJ 803	-	-3.3 ± 0.27	M1	8.5
GJ 849	sinusoidal	20.23 ± 4.82	M3	-
GJ 876	-	-3.3 ± 0.27	M3.5	2.75
GJ 880	constant	-2.06 ± 1.47	M1.5	2.62
GJ 887	constant	-10.84 ± 2.91	M2	2.7
GJ 1214	constant	1.50 ± 2.42	M4	-
GJ 2066	constant	-2.53 ± 0.43	M2	-
GJ 3135	constant	-3.30 ± 0.57	M3	3.7
GJ 3323	constant	-2.94 ± 0.60	M4	3.8
GJ 9482	sinusoidal	-27.10 ± 15.70	M0	-
GJ 9592	constant	-1.19 ± 0.59	M2	2.51
LP816-60	constant	-6.09 ± 0.65	M4	2.7

**Notes.** Offset values obtained according to the chosen long-term model.

Table B.4: Identified signals as rotation signatures

Star	FAP	P (d)	$P_E$ (d)	$P_P$ (d)	Method	Reference
GJ 87	0.004	53.15	72.6	53.05	H $\alpha$	Mignon et al. (2023)
GJ 205	0.0	27.2	21.1	20. 33.4 35	Ph Ph H $\alpha$ , Ca	Hébrard et al. (2016) Suárez Mascareño et al. (2016) Mignon et al. (2023)
GJ 229	0.0	27.60	25.3	27.3 27.6	Ph H $\alpha$ , NaD, Ca	Suárez Mascareño et al. (2016) Mignon et al. (2023)
	0.007	26.51		26.3	Ca	Mignon et al. (2023)
GJ 358	0.0	24.96	21.2	25.4	Ph	Hébrard et al. (2016)
GJ 388	0.0	2.23	-	2.23	VR	Morin et al. (2008)
GJ 393	0.0	38.5	44.6	37.2	Ca	Mignon et al. (2023)
	0.0	33.7				
GJ 406	0.0	2.69	-		Ph	Díez Alonso et al. (2019b)
GJ 447	0.0	61.9	100	123 111	VR H $\alpha$	Bonfils et al. (2018a) Mignon et al. (2023)
GJ 479	0.0	23.10	28.7	24 22.5	Ph Ch	Hébrard et al. (2016) Suárez Mascareño et al. (2015)
	0.01	11.27				
GJ 514	0.0	31.4	33.9		Ch	Suárez Mascareño et al. (2015)
	0.0	32.4		34.0	Ca, NaD	Mignon et al. (2023)
	0.0	15.15		15.1	H $\alpha$ , NaD, Ca	Mignon et al. (2023)
GJ 536	0.0	43.9	32.6	43.1 39. 49.	Ph H $\alpha$ , Ca NaD	Suárez Mascareño et al. (2016) Mignon et al. (2023) Mignon et al. (2023)
GJ 551	0.0	114	28.4		Ca, NaD, H $\alpha$	Mignon et al. (2023)
	0.0	44.6		83		Kiraga & Stepien (2007)
GJ 581	0.0	67	114	127	Ca, NaD, H $\alpha$	Mignon et al. (2023)
GJ 628	0.0	48.3	92.6	93	VR	Astudillo-Defru et al. (2017b)
	0.0	186				
GJ 667C	0.0	90.9	73	90	VR	Robertson & Mahadevan (2014)
	0.001	38.9				
	0.003	82.4				
GJ 674	0.0	36.68	33.3	33.9	Ch	Suárez Mascareño et al. (2015)
	0.007	35.62		35.2	Ph H $\alpha$ , Ca	Suárez Mascareño et al. (2016) Mignon et al. (2023)
	0.009	16.9				
GJ 740	0.002	17.58	23.4		-	Toledo-Padrón et al. (2021)
				18.2 37.2	Ca H $\alpha$	Mignon et al. (2023) Mignon et al. (2023)
GJ 832	0.005	36.73	50	35.8 35.4	Ca H $\alpha$	Mignon et al. (2023) Mignon et al. (2023)
GJ 849	0.0	35.8	58	39.2 39.2	Ch H $\alpha$ , Ca	Suárez Mascareño et al. (2015) Mignon et al. (2023)
GJ 880	0.001	40.17	25.8	37.5 37	Ch H $\alpha$ , NaD, Ca	Suárez Mascareño et al. (2015) Mignon et al. (2023)
GJ 1132	0.0	62.6	63	125	VR	Bonfils et al. (2018a)
GJ 3148	0.0	11.14	16.2		-	-
	0.0	5.67			-	-
GJ 4303	0.002	17.63	15.5	17.5	H $\alpha$ , NaD, Ca	Mignon et al. (2023)

**Notes.** The three periods are i) the period found in the frequency analysis of the RV time series (P), ii) the estimation of the rotation period obtained by the relation with the mean activity level of Astudillo-Defru et al. (2017a) ( $P_E$ ), and iii) the period found in the literature ( $P_P$ ). The 0.0 FAP value corresponds to a value under the  $10^{-3}$  threshold.

Table B.5: Stellar parameters

Star	Mass ( $M_{\odot}$ )	Spectral Type	Distance (pc)	Magnitudes				
				V	K	J	G	H
BD-15869	0.6089	M0	25.0996	10.881	7.198	8.053	10.1618	7.414
CD-2417578	0.5642	M0V	23.1946	10.847	7.253	8.103	10.1758	7.448

*Continued on next page*

Table B.5: Stellar parameters

Star	Mass ( $M_{\odot}$ )	Spectral Type	Distance (pc)	Magnitudes				
				V	K	J	G	H
CD-246144	0.6686	M0	17.7978	9.715	6.169	7.021	9.0853	6.372
CD-281745	0.606	M0V	15.6683	10.07	6.19	7.04	9.2505	6.42
CD-301270	0.5649	M1V	22.047	10.998	7.115	7.986	10.2204	7.356
CD-4114656	0.6001	M0V	23.6596	10.544	7.139	7.936	9.9321	7.303
G80-21	0.4841	M3.0V	16.8022	11.537	6.933	7.804	10.4962	7.174
G 161-7	0.192	M5.0V	7.4129	13.8	7.733	8.605	11.9686	8.074
G 161-71	0.2811	M5.0V	13.1277	13.646	7.601	8.496	11.9081	7.919
G 272-10	0.2409	-	15.7114	13.009	8.35	9.181	11.8578	8.63
GJ 1	0.3936	M2V	4.3453	8.562	4.535	5.328	7.6819	4.732
GJ 7	0.4524	M0V	23.7425	11.67	7.856	8.655	10.9187	8.143
GJ 12	0.2418	M4V	12.2143	12.6	7.807	8.619	11.3963	8.068
GJ 16	0.5275	M1V	16.7799	10.864	6.741	7.564	10.0009	6.922
GJ 46	0.3566	M3V	11.9735	11.801	6.892	7.763	10.5653	7.203

Notes. Properties of the 425 stars in the sample available online.

Table B.6: Parameters of the long-term analysis.

Star	$N_{mes}$	$\chi_{0*}^2$	$P(\chi_0^2)$	$P(F_{value_0})$	$\chi_{1*}^2$	$P(F_{0/1})$	FAP (%)	$\chi_{2*}^2$	$P(F_{0/2})$	$P(F_{1/2})$
CD-246144	13	<b>2.51</b>	<b>0.001</b>	<b>0.097</b>	<b>2.664</b>	0.996	64.8	<b>2.902</b>	0.997	<b>1.0</b>
CD-281745	15	21.90	<b>0.0</b>	<b>0.0</b>	16.405	<b>0.0026</b>	7.8	17.056	<b>0.002</b>	<b>0.939</b>
CD-4114656	21	13.26	<b>0.0</b>	<b>0.0</b>	13.304	0.687	38.4	13.991	0.712	<b>1.0</b>
G80-21	12	522.44	<b>0.0</b>	<b>0.0</b>	550.06	0.974	61.7	576.72	0.758	<b>0.904</b>
GJ 1	46	4.79	<b>0.0</b>	<b>0.0</b>	4.617	<b>0.0009</b>	10.8	3.962	<b>0.0</b>	<b>0.0</b>
GJ 7	10	<b>2.14</b>	<b>0.011</b>	<b>0.147</b>	<b>2.073</b>	0.52	32.2	<b>2.323</b>	0.581	<b>1.0</b>
GJ 54.1	256	3.88	<b>0.0</b>	<b>0.0</b>	3.89	1.0	45.2	3.497	<b>0.0</b>	<b>0.0</b>
GJ 85	11	9.67	<b>0.0</b>	<b>0.002</b>	9.32	0.474	29.0	6.025	<b>0.003</b>	<b>0.004</b>
GJ 87	154	<b>1.83</b>	<b>0.0</b>	<b>0.0</b>	<b>1.822</b>	<b>0.0</b>	15.9	<b>1.806</b>	<b>0.0</b>	<b>0.0</b>
GJ 91	26	5.29	<b>0.0</b>	<b>0.0</b>	5.163	0.17	24.3	5.317	0.102	<b>0.999</b>
GJ 93	19	<b>2.19</b>	<b>0.001</b>	<b>0.082</b>	<b>2.244</b>	0.946	88.8	<b>2.001</b>	<b>0.008</b>	<b>0.011</b>
GJ 105B	22	4.63	<b>0.0</b>	<b>0.001</b>	4.692	0.859	91.9	<b>1.794</b>	<b>0.0</b>	<b>0.0</b>
GJ 118	20	4.63	<b>0.0</b>	<b>0.001</b>	<b>2.604</b>	<b>0.0</b>	<b>0.1</b>	<b>2.244</b>	<b>0.0</b>	<b>0.002</b>
GJ 126	32	3.61	<b>0.0</b>	<b>0.002</b>	<b>2.253</b>	<b>0.0</b>	<b>0.0</b>	<b>2.328</b>	<b>0.0</b>	<b>1.0</b>
GJ 157B	16	340.68	<b>0.0</b>	<b>0.0</b>	302.66	<b>0.0438</b>	81.7	323.21	0.054	<b>1.0</b>
GJ 163	179	14.03	<b>0.0</b>	<b>0.0</b>	14.08	1.0	63.1	13.70	<b>0.0</b>	<b>0.0</b>
GJ 173	16	<b>2.67</b>	<b>0.0</b>	<b>0.066</b>	<b>2.477</b>	0.123	17.4	<b>1.449</b>	<b>0.0</b>	<b>0.0</b>
GJ 176	115	17.84	<b>0.0</b>	<b>0.0</b>	15.94	<b>0.0</b>	<b>0.2</b>	15.763	<b>0.0</b>	<b>0.0</b>
GJ 179	22	40.10	<b>0.0</b>	<b>0.0</b>	31.973	<b>0.0001</b>	2.2	7.461	<b>0.0</b>	<b>0.0</b>
GJ 180	49	6.21	<b>0.0</b>	<b>0.0</b>	6.279	0.999	63.7	6.402	0.996	<b>1.0</b>
GJ 182	16	6687.65	<b>0.0</b>	<b>0.0</b>	7101.31	1.0	84.6	5700.64	<b>0.006</b>	<b>0.003</b>
GJ 191	228	4.64	<b>0.0</b>	<b>0.0</b>	4.649	1.0	87.6	4.073	<b>0.0</b>	<b>0.0</b>
GJ 203	10	<b>2.168</b>	<b>0.01</b>	0.28	<b>1.987</b>	0.321	26.1	<b>1.419</b>	<b>0.011</b>	<b>0.021</b>
GJ 205	103	287.40	<b>0.0</b>	<b>0.0</b>	194.733	<b>0.0</b>	<b>0.0</b>	186.496	<b>0.0</b>	<b>0.0</b>
GJ 208	18	52.128	<b>0.0</b>	<b>0.0</b>	29.734	<b>0.0</b>	<b>0.4</b>	23.326	<b>0.0</b>	<b>0.001</b>
GJ 213	122	4.44	<b>0.0</b>	<b>0.0</b>	4.362	<b>0.0</b>	7.3	4.18	<b>0.0</b>	<b>0.0</b>
GJ 221	110	24.57	<b>0.0</b>	<b>0.0</b>	23.796	<b>0.0</b>	6.6	23.172	<b>0.0</b>	<b>0.0</b>
GJ 229	200	10.41	<b>0.0</b>	<b>0.0</b>	8.467	<b>0.0</b>	<b>0.0</b>	8.101	<b>0.0</b>	<b>0.0</b>
GJ 234	20	$>10^4$	<b>0.0</b>	<b>0.0</b>	290.983	<b>0.0</b>	<b>0.0</b>	158.446	<b>0.0</b>	<b>0.0</b>
GJ 250B	12	<b>1.514</b>	0.078	0.389	<b>1.604</b>	0.987	75.1	<b>1.584</b>	0.434	0.471
GJ 273	315	7.26	<b>0.0</b>	<b>0.0</b>	7.019	<b>0.0</b>	<b>0.2</b>	7.011	<b>0.0</b>	<b>0.003</b>
GJ 282C	10	8288.96	<b>0.0</b>	<b>0.0</b>	145.849	<b>0.0</b>	<b>0.0</b>	24.053	<b>0.0</b>	<b>0.0</b>
GJ 299	24	4.19	<b>0.0</b>	<b>0.001</b>	3.769	<b>0.0032</b>	10.3	3.535	<b>0.0</b>	<b>0.019</b>
GJ 300	39	10.27	<b>0.0</b>	<b>0.0</b>	10.255	0.508	34.0	9.387	<b>0.0</b>	<b>0.0</b>
GJ 317	137	210.70	<b>0.0</b>	<b>0.0</b>	153.206	<b>0.0</b>	<b>0.0</b>	145.64	<b>0.0</b>	<b>0.0</b>
GJ 333	11	6.419	<b>0.0</b>	<b>0.003</b>	4.825	<b>0.0305</b>	9.9	<b>2.946</b>	<b>0.0</b>	<b>0.003</b>
GJ 334	26	214.704	<b>0.0</b>	<b>0.0</b>	182.354	<b>0.0001</b>	4.8	151.038	<b>0.0</b>	<b>0.0</b>
GJ 341	57	4.538	<b>0.0</b>	<b>0.0</b>	3.809	<b>0.0</b>	<b>0.0</b>	3.713	<b>0.0</b>	<b>0.001</b>
GJ 357	48	7.575	<b>0.0</b>	<b>0.0</b>	7.729	1.0	91.3	7.897	1.0	<b>1.0</b>
GJ 358	34	24.089	<b>0.0</b>	<b>0.0</b>	22.244	<b>0.0003</b>	8.0	22.655	<b>0.0</b>	<b>0.996</b>
GJ 361	101	10.066	<b>0.0</b>	<b>0.0</b>	9.922	<b>0.0</b>	16.5	10.01	<b>0.0</b>	<b>1.0</b>
GJ 367	24	6.625	<b>0.0</b>	<b>0.0</b>	6.902	1.0	98.1	6.525	<b>0.042</b>	<b>0.029</b>
GJ 369	45	4.051	<b>0.0</b>	<b>0.0</b>	<b>2.771</b>	<b>0.0</b>	<b>0.0</b>	<b>2.733</b>	<b>0.0</b>	0.068
GJ 377	11	$>10^4$	<b>0.0</b>	<b>0.0</b>	$>10^4$	<b>0.0006</b>	79.0	$>10^4$	<b>0.0</b>	0.204

Continued on next page

Table B.6: Parameters of the long-term analysis.

Star	$N_{mes}$	$\chi^2_{0s}$	$P(\chi^2_0)$	$P(F_{value_0})$	$\chi^2_{2s}$	$P(F_{0/1})$	FAP (%)	$\chi^2_{2s}$	$P(F_{0/2})$	$P(F_{1/2})$
GJ 382	33	25.708	<b>0.0</b>	<b>0.0</b>	22.708	<b>0.0</b>	6.8	23.124	<b>0.0</b>	<b>0.993</b>
GJ 388	56	261.576	<b>0.0</b>	<b>0.0</b>	245.797	<b>0.0</b>	7.2	247.617	<b>0.0</b>	<b>0.969</b>
GJ 390	46	6.233	<b>0.0</b>	<b>0.0</b>	6.329	1.0	60.3	6.386	0.715	<b>0.962</b>
GJ 393	175	4.824	<b>0.0</b>	<b>0.0</b>	4.776	<b>0.0</b>	15.6	4.755	<b>0.0</b>	<b>0.0</b>
GJ 406	34	17.355	<b>0.0</b>	<b>0.0</b>	17.427	0.758	61.7	17.507	0.104	<b>0.71</b>
GJ 422	40	6.606	<b>0.0</b>	<b>0.0</b>	6.754	1.0	74.6	6.927	1.0	<b>1.0</b>
GJ 433	86	8.065	<b>0.0</b>	<b>0.0</b>	8.158	1.0	90.9	8.074	<b>0.003</b>	<b>0.002</b>
GJ 438	19	<b>1.482</b>	0.06	0.319	<b>1.438</b>	0.271	25.6	<b>1.522</b>	0.309	<b>1.0</b>
GJ 443	18	31.888	<b>0.0</b>	<b>0.0</b>	30.783	0.255	24.3	25.461	<b>0.0</b>	<b>0.002</b>
GJ 447	156	3.353	<b>0.0</b>	<b>0.0</b>	<b>2.895</b>	<b>0.0</b>	<b>0.0</b>	<b>2.832</b>	<b>0.0</b>	<b>0.0</b>
GJ 465	23	<b>2.3</b>	<b>0.0</b>	<b>0.058</b>	<b>2.111</b>	<b>0.0123</b>	10.6	<b>2.209</b>	<b>0.015</b>	<b>1.0</b>
GJ 476	12	<b>1.734</b>	<b>0.035</b>	<b>0.134</b>	<b>1.621</b>	0.291	16.1	<b>1.728</b>	0.24	<b>0.977</b>
GJ 479	58	11.504	<b>0.0</b>	<b>0.0</b>	11.676	1.0	70.1	11.108	<b>0.0</b>	<b>0.0</b>
il GJ 480	37	12.896	<b>0.0</b>	<b>0.0</b>	10.854	<b>0.0</b>	1.6	9.904	<b>0.0</b>	<b>0.0</b>
GJ 486	12	3.424	<b>0.0</b>	<b>0.039</b>	3.428	0.683	36.8	3.658	0.549	<b>0.979</b>
GJ 488	10	10.315	<b>0.0</b>	<b>0.002</b>	11.168	0.995	71.4	9.791	0.196	0.145
GJ 510	13	<b>2.89</b>	<b>0.0</b>	<b>0.112</b>	3.066	0.997	94.2	3.331	0.995	<b>1.0</b>
GJ 514	160	7.484	<b>0.0</b>	<b>0.0</b>	7.327	<b>0.0</b>	5.3	7.2	<b>0.0</b>	<b>0.0</b>
GJ 526	32	8.553	<b>0.0</b>	<b>0.0</b>	8.72	0.998	59.2	8.989	0.993	<b>1.0</b>
GJ 536	195	15.579	<b>0.0</b>	<b>0.0</b>	40.643	1	100.0	14.397	<b>0.0</b>	<b>0.0</b>
GJ 550.3	42	415.302	<b>0.0</b>	<b>0.0</b>	261.46	<b>0.0</b>	<b>0.0</b>	229.617	<b>0.0</b>	<b>0.0</b>
GJ 551	246	3.841	<b>0.0</b>	<b>0.0</b>	3.723	<b>0.0</b>	8.3	3.505	<b>0.0</b>	<b>0.0</b>
GJ 555	14	5.88	<b>0.0</b>	<b>0.003</b>	4.016	<b>0.0013</b>	3.1	3.929	<b>0.001</b>	0.372
GJ 569A	24	49.812	<b>0.0</b>	<b>0.0</b>	38.996	<b>0.0</b>	1.4	40.748	<b>0.0</b>	<b>1.0</b>
GJ 570B	340	>10 <sup>4</sup>	<b>0.0</b>	<b>0.0</b>	>10 <sup>4</sup>	<b>0.0</b>	<b>0.0</b>	>10 <sup>4</sup>	<b>0.0</b>	<b>0.0</b>
GJ 581	242	70.351	<b>0.0</b>	<b>0.0</b>	70.602	1.0	77.0	70.883	1.0	<b>1.0</b>
GJ 588	75	5.186	<b>0.0</b>	<b>0.0</b>	4.007	<b>0.0</b>	<b>0.0</b>	3.709	<b>0.0</b>	<b>0.0</b>
GJ 606	23	3.373	<b>0.0</b>	<b>0.001</b>	3.36	0.552	65.9	3.295	<b>0.033</b>	0.227
GJ 618A	20	25.464	<b>0.0</b>	<b>0.0</b>	<b>2.5</b>	<b>0.0</b>	<b>0.0</b>	<b>2.556</b>	<b>0.0</b>	<b>0.902</b>
GJ 620	22	4.54	<b>0.0</b>	<b>0.003</b>	4.4	0.189	36.9	3.832	<b>0.0</b>	<b>0.001</b>
GJ 628	189	7.717	<b>0.0</b>	<b>0.0</b>	7.748	1.0	81.7	7.789	1.0	<b>1.0</b>
GJ 634	23	4.649	<b>0.0</b>	<b>0.004</b>	3.687	<b>0.0</b>	5.3	3.045	<b>0.0</b>	<b>0.0</b>
GJ 637	17	<b>1.524</b>	0.055	0.4	<b>1.614</b>	1.0	87.2	<b>1.697</b>	0.998	<b>0.999</b>
GJ 645	10	<b>0.528</b>	0.809	0.789	<b>0.372</b>	<b>0.0299</b>	4.0	<b>0.355</b>	<b>0.013</b>	0.348
GJ 654	193	4.836	<b>0.0</b>	<b>0.0</b>	4.785	<b>0.0</b>	14.1	4.78	<b>0.0</b>	0.078
GJ 660	15	420.748	<b>0.0</b>	<b>0.0</b>	51.503	<b>0.0</b>	<b>0.0</b>	45.789	<b>0.0</b>	<b>0.042</b>
GJ 667C	248	13.551	<b>0.0</b>	<b>0.0</b>	9.669	<b>0.0</b>	<b>0.0</b>	9.707	<b>0.0</b>	<b>1.0</b>
GJ 674	212	43.018	<b>0.0</b>	<b>0.0</b>	43.111	1.0	50.1	42.871	<b>0.0</b>	<b>0.0</b>
GJ 676A	125	4218.153	<b>0.0</b>	<b>0.0</b>	2228.731	<b>0.0</b>	<b>0.0</b>	2235.63	<b>0.0</b>	<b>0.997</b>
GJ 680	39	25.65	<b>0.0</b>	<b>0.0</b>	4.326	<b>0.0</b>	<b>0.0</b>	<b>2.15</b>	<b>0.0</b>	<b>0.0</b>
GJ 682	21	3.56	<b>0.0</b>	<b>0.002</b>	<b>2.393</b>	<b>0.0</b>	0.8	<b>2.468</b>	<b>0.0</b>	<b>0.985</b>
GJ 686	20	5.61	<b>0.0</b>	<b>0.0</b>	5.486	0.319	24.8	5.422	<b>0.038</b>	0.37
GJ 693	179	4.18	<b>0.0</b>	<b>0.0</b>	4.17	1.0	80.3	4.16	<b>0.0</b>	<b>0.0</b>
GJ 696	42	5.26	<b>0.0</b>	<b>0.0</b>	5.15	<b>0.032</b>	29.3	4.54	<b>0.0</b>	<b>0.0</b>
GJ 699	117	5.28	<b>0.0</b>	<b>0.0</b>	5.201	<b>0.0</b>	14.9	4.762	<b>0.0</b>	<b>0.0</b>
GJ 701	153	4.79	<b>0.0</b>	<b>0.0</b>	4.77	<b>0.0006</b>	21.8	4.80	<b>0.0</b>	<b>1.0</b>
GJ 707	17	51.62	<b>0.0</b>	<b>0.0</b>	31.74	<b>0.0</b>	1.4	33.75	<b>0.0</b>	<b>1.0</b>
GJ 723	10	12.441	<b>0.0</b>	<b>0.001</b>	9.03	<b>0.0384</b>	7.4	5.479	<b>0.001</b>	<b>0.006</b>
GJ 724	27	12.48	<b>0.0</b>	<b>0.0</b>	12.77	0.996	55.0	11.86	<b>0.003</b>	<b>0.004</b>
GJ 729	29	93.37	<b>0.0</b>	<b>0.0</b>	83.06	<b>0.0002</b>	9.2	70.97	<b>0.0</b>	<b>0.0</b>
GJ 739	19	5.42	<b>0.0</b>	<b>0.001</b>	4.83	<b>0.0171</b>	9.1	4.82	<b>0.004</b>	<b>0.502</b>
GJ 740	54	19.21	<b>0.0</b>	<b>0.0</b>	18.73	<b>0.0017</b>	12.3	19.01	<b>0.001</b>	<b>1.0</b>
GJ 752A	147	11.30	<b>0.0</b>	<b>0.0</b>	10.90	<b>0.0</b>	0.9	10.65	<b>0.0</b>	<b>0.0</b>
GJ 754	182	3.67	<b>0.0</b>	<b>0.0</b>	3.67	0.194	26.9	3.69	0.204	<b>1.0</b>
GJ 784	39	15.41	<b>0.0</b>	<b>0.0</b>	15.32	0.359	58.4	14.95	<b>0.001</b>	<b>0.025</b>
GJ 800A	30	<b>2.886</b>	<b>0.0</b>	<b>0.006</b>	<b>2.623</b>	<b>0.0004</b>	5.8	<b>2.546</b>	<b>0.0</b>	0.056
GJ 803	48	4993.01	<b>0.0</b>	<b>0.0</b>	5494.86	1	100.0	4804.53	<b>0.0</b>	<b>0.0</b>
GJ 816	19	4.238	<b>0.0</b>	<b>0.005</b>	3.593	<b>0.0036</b>	7.6	3.659	<b>0.002</b>	<b>0.83</b>
GJ 821	11	<b>1.456</b>	0.099	0.428	<b>1.416</b>	0.52	28.2	<b>1.369</b>	0.146	0.375
GJ 825	20	8.322	<b>0.0</b>	<b>0.0</b>	6.605	<b>0.0003</b>	1.9	6.947	<b>0.0</b>	<b>1.0</b>
GJ 832	60	116.00	<b>0.0</b>	<b>0.0</b>	21.90	<b>0.0</b>	<b>0.0</b>	21.68	<b>0.0</b>	<b>0.045</b>
GJ 842	10	4.537	<b>0.0</b>	<b>0.039</b>	<b>2.327</b>	<b>0.0028</b>	2.1	<b>2.583</b>	<b>0.004</b>	<b>0.999</b>
GJ 846	55	15.78	<b>0.0</b>	<b>0.0</b>	14.40	<b>0.0</b>	1.5	14.66	<b>0.0</b>	<b>1.0</b>
GJ 849	71	185.51	<b>0.0</b>	<b>0.0</b>	181.67	<b>0.0001</b>	22.4	180.21	<b>0.0</b>	<b>0.033</b>
GJ 855	35	10.04	<b>0.0</b>	<b>0.0</b>	10.28	1.0	98.5	10.37	0.731	<b>0.859</b>
GJ 864	15	8193.9	<b>0.0</b>	<b>0.0</b>	58.573	<b>0.0</b>	<b>0.0</b>	61.134	<b>0.0</b>	<b>0.96</b>

Continued on next page

Table B.6: Parameters of the long-term analysis.

Star	$N_{mes}$	$\chi^2_{0s}$	$P(\chi^2_0)$	$P(F_{value_0})$	$\chi^2_{1s}$	$P(F_{0/1})$	FAP (%)	$\chi^2_{2s}$	$P(F_{0/2})$	$P(F_{1/2})$
GJ 871.1A	28	5062.77	<b>0.0</b>	<b>0.0</b>	4954.25	0.171	33.7	4666.37	<b>0.0</b>	<b>0.008</b>
GJ 876	256	>10 <sup>4</sup>	<b>0.0</b>	<b>0.0</b>	>10 <sup>4</sup>	<b>0.0</b>	<b>0.0</b>	>10 <sup>4</sup>	<b>0.0</b>	<b>1.0</b>
GJ 877	42	13.18	<b>0.0</b>	<b>0.0</b>	13.04	0.179	25.3	13.31	0.111	<b>1.0</b>
GJ 880	140	12.81	<b>0.0</b>	<b>0.0</b>	12.83	0.932	41.0	12.377	<b>0.0</b>	<b>0.0</b>
GJ 887	154	21.143	<b>0.0</b>	<b>0.0</b>	20.291	<b>0.0</b>	1.0	19.605	<b>0.0</b>	<b>0.0</b>
GJ 891	28	4.541	<b>0.0</b>	<b>0.0</b>	4.664	1.0	62.7	4.843	1.0	<b>1.0</b>
GJ 900	13	425.316	<b>0.0</b>	<b>0.0</b>	401.119	0.286	23.8	386.728	0.057	0.307
GJ 908	87	4.41	<b>0.0</b>	<b>0.0</b>	4.135	<b>0.0</b>	1.6	4.138	<b>0.0</b>	<b>0.643</b>
GJ 1001A	25	7.792	<b>0.0</b>	<b>0.0</b>	7.112	<b>0.0045</b>	8.4	5.931	<b>0.0</b>	<b>0.0</b>
GJ 1009	12	<b>2.165</b>	<b>0.007</b>	0.247	<b>1.567</b>	<b>0.0113</b>	6.3	<b>1.7</b>	<b>0.014</b>	<b>0.999</b>
GJ 1018	15	6.902	<b>0.0</b>	<b>0.001</b>	4.536	<b>0.0003</b>	2.5	4.634	<b>0.0</b>	<b>0.784</b>
GJ 1032	10	4.645	<b>0.0</b>	<b>0.055</b>	4.092	0.221	21.5	4.48	0.224	<b>0.99</b>
GJ 1046	20	>10 <sup>4</sup>	<b>0.0</b>	<b>0.0</b>	>10 <sup>4</sup>	0.714	41.9	>10 <sup>4</sup>	<b>0.0</b>	<b>0.0</b>
GJ 1050	10	<b>1.484</b>	0.096	0.239	<b>1.454</b>	0.59	32.3	<b>1.31</b>	0.106	0.192
GJ 1061	111	397.06	<b>0.0</b>	<b>0.0</b>	168.883	<b>0.0</b>	<b>0.0</b>	147.826	<b>0.0</b>	<b>0.0</b>
GJ 1075	35	11.051	<b>0.0</b>	<b>0.0</b>	11.33	1.0	88.5	11.19	0.153	0.178
GJ 1084	10	79.49	<b>0.0</b>	<b>0.0</b>	83.49	0.929	71.0	88.52	0.712	<b>0.888</b>
GJ 1132	117	4.20	<b>0.0</b>	<b>0.0</b>	4.185	<b>0.0333</b>	42.1	3.403	<b>0.0</b>	<b>0.0</b>
GJ 1135	18	1787.75	<b>0.0</b>	<b>0.0</b>	179.97	<b>0.0</b>	<b>0.0</b>	177.16	<b>0.0</b>	0.354
GJ 1214	112	6.35	<b>0.0</b>	<b>0.0</b>	6.361	0.941	46.1	6.406	0.594	<b>1.0</b>
GJ 1236	11	<b>2.58</b>	<b>0.002</b>	<b>0.109</b>	<b>2.819</b>	1.0	91.4	<b>1.8</b>	<b>0.009</b>	<b>0.004</b>
GJ 1248	10	<b>0.57</b>	0.77	0.879	<b>0.585</b>	0.831	69.5	<b>0.639</b>	0.742	<b>0.986</b>
GJ 1284	22	>10 <sup>4</sup>	<b>0.0</b>	<b>0.0</b>	>10 <sup>4</sup>	1.0	91.2	>10 <sup>4</sup>	0.997	<b>1.0</b>
GJ 2003	41	<b>2.772</b>	<b>0.0</b>	<b>0.006</b>	<b>2.792</b>	0.914	49.0	<b>2.465</b>	<b>0.0</b>	<b>0.0</b>
GJ 2060	11	>10 <sup>4</sup>	<b>0.0</b>	<b>0.0</b>	7084.75	<b>0.0019</b>	73.2	7859.99	<b>0.003</b>	<b>1.0</b>
GJ 2066	111	<b>2.516</b>	<b>0.0</b>	<b>0.0</b>	<b>2.421</b>	<b>0.0</b>	1.9	<b>2.419</b>	<b>0.0</b>	0.342-
GJ 2121	28	121.59	<b>0.0</b>	<b>0.0</b>	37.70	<b>0.0</b>	<b>0.0</b>	22.55	<b>0.0</b>	<b>0.0</b>
GJ 3009	11	13.84	<b>0.0</b>	<b>0.002</b>	15.20	1.0	96.7	15.47	0.781	<b>0.673</b>
GJ 3018	25	4.151	<b>0.0</b>	<b>0.001</b>	3.938	<b>0.0387</b>	16.2	3.744	<b>0.0</b>	<b>0.032</b>
GJ 3053	224	<b>2.517</b>	<b>0.0</b>	<b>0.0</b>	<b>2.524</b>	1.0	93.5	<b>2.535</b>	1.0	<b>1.0</b>
GJ 3082	42	4.173	<b>0.0</b>	<b>0.0</b>	4.256	1.0	86.1	4.295	0.823	<b>0.945</b>
GJ 3090	25	7.013	<b>0.0</b>	<b>0.0</b>	6.914	0.329	34.5	6.744	<b>0.01</b>	0.146
GJ 3102	26	14.23	<b>0.0</b>	<b>0.0</b>	8.03	<b>0.0</b>	<b>0.0</b>	4.54	<b>0.0</b>	<b>0.0</b>
GJ 3135	168	<b>1.61</b>	<b>0.0</b>	<b>0.0</b>	<b>1.578</b>	<b>0.0</b>	7.2	<b>1.568</b>	<b>0.0</b>	<b>0.0</b>
GJ 3141	10	12.86	<b>0.0</b>	<b>0.001</b>	4.029	<b>0.0001</b>	<b>0.3</b>	4.95	<b>0.0</b>	<b>1</b>
GJ 3148	62	26.445	<b>0.0</b>	<b>0.0</b>	26.126	<b>0.0229</b>	31.1	25.764	<b>0.0</b>	<b>0.01</b>
GJ 3189	10	<b>1.80</b>	<b>0.035</b>	0.384	<b>1.928</b>	0.977	67.1	<b>2.144</b>	0.965	<b>1.0</b>
GJ 3205	20	<b>2.58</b>	<b>0.0</b>	<b>0.063</b>	<b>2.398</b>	0.05	17.2	<b>2.53</b>	0.063	<b>1.0</b>
GJ 3212	12	<b>2.56</b>	<b>0.001</b>	<b>0.144</b>	<b>2.462</b>	0.418	28.3	<b>2.675</b>	0.421	<b>1.0</b>
GJ 3218	45	10.82	<b>0.0</b>	<b>0.0</b>	11.016	1.0	67.5	10.792	<b>0.013</b>	<b>0.019</b>
GJ 3221	28	5.42	<b>0.0</b>	<b>0.0</b>	5.48	0.896	59.6	5.66	0.8	<b>1.0</b>
GJ 3256	29	7.88	<b>0.0</b>	<b>0.0</b>	6.61	<b>0.0</b>	2.1	6.815	<b>0.0</b>	<b>1.0</b>
GJ 3279	11	14.72	<b>0.0</b>	<b>0.001</b>	9.139	<b>0.005</b>	0.8	<b>2.669</b>	<b>0.0</b>	<b>0.0</b>
GJ 3293	201	14.04	<b>0.0</b>	<b>0.0</b>	14.05	0.811	90.3	14.12	0.774	<b>1.0</b>
GJ 3307	20	>10 <sup>4</sup>	<b>0.0</b>	<b>0.0</b>	1960.572	<b>0.0</b>	<b>0.0</b>	29.07	<b>0.0</b>	<b>0.0</b>
GJ 3323	148	<b>2.581</b>	<b>0.0</b>	<b>0.0</b>	<b>2.591</b>	1.0	78.4	<b>2.609</b>	1.0	<b>1.0</b>
GJ 3331	19	5468.52	<b>0.0</b>	<b>0.0</b>	5099.43	0.072	69.0	5248.26	<b>0.037</b>	<b>0.947</b>
GJ 3341	134	<b>2.57</b>	<b>0.0</b>	<b>0.0</b>	<b>2.603</b>	1.0	75.0	<b>2.602</b>	0.216	0.391
GJ 3356	10	<b>0.54</b>	0.797	0.859	<b>0.502</b>	0.364	25.7	<b>0.541</b>	0.306	<b>0.952</b>
GJ 3379	14	2434.22	<b>0.0</b>	<b>0.0</b>	2294.17	0.245	24.1	2485.33	0.296	<b>1.0</b>
GJ 3403	14	4.67	<b>0.0</b>	<b>0.012</b>	5.023	1.0	96.4	5.186	0.912	<b>0.858</b>
GJ 3404	13	<b>0.87</b>	0.502	0.45	<b>0.883</b>	0.787	84.5	<b>0.826</b>	0.107	0.185
GJ 3455	12	<b>2.67</b>	<b>0.001</b>	<b>0.164</b>	<b>2.757</b>	0.887	92.3	<b>2.279</b>	<b>0.036</b>	<b>0.037</b>
GJ 3501	11	>10 <sup>4</sup>	<b>0.0</b>	<b>0.0</b>	>10 <sup>4</sup>	0.344	53.2	>10 <sup>4</sup>	<b>0.0</b>	<b>0.0</b>
GJ 3502	22	<b>1.78</b>	<b>0.009</b>	0.222	<b>1.327</b>	<b>0.0</b>	1.3	<b>0.918</b>	<b>0.0</b>	<b>0.0</b>
GJ 3528	15	3.28	<b>0.0</b>	<b>0.039</b>	3.402	0.965	63.0	<b>2.55</b>	<b>0.002</b>	<b>0.002</b>
GJ 3530	24	166.35	<b>0.0</b>	<b>0.0</b>	79.45	<b>0.0</b>	<b>0.0</b>	70.89	<b>0.0</b>	<b>0.001</b>
GJ 3543	94	4.811	<b>0.0</b>	<b>0.0</b>	4.805	0.354	37.5	4.758	<b>0.0</b>	<b>0.001</b>
GJ 3563	12	<b>1.52</b>	0.075	0.245	<b>1.457</b>	0.393	76.2	<b>1.491</b>	0.192	<b>0.734</b>
GJ 3634	73	20.30	<b>0.0</b>	<b>0.0</b>	4.212	<b>0.0</b>	<b>0.0</b>	4.222	<b>0.0</b>	<b>0.804</b>
GJ 3643	21	<b>1.391</b>	0.084	0.207	<b>1.24</b>	<b>0.0076</b>	6.0	<b>1.174</b>	<b>0.0</b>	0.06
GJ 3700	11	<b>1.91</b>	<b>0.021</b>	0.259	<b>0.642</b>	<b>0.0001</b>	<b>0.0</b>	<b>0.437</b>	<b>0.0</b>	<b>0.007</b>
GJ 3708	24	<b>2.32</b>	<b>0.0</b>	<b>0.089</b>	<b>2.401</b>	1.0	77.1	<b>2.376</b>	0.294	0.343
GJ 3709	25	<b>2.34</b>	<b>0.0</b>	<b>0.076</b>	<b>2.424</b>	1.0	79.5	<b>2.378</b>	0.202	0.204
GJ 3728	17	15.51	<b>0.0</b>	<b>0.0</b>	15.029	0.311	26.2	16.031	0.361	<b>1.0</b>
GJ 3759	12	<b>1.61</b>	0.055	0.387	<b>1.748</b>	1.0	94.9	<b>1.79</b>	0.796	<b>0.738</b>

Continued on next page

Table B.6: Parameters of the long-term analysis.

Star	$N_{mes}$	$\chi^2_{0s}$	$P(\chi^2_0)$	$P(F_{value_0})$	$\chi^2_{1s}$	$P(F_{0/1})$	FAP (%)	$\chi^2_{2s}$	$P(F_{0/2})$	$P(F_{1/2})$
GJ 3779	20	91.49	<b>0.0</b>	<b>0.0</b>	<b>2.114</b>	<b>0.0</b>	<b>0.0</b>	<b>1.728</b>	<b>0.0</b>	<b>0.0</b>
GJ 3804	18	<b>2.85</b>	<b>0.0</b>	<b>0.032</b>	<b>1.803</b>	<b>0.0</b>	<b>0.3</b>	<b>1.878</b>	<b>0.0</b>	<b>0.992</b>
GJ 3813	21	193.97	<b>0.0</b>	<b>0.0</b>	34.26	<b>0.0</b>	<b>0.0</b>	35.52	<b>0.0</b>	<b>0.997</b>
GJ 3822	67	17.376	<b>0.0</b>	<b>0.0</b>	16.919	<b>0.0</b>	9.9	15.319	<b>0.0</b>	<b>0.0</b>
GJ 3871	36	9.653	<b>0.0</b>	<b>0.0</b>	6.649	<b>0.0</b>	<b>0.0</b>	6.39	<b>0.0</b>	<b>0.006</b>
GJ 3874	22	<b>2.553</b>	<b>0.0</b>	<b>0.05</b>	<b>2.474</b>	0.187	26.0	<b>1.887</b>	<b>0.0</b>	<b>0.0</b>
GJ 3885	12	<b>0.668</b>	0.712	0.846	<b>0.682</b>	0.829	44.1	<b>0.723</b>	0.631	<b>0.954</b>
GJ 3918	29	<b>2.34</b>	<b>0.0</b>	<b>0.03</b>	<b>2.394</b>	0.999	72.1	<b>2.443</b>	0.839	<b>0.988</b>
GJ 4001	21	$>10^4$	<b>0.0</b>	<b>0.0</b>	1516.222	<b>0.0</b>	<b>0.0</b>	583.754	<b>0.0</b>	<b>0.0</b>
GJ 4056	11	8.51	<b>0.0</b>	<b>0.003</b>	5.719	<b>0.0102</b>	2.1	5.035	<b>0.002</b>	0.117
GJ 4079	21	10.64	<b>0.0</b>	<b>0.0</b>	11.127	1.0	80.5	8.42	<b>0.0</b>	<b>0.0</b>
GJ 4088	14	23.69	<b>0.0</b>	<b>0.0</b>	14.96	<b>0.0005</b>	<b>0.4</b>	13.113	<b>0.0</b>	<b>0.044</b>
GJ 4160	18	<b>1.004</b>	0.384	0.714	<b>1.036</b>	0.979	60.2	<b>0.954</b>	<b>0.035</b>	<b>0.043</b>
GJ 4206	28	38.53	<b>0.0</b>	<b>0.0</b>	13.47	<b>0.0</b>	<b>0.0</b>	13.986	<b>0.0</b>	<b>1.0</b>
GJ 4254	31	$>10^4$	<b>0.0</b>	<b>0.0</b>	$>10^4$	0.984	77.5	$>10^4$	<b>0.0</b>	<b>0.0</b>
GJ 4303	72	84.56	<b>0.0</b>	<b>0.0</b>	32.141	<b>0.0</b>	<b>0.0</b>	15.646	<b>0.0</b>	<b>0.0</b>
GJ 4310	10	10.32	<b>0.0</b>	<b>0.002</b>	11.099	0.987	83.9	11.712	0.798	<b>0.865</b>
GJ 4332	33	5.59	<b>0.0</b>	<b>0.001</b>	5.502	0.189	62.4	5.43	<b>0.003</b>	0.181
GJ 4353	14	6.17	<b>0.0</b>	<b>0.01</b>	5.896	0.311	23.0	5.846	0.082	0.477
GJ 4364	11	<b>0.494</b>	0.86	0.906	<b>0.521</b>	0.961	94.5	<b>0.574</b>	0.95	<b>1.0</b>
GJ 9010	10	3.60	<b>0.0</b>	<b>0.158</b>	3.685	0.811	73.4	<b>2.8</b>	<b>0.038</b>	<b>0.036</b>
GJ 9018	50	5.57	<b>0.0</b>	<b>0.0</b>	5.562	0.511	33.6	5.471	<b>0.0</b>	<b>0.023</b>
GJ 9050	15	<b>2.94</b>	<b>0.0</b>	<b>0.083</b>	3.025	0.918	53.2	<b>2.719</b>	<b>0.041</b>	0.053
GJ 9066	25	36.24	<b>0.0</b>	<b>0.0</b>	7.768	<b>0.0</b>	<b>0.0</b>	6.197	<b>0.0</b>	<b>0.0</b>
GJ 9103A	44	12.38	<b>0.0</b>	<b>0.0</b>	12.098	<b>0.0207</b>	21.6	11.507	<b>0.0</b>	<b>0.0</b>
GJ 9118B	11	1153.76	<b>0.0</b>	<b>0.0</b>	657.914	<b>0.0024</b>	9.7	<b>2.812</b>	<b>0.0</b>	<b>0.0</b>
GJ 9133	14	<b>1.116</b>	0.27	0.567	<b>0.659</b>	<b>0.0002</b>	1.7	<b>0.606</b>	<b>0.0</b>	0.111
GJ 9137	19	10.19	<b>0.0</b>	<b>0.0</b>	9.083	<b>0.0164</b>	26.0	8.396	<b>0.001</b>	<b>0.038</b>
GJ 9349	18	<b>2.73</b>	<b>0.0</b>	<b>0.033</b>	<b>2.579</b>	0.132	23.6	<b>2.736</b>	0.155	<b>1.0</b>
GJ 9375	13	10.71	<b>0.0</b>	<b>0.0</b>	10.866	0.786	47.4	10.335	0.135	0.244
GJ 9425	86	156.12	<b>0.0</b>	<b>0.0</b>	155.236	<b>0.048</b>	27.7	147.663	<b>0.0</b>	<b>0.0</b>
GJ 9568	15	165.99	<b>0.0</b>	<b>0.0</b>	3.739	<b>0.0</b>	<b>0.0</b>	3.967	<b>0.0</b>	<b>0.999</b>
GJ 9588	33	9011.62	<b>0.0</b>	<b>0.0</b>	9262.826	1.0	94.3	8866.913	<b>0.01</b>	<b>0.009</b>
GJ 9590	14	$>10^4$	<b>0.0</b>	<b>0.0</b>	$>10^4$	<b>0.0002</b>	13.7	$>10^4$	<b>0.0</b>	<b>0.998</b>
GJ 9592	148	6.52	<b>0.0</b>	<b>0.0</b>	6.471	<b>0.0</b>	27.5	6.427	<b>0.0</b>	<b>0.0</b>
GJ 9647	11	3.32	<b>0.0</b>	<b>0.117</b>	3.07	0.3	28.1	3.255	0.227	<b>0.928</b>
HD223889	11	6.53	<b>0.0</b>	<b>0.006</b>	6.927	0.978	68.5	7.665	0.978	<b>1.0</b>
L32-8	19	$>10^4$	<b>0.0</b>	<b>0.0</b>	$>10^4$	<b>0.0237</b>	20.7	$>10^4$	<b>0.023</b>	<b>1.0</b>
LP776-25	12	120.20	<b>0.0</b>	<b>0.0</b>	126.752	0.978	81.9	57.257	<b>0.0</b>	<b>0.0</b>
LP816-60	153	4.63	<b>0.0</b>	<b>0.0</b>	4.371	<b>0.0</b>	<b>0.0</b>	4.322	<b>0.0</b>	<b>0.0</b>

Notes. Parameters of the LT analysis for the 200 stars with at least ten measurements.

Table B.7: Average activity level and estimated rotation period.

Star	$N_{mes}$	$\log_r HK$	P(d)	Star	$N_{mes}$	$\log_r HK$	P(d)	Star	$N_{mes}$	$\log_r HK$	P(d)
CD-246144	13	-4.619	23.6	CD-281745	15	-4.383	16.5	CD-4114656	21	-4.669	25.5
G80-21	12	-3.972	$<10$	GJ 1	46	-5.505	90.8	GJ 54.1	256	-4.597	22.9
GJ 79	12	-	-	GJ 85	11	-6.197	260.2	GJ 87	154	-5.358	72.6
GJ 91	26	-4.889	35.6	GJ 93	19	-5.103	49.3	GJ 105B	22	-5.543	96.2
GJ 118	20	-5.278	64.4	GJ 126	32	-4.997	42.0	GJ 157B	16	-4.436	17.9
GJ 163	179	-5.398	77.2	GJ 173	16	-5.120	50.6	GJ 176	115	-4.813	31.8
GJ 179	22	-5.210	58.1	GJ 180	49	-5.151	53.0	GJ 182	16	-3.896	$<10$
GJ 191	228	-5.826	148.0	GJ 205	103	-4.543	21.1	GJ 208	18	-4.086	10.5
GJ 213	122	-5.891	163.4	GJ 221	110	-4.719	27.5	GJ 229	200	-4.664	25.3
GJ 234	20	-4.346	15.6	GJ 250B	12	-4.924	37.6	GJ 273	315	-5.475	86.8
GJ 299	24	-5.482	87.8	GJ 300	39	-5.308	67.3	GJ 317	137	-5.262	62.8
GJ 333	11	-5.443	82.8	GJ 334	26	-4.373	16.3	GJ 341	57	-4.674	25.7
GJ 357	48	-5.557	98.4	GJ 358	34	-4.546	21.2	GJ 361	101	-4.849	33.5
GJ 367	24	-4.964	39.9	GJ 369	45	-4.964	39.9	GJ 377	11	-5.074	47.2
GJ 382	33	-4.639	24.4	GJ 388	56	-4.185	12.2	GJ 390	46	-4.651	24.8
GJ 393	175	-5.037	44.6	GJ 406	34	-4.574	22.1	GJ 422	40	-5.669	116.6
GJ 433	86	-5.079	47.6	GJ 438	19	-5.202	57.3	GJ 443	18	-4.986	41.3

Table B.7: Average activity level and estimated rotation period.

Star	N <sub>mes</sub>	log <sub>r</sub> HK	P(d)	Star	N <sub>mes</sub>	log <sub>r</sub> HK	P (d)	Star	N <sub>mes</sub>	log <sub>r</sub> HK	P (d)
GJ 447	156	-5.365	73.4	GJ 465	23	-5.660	115.1	GJ 476	12	-5.198	57.0
GJ 479	58	-4.746	28.7	GJ 480	37	-5.177	55.2	GJ 486	12	-5.686	119.6
GJ 510	13	-4.537	20.9	GJ 514	160	-4.857	33.9	GJ 526	32	-5.088	48.2
GJ 536	195	-4.832	32.6	GJ 550.3	42	-4.452	18.3	GJ 551	246	-4.741	28.4
GJ 555	14	-5.502	90.4	GJ 569A	24	-4.263	13.8	GJ 570B	340	-4.808	31.5
GJ 581	242	-5.657	114.4	GJ 588	75	-5.128	51.2	GJ 606	23	-4.644	24.5
GJ 618A	20	-5.283	64.8	GJ 620	22	-4.568	21.9	GJ 628	189	-5.518	92.7
GJ 634	23	-5.764	134.7	GJ 637	17	-5.173	54.8	GJ 654	193	-5.266	63.1
GJ 660	15	-5.092	48.5	GJ 667C	248	-5.367	73.6	GJ 674	212	-4.844	33.3
GJ 676A	125	-4.583	22.4	GJ 680	39	-5.048	45.3	GJ 682	21	-5.371	74.2
GJ 686	20	-5.120	50.6	GJ 693	179	-5.529	94.2	GJ 696	42	-4.490	19.4
GJ 699	117	-5.536	95.3	GJ 701	153	-4.928	37.8	GJ 707	17	-4.445	18.1
GJ 724	27	-4.694	26.5	GJ 729	29	-4.354	15.8	GJ 739	19	-5.106	49.5
GJ 740	54	-4.612	23.4	GJ 752A	147	-5.067	46.7	GJ 754	182	-5.405	78.1
GJ 784	39	-4.534	20.8	GJ 800A	30	-4.884	35.3	GJ 803	48	-3.870	<10
GJ 816	19	-5.131	51.5	GJ 821	11	-5.614	107.2	GJ 825	20	-4.693	26.4
GJ 832	60	-5.118	50.4	GJ 846	55	-4.522	20.4	GJ 849	71	-5.212	58.2
GJ 855	35	-4.601	23.0	GJ 864	15	-4.779	30.1	GJ 871.1A	28	-4.174	12.0
GJ 876	256	-5.401	77.6	GJ 877	42	-5.290	65.6	GJ 880	140	-4.676	25.8
GJ 887	154	-4.739	28.4	GJ 891	28	-4.988	41.4	GJ 900	13	-4.237	13.2
GJ 908	87	-5.276	64.1	GJ 1001A	25	-5.391	76.4	GJ 1009	12	-4.757	29.2
GJ 1018	15	-5.284	65.0	GJ 1046	20	-5.280	64.5	GJ 1061	111	-5.697	121.7
GJ 1075	35	-4.343	15.5	GJ 1132	117	-5.266	63.2	GJ 1135	18	-4.721	27.6
GJ 1214	112	-5.563	99.2	GJ 1236	11	-5.392	76.6	GJ 1284	22	-4.243	13.4
GJ 2003	41	-5.683	119.1	GJ 2060	11	-3.970	<10	GJ 2066	111	-5.098	49.0
GJ 2121	28	-5.400	77.5	GJ 3009	11	-5.482	87.8	GJ 3018	25	-4.708	27.0
GJ 3053	224	-5.488	88.6	GJ 3082	42	-4.704	26.9	GJ 3090	25	-4.38	16.4
GJ 3102	26	-4.240	13.3	GJ 3135	168	-5.414	79.1	GJ 3148	62	-4.369	16.2
GJ 3192	18	0.0	0.0	GJ 3205	20	-5.193	56.6	GJ 3212	12	-5.072	47.1
GJ 3218	45	-4.581	22.3	GJ 3221	28	-4.484	19.2	GJ 3256	29	-4.607	23.2
GJ 3279	11	-	-	GJ 3293	201	-5.022	43.6	GJ 3307	20	-4.704	26.9
GJ 3323	148	-4.671	25.6	GJ 3331	19	-3.880	<10	GJ 3341	134	-5.259	62.5
GJ 3379	14	-4.907	36.6	GJ 3403	14	-4.634	24.2	GJ 3404	13	-5.494	89.4
GJ 3455	12	-5.629	109.8	GJ 3501	11	-4.927	37.8	GJ 3502	22	-5.304	66.9
GJ 3528	15	-5.068	46.7	GJ 3530	24	-5.064	46.5	GJ 3543	94	-4.594	22.7
GJ 3563	12	-5.386	75.8	GJ 3634	73	-5.099	49.0	GJ 3643	21	-5.479	87.4
GJ 3700	11	-5.2755	64.0	GJ 3708	24	-5.376	74.7	GJ 3709	25	-5.472	86.4
GJ 3728	17	-4.380	16.4	GJ 3759	12	-4.891	35.7	GJ 3779	20	-	-
GJ 3804	18	-5.552	97.6	GJ 3813	21	-4.883	35.3	GJ 3822	67	-4.475	19.0
GJ 3871	36	-4.745	28.6	GJ 3874	22	-4.947	38.9	GJ 3885	12	-5.267	63.2
GJ 3918	29	-5.173	54.9	GJ 4001	21	-4.568	21.9	GJ 4056	11	-5.254	62.0
GJ 4079	21	-4.312	14.8	GJ 4088	14	-4.956	39.5	GJ 4160	18	-	-
GJ 4206	28	-4.6598	25.1	GJ 4254	31	-4.545	21.1	GJ 4303	72	-4.340	15.5
GJ 4332	33	-4.539	20.9	GJ 4353	14	-4.396	16.8	GJ 4364	11	-4.810	31.6
GJ 9018	50	-4.681	26.0	GJ 9050	15	-4.850	33.6	GJ 9066	25	-4.610	23.3
GJ 9103A	44	-5.144	52.5	GJ 9118B	11	-4.574	22.1	GJ 9133	14	-5.160	53.8
GJ 9137	19	-5.230	59.8	GJ 9349	18	-5.104	49.4	GJ 9375	13	-4.515	20.2
GJ 9425	86	-4.590	22.6	GJ 9568	15	-5.575	101.0	GJ 9588	33	-5.305	67.0
GJ 9592	148	-4.747	28.7	GJ 9647	11	-4.768	29.6	HD223889	11	-4.829	32.5
L32-8	19	-5.271	63.7	LP776-25	12	-3.996	<10	LP816-60	153	-5.236	60.3

**Notes.** Estimation of the rotation period ( $P$ ) derived from the empiric law determined in [Astudillo-Defru et al. \(2017a\)](#) with the average level of activity ( $\log_{rHK}$ ).